Investigation of Solar Cells and Phototransistors based on Hybrid Copper (I) Thiocyanate: Methanofullerene Materials

Wai Yu Sit

A thesis submitted in partial fulfilment of the requirements for the degree of
Doctor of Philosophy

Imperial College London
Department of Physics
November 2019

DECLARATION OF ORIGINALITY

This thesis describes the work carried out between October 2015 and October 2019 in the Experimental Solid State Physics group of Imperial College London, under the supervision of Prof. Thomas D. Anthopoulos and Prof. Jenny Nelson. The material presented herein is the product of my own work, unless stated. Where information has been derived from other sources, this has been indicated in the thesis.

COPYRIGHT DECLATION

Wai Yu Sit

London, November 2019

Abstract

The combination of organic and inorganic semiconductors offers a route to the development of solar cells and other optoelectronic devices that combine flexibility, high efficiency and high stability. In this thesis, we have investigated the hybrid organic: inorganic system, copper (I) thiocyanate (CuSCN): phenyl C71 butyric methyl acid ester ($PC_{70}BM$). We have shown that ~100 nm long CuSCN nanowires can be grown within $PC_{70}BM$ when a layer of $PC_{70}BM$ containing dilute CuSCN is deposited on top of a CuSCN layer on a heated substrate. Photovoltaic devices made from these nanowire-containing layers perform significantly better than devices made from CuSCN/$PC_{70}BM$ bilayers because the nanowires improve charge collection efficiency. The initial device based on a nanowire-containing CuSCN:$PC_{70}BM$ structure, the device shows ~5% power conversion efficiency. We show that these CuSCN NWs form well when the substrate temperature is about 115ºC. We then discovered that by spin-coating interlayers with a CuSCN rich precursor solution between the compact CuSCN layer and CuSCN:$PC_{70}BM$ photoactive mixed layer, the power conversion efficiency could be further improved to nearly 6% power conversion efficiency. Finally, we measured the carrier mobility of CuSCN:$PC_{70}BM$ layer using field-effect transistors. We find the carrier mobility values for holes and electrons to be on the order of 10^{-3} to 10^{-2} cm^2/Vs, similar to values for typical organic semiconducting materials. We have also characterized the same device as a phototransistor by illuminating the active area with light in the visible range.

This work has demonstrated the concept of the initial application of CuSCN nanowires, which has never been reported in any organic: inorganic mixed layer. CuSCN

nanowires could be a new approach for optimizing charge separation in light-absorbing acceptor systems.

Acknowledgements

I would like to express my sincere gratitude to everyone who have given their support of my doctoral study and research.

First, I would like to thank Prof. Thomas Anthopoulos and Prof. Jenny Nelson, my principle supervisors, for giving me a precious chance to study under their groups. Prof. Anthopoulos and Prof. Nelson are always encouraging and supportive academically and even in personal life. I am extremely thankful and indebted to them for sharing expertise, patience, motivation, excellent guidance, and providing me with an excellent atmosphere for doing research.

I would also like to thank my co-workers in the AMD laboratory and Jenny's group. Hendrik, Ivan, Yen, Dimitra, Nikos, Sungho, Dongyoon, Francesca, Nilushi, Alex, Gwen, Zan, Wentao, Julianna, Flurin, Max, Supamas, Sachetan, Mohammed, Jun and Xingyuan, who gave me guidance and advises in my research. It would have been a very challenging doctoral study without them.

Dr. Xuhua Huang, for the maintenance of instruments and technical supports.

Dr. Claire Burgess, for the high quality TEM images and detailed analysis.

My Fiancée, Michelle, who supported me all the way through the doctoral study.

My parents, my brother. They were always supporting and encouraging with their best wishes.

List of Publications

1. **W. Y.Sit**, F. D.Eisner, Y. H.Lin, Y.Firdaus, A.Seitkhan, A. H.Balawi, F.Laquai, C. H.Burgess, M. A.McLachlan, G.Volonakis, F.Giustino, T. D.Anthopoulos, Adv. Sci. 2018, 5, 1700980

2. Y.Firdaus, A.Seitkhan, F.Eisner, **W.-Y.Sit**, Z.Kan, N.Wehbe, A. H.Balawi, E.Yengel, S.Karuthedath, F.Laquai, T. D.Anthopoulos, Sol. RRL 2018, 2, 1800095.

3. N.Wijeyasinghe, L.Tsetseris, A.Regoutz, **W. Y.Sit**, Z.Fei, T.Du, X.Wang, M. A.McLachlan, G.Vourlias, P. A.Patsalas, D. J.Payne, M.Heeney, T. D.Anthopoulos, Adv. Funct. Mater. 2018, 28, 1.

4. S.Karuthedath, J.Gorenflot, Y.Firdaus, **W. Y.Sit**, F.Eisner, A.Seitkhan, M. K.Ravva, T. D.Anthopoulos, F.Laquai, Adv. Energy Mater. 2019, 9, 1.

5. M. Chaudhry, J Panidi, S. Nam, A. Smith, J. Lim, K. Tezner, P. Patsalas, G. Vourlias, **W. Y. Sit**, Y. Firdaus, M. Heeney, D. Bradley, T. D. Anthopoulos, Adv. Electron. Mater., 2019, 1901132

Glossary of Symbols and Abbreviations

AFM	Atomic Force Microscopy
BCP	Bathocuproine
BHJ	Bulk Heterojunction
CB	Conduction Band
CIGS	Copper Indium Gallium Selenide
CuSCN	Copper Thiocyanate
DCB	Dichlorobenzene
DES	Diethyl Sulfide
DFT	Density Functional Theory
E_g	Energy Bandgap
EQE	External Quantum Efficiency
ETL	Electron Transport Layer
FF	Fill Factor
GaAs	Gallium Arsenide
HOMO	Highest Occupied Molecular Orbital
HTL	Hole Transport Layer
ITO	Indium Tin Oxide
IPCC	Intergovernmental Panel on Climate Change
J-V	Current Density-Voltage
LED	Light Emitting Diodes
FET	Field Effect Transistors
NREL	National Renewable Energy Laboratory
OPV	Organic photovoltaics
OFET	Organic Field Effect Transistors
OLED	Organic Light Emitting Diodes
PV	Photovoltaics
$PC_{60}BM$	phenyl-C61-butyric acid methyl ester
$PC_{70}BM$	phenyl-C71-butyric acid methyl ester
PCE	Power Conversion Efficiency
PEDOT:PSS	poly(3,4-ethylenedioxythiophene) polystyrene sulfonate
PHJ	Planar Heterojunction
SRH	Shockley–Read–Hall recombination
TEM	Transmission Electron Microscopy

VB	Valence Band
V_{oc}	Open Circuit Voltage

Table of contents

List of figures

List of tables

Chapter 1 Background

The mass production and consumption of fossil fuel started from the industrial revolution in the 18th century. It converted hand production methods into machinery production. Since then, the development of science and technology accelerated significantly. However, the high consumption of coal or fossil fuel leads to a large amount of pollution gas emission to the atmosphere. Figure 1.1 shows a simulation of the amount of greenhouse gas from the year 1750 to now.[1] It is clear that the amount of greenhouse gas has increased significantly from the 18th century. Primary greenhouse gases are generally considered to be carbon dioxide, methane, nitrous oxide, ozone, and water vapor. The main reason for the emission of such greenhouse gases is due to the combustion of non-renewable fossil fuel. Reports show that the CO_2 concentration has surpassed the 400ppm, which the Intergovernmental Panel on Climate Change (IPCC) report suggests that the CO2 concentration is likely to reach 2000ppm by 2250.[2] Such an increase will impose a big impact on the global climate, more extreme weather are expected. As a result, the reduction of the consumption of fossil fuel is in paramount importance.

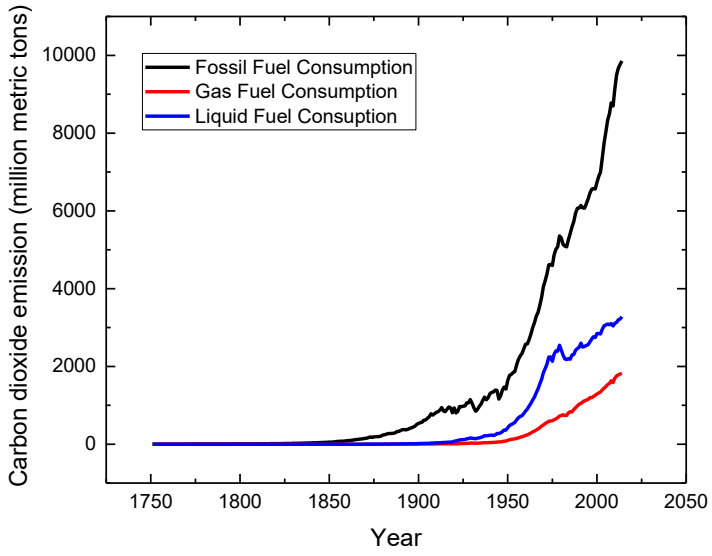

Figure 1.1 Carbon dioxide emission of carbon dioxide from 1750 from different consumption of non-renewable fuel

Looking for renewable energy sources is one of the promising ways to replace the use of fossil fuel. For example, wind energy, geothermal energy, solar energy, and hydroelectricity. Apart from solar energy, all other energy sources cannot be easily used domestically because they require a large area for the implantation of generators. For solar cells, we could build large arrays of solar panels over a desert or install solar panels on the rooftop to harvest solar energy. In this chapter, we will discuss the development of solar cells.

1.1 Inorganic solar cells

The first p-n junction of inorganic silicon (Si) based solar cell was made in 1954 in the Bell Telephone Laboratories.[3] At that time, the power conversion efficiency (PCE) was 6%. Many other types of inorganic solar cells were then developed such as gallium

arsenide solar cell(GaAs) and copper indium gallium selenide (CIGS) solar cell. Figure 1.2 shows the growth of photovoltaic device efficiency in the past 44 years from the National Renewable Energy Laboratory (NREL).[4] The highest efficiency of single-junction solar cells of Si, GaAs, CIGS and the organic solar cell to date is summarized in Table 1.1. It is worth noting that the theoretical maximum power conversion efficiency of a single junction solar cell is 33.7%, according to the Shockley-Queisser limit[5], which means the development of inorganic photovoltaic technology has become mature.

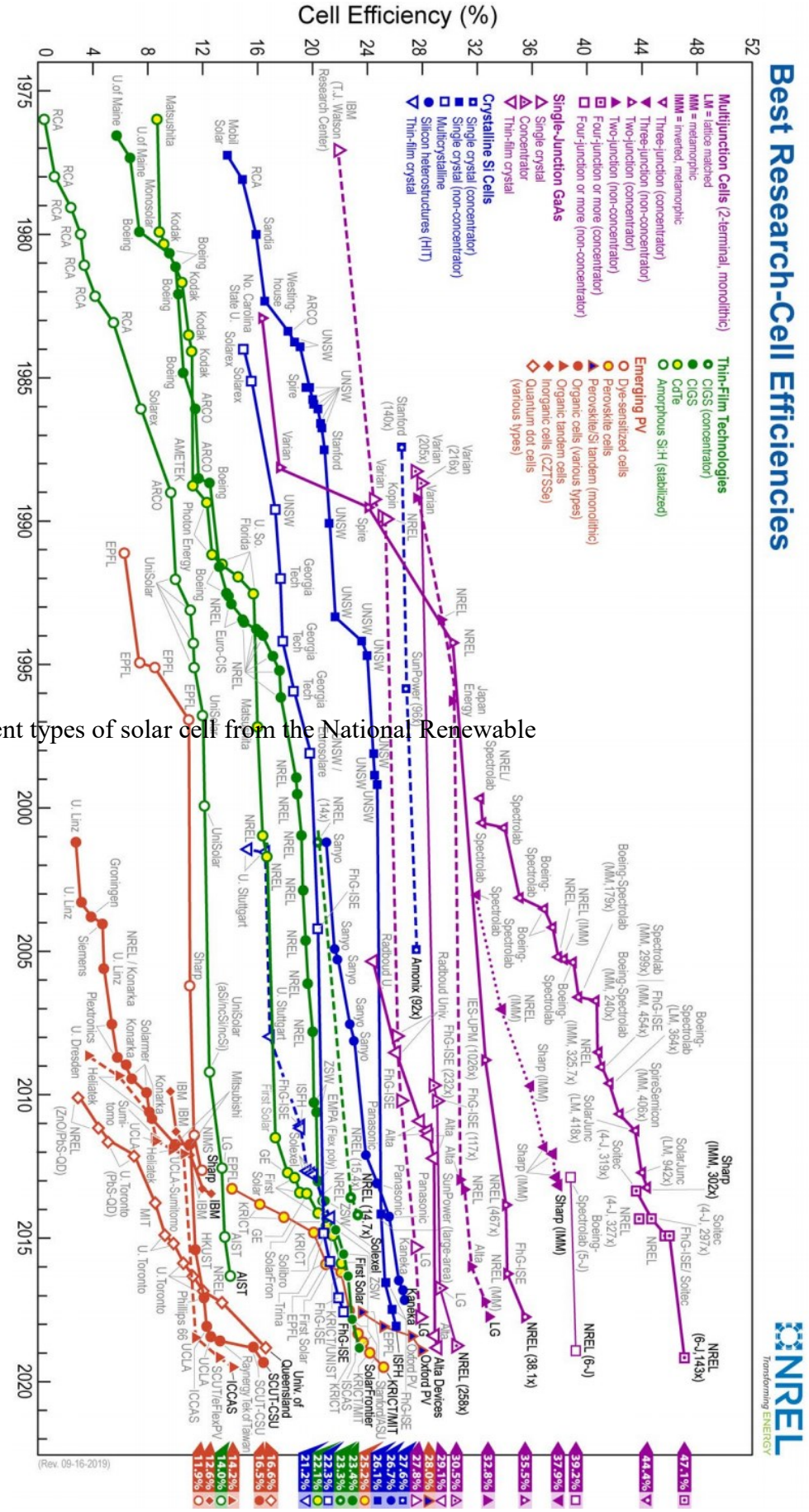

development of different types of solar cell from the National Renewable

Photoactive material	Power conversion efficiency
GaAs	29.1%
Organic	16.5%

Table 1.1 Single junction solar cell efficiency record to date[3]

From Figure 1.2 and Table 1.1, although organic solar cells do not have high efficiency as an inorganic photovoltaic device, it has many advantages. We will discuss the development of organic devices in the next section.

1.2 Development and advantages of organic devices

In the 1970s, it was found that the derivatives of organic molecule polyacetylene have high conductivity, which is in the order of ~10 $\Omega^{-1}cm^{-1}$.[6] The electrical properties of many other organic materials were investigated since then. Steven van Slyke and Ching Tang fabricated the first organic light-emitting diodes using 8-hydroxyquinoline aluminum (Alq_3) as the light-emitting layer.[7] Their discovery has led to the current OLED development from companies like Samsung and LG. Both companies have already released the curved displays on television and mobile phone, which make uses of the flexibility of organic materials as shown in Figure 1.3. Also, prototypes of foldable phone (Samsung Galaxy Fold), has been produced and will be released to the market very soon. Therefore, the future of organic-based devices is very promising if we consider the advantages of organic-based devices:

1) The material can be chemically synthesized

The type of elements used in the inorganic semiconductor is very limited. They are usually made by group IV elements (Si) or the combination of group III/V (GaAs, GaN), or more than two elements (CIGS, InGaN, InAlN for solar cell). However, for organic materials, synthetic chemists can add or edit functional groups, branch chains of organic molecules or polymers, which provides a higher potential for different use. Also, the energy gap between organic materials can be fine-tuned by adding specific atoms such as fluorine, which helps the optimization of organic optoelectronic devices.

2) Solution processible and cost-effective:

The fabrication process of inorganic solar cells needs to be very clean and high temperature because of the growth of crystalline structure, which increases the difficulty and cost for mass production. While organic materials can be synthesized and solution-processed, making it possible to perform large-area fabrication under an ambient condition such as blade coating and roll-to-roll fabrication.

3) Flexibility

Organic small molecules or polymers are not as rigid as inorganic molecules, which means they can be fabricated on a flexible substrate to make bendable solar cells or light-emitting diodes. Such properties can also be exploited to make portable devices such as smart glass or foldable solar cells and install solar cells behind a backpack for military use.

Figure 1.3. Rollerble OLED display from LG (left) and Samsung Galaxy Fold (right)

1.3 Motivation of this work

Organic materials have the advantage of cheap and simple processing methods. However, due to the low dielectric constant of organic materials, organic devices often suffer from severe carrier recombination.[8,9] Also, the carrier mobility of organic materials is usually not as high as inorganic compounds. A lot of work based on hybrid organic/inorganic devices have been investigated, which combines the advantages of both organic and inorganic semiconductors.

In this thesis, we aim to utilize the ambipolar transport and light-absorbing properties of organic methanofullerene, [6,6]-phenyl-C61-butyric acid methyl ester ($PC_{60}BM$) and[6,6]-phenyl-C71-butyric acid methyl ester ($PC_{70}BM$) as a light-absorbing layer to fabricate a photovoltaic device with the help of copper (I) thiocyanate (CuSCN). CuSCN is a promising inorganic hole transporting layer because it possesses high hole mobility, high bandgap, and low absorbance in the visible range.[10–14]

This thesis is organized as follows. In Chapter 1, the fundamental theory of organic and inorganic semiconductors will be outlined. Experimental details will then be discussed in Chapter 2. In Chapter 3, we will discuss the device fabrication of efficient PCBM only devices with CuSCN. We have discovered that CuSCN nanowires are grown from CuSCN compact layer, which improves the PCBM only device significantly. In Chapter 4, we will examine different approaches to improve the CuSCN:$PC_{70}BM$ device, involving growing seed layers, and adding metal nanoparticles to improve light absorption. Finally, in Chapter 5, we used thin-film transistors to measure the carrier mobility of CuSCN:$PC_{70}BM$ device and the application as CuSCN:$PC_{70}BM$ phototransistors.

References

[1] United States Environmental Protection 2019. https://www.epa.gov/ghgemissions/global-greenhouse-gas-emissions-data

[2] IPCC, IPCC Report https://www.ipcc.ch/reports **2017**

[3] D. M.Chapin, C. S.Fuller, G. L.Pearson, *J. Appl. Phys.* **1954**, *25*, 676.

[4] N. R. E. L.(NREL), **n.d.**, DOI https://www.nrel.gov/pv/cell-efficiency.html.

[5] W.Shockley, H. J.Queisser, *J. Appl. Phys.* **1961**, *32*, 510.

[6] H.Shirakawa, E. J.Louis, A. G.MacDiarmid, C. K.Chiang, A. J.Heeger, *J. Chem. Soc. Chem. Commun.* **1977**, 578.

[7] S. A.VanSlyke, C. H.Chen, C. W.Tang, *Appl. Phys. Lett.* **1996**, *69*, 2160.

[8] J. C.Scott, G. G.Malliaras, *Chem. Phys. Lett.* **1999**, *299*, 115.

[9] N.Cho, C. W.Schlenker, K. M.Knesting, P.Koelsch, H. L.Yip, D. S.Ginger, A. K. Y.Jen, *Adv. Energy Mater.* **2014**, *4*, 1301857

[10] N.Wijeyasinghe, T. D.Anthopoulos, *Semicond. Sci. Technol.* **2015**, *30*, 104002.

[11] N.Wijeyasinghe, A.Regoutz, F.Eisner, T.Du, L.Tsetseris, Y. H.Lin, H.Faber, P.Pattanasattayavong, J.Li, F.Yan, M. A.McLachlan, D. J.Payne, M.Heeney, T. D.Anthopoulos, *Adv. Funct. Mater.* **2017**, *27*, 1701818

[12] N.Yaacobi-Gross, N. D.Treat, P.Pattanasattayavong, H.Faber, A. K.Perumal, N.Stingelin, D. D. C.Bradley, P. N.Stavrinou, M.Heeney, T. D.Anthopoulos, *Adv. Energy Mater.* **2015**, *5*, 1. 1401529

[13] J. W.Jung, C. C.Chueh, A. K. Y.Jen, *Adv. Energy Mater.* **2015**, *5*, 1645.

[14] A.Casey, J. P.Green, P.Shakya Tuladhar, M.Kirkus, Y.Han, T. D.Anthopoulos, M.Heeney, *J. Mater. Chem. A* **2017**, *5*, 6465.

Chapter 2 Fundamental concepts and working principles of semiconductors

2.1 Fundamental concept of semiconductors

2.1.1 Electrical conduction in semiconductors

To quantify the electric charge movement inside a solid, we can define the current density $\vec{J}$ be the amount of electric charge passing through a solid per unit area per second. It is given by

$$\vec{J} = ne\vec{v} \tag{2.1}$$

where n is the number of electrons passing through such a solid per unit volume, e is elementary charge constant and $\vec{v}$ is the velocity of the electric charge.

Paul Drude proposed a model to explain the electrical conductivity in metals. The Drude model has three assumptions for the motion of electrons inside metals:[1] 1. Metals contain free electrons, which can be treated as electron gas. 2. Metal ions are relatively massive compared to electron. Therefore, ions can be assumed to be stationary. 3. In the absence of electric field, $\vec{E}$, the average kinetic energy of an electron is given by $\left\langle \frac{1}{2}mv^2 \right\rangle$, where the average velocity $\langle \mathrm{v} \rangle = 0$ but the mean square speed $\langle v^2 \rangle > 0$. As shown in Figure 2.1, without an electric field, electrons are in random motion inside the solid, however, the average displacement of the electrons is negligible. Further, in the presence of an electric field, charges are accelerated. An extra component of velocity is given to the charge such that there will be a net movement and displacement. The average velocity of charges moving inside such solid is the drift velocity, v_d.

Figure 2.1 Schematic path of the movement of electric charge. a) with influence of electric field and b) without the influence of electric field.

If we consider the motion of an electric charge, the force F experienced by the charge is given by

$$F = -eE \tag{2.2}$$

Therefore, by Newton's second law, the velocity of the charge, v , is given by

$$v = \mathrm{v}_0 - \frac{eE}{m}t \tag{2.3}$$

where v_0 is the intrinsic velocity, v_d is the drift velocity, m is the mass of electron and t is the time taken for each collision. By the assumption of Drude's model, the average velocity $\langle \mathrm{v} \rangle = \frac{-eE}{m}\langle t \rangle$ because $\langle v_0 \rangle = 0$. As a result, combining (2.1) and (2.3), the relationship between J and E can be written as

$$J = -\frac{ne^2 t}{m}E \tag{2.4}$$

It shows that current density is directly proportional to E with a proportionality constant σ,

$$J = \sigma E \tag{2.5}$$

$$\sigma = \frac{ne^2 \mathrm{t}}{m} \tag{2.6}$$

where σ is defined as the conductivity of a solid. For instance, the conductivity for

some metals, non-metal, and semimetals are given in Table 2.1.[2] The conductivity depends on the charge concentration, which are different depending on the intrinsic properties of the material. For example, semiconductors such as silicon can be doped to increase certain type of carrier concentration to increase the conductivity.

Materials	**Conductivity [S/m]**
Aluminum	3.77×10^{7}
Gold	4.11×10^{7}
Silicon (undoped)	1.56×10^{-3}
Silicon (doped)	$\sim 10^{1} - 10^{3}$
Glass	$\sim 1 \times 10^{-15}$
Teflon	$\sim 1 \times 10^{-25}$

Table 2.1 Conductivity of different materials

2.1.2 Carrier Mobility

Apart from conductivity, we can also characterize how effective electrons move inside a solid using the concept of carrier mobility. If we consider the momentum, p, of a charge

$$p = mv_d = -eE\tau \tag{2.7}$$

where τ *i*s the mean free time for the charge to travel without collision. The drift velocity v_d is then directly proportional to the applied electric field, that is

$$v_d = \mu E \tag{2.8}$$

where μ is the carrier mobility inside the solid, which is given by

$$\mu = \frac{-e\,\mathrm{t}}{m} \tag{2.9}$$

The carrier mobility only depends on the collision time and the effective mass of the carrier. There are two types of carriers, namely electron and hole. The electron is the fundamental charge which carries -*e* coulomb of charge (-1.6×10^{-19}C), whilst the hole is a quasiparticle that represents a missing electron inside an atom and thus contains +*e* coulomb of charge. As a result, there are hole and electron mobility in a semiconductor. In many semiconductors, holes usually has a lower carrier mobility due to higher effective mass of hole carriers. For example, Table 2.2 shows the mobility of polycrystalline silicon, amorphous silicon, graphene, CuSCN, and $PC_{70}BM$. [3–6] It is worth noting that carrier mobility is independent of electric field. However, in some cases, carrier mobility is measured to be field dependent. Other transport models such as the Poole Frenkel model is used to describe such behavior. where the expression is given by:

$$\mu = \mu_0 e^{\beta\sqrt{\mathrm{E}}} \tag{2.10}$$

where β is the Poole Frenkel slope, which is an intrinsic property of the materials, and it can be determined experimentally.[7–11]

	Electron mobility [cm^2/Vs]	Hole Mobility [cm^2/Vs]
Polycrystalline Si	300-1500	500
Amorphous Si	$5x10^{-2}$	$5x10^{-4}$
Graphene	200000	
CuSCN		$1x10^{-2}$
$PC_{70}BM$	$1x10^{-2}$	$1x10^{-2}$

Table 2.2 Mobility values of different inorganic and organic semiconductors

2.1.3 Band Structure

The mobility describes how fast electrons and holes can pass through the semiconductor. However, most of the electrons inside a semiconductor are not free carriers, which means they cannot contribute to electrical conduction. This phenomenon can be explained by the band structure.

Electricity conduction is the result of a movement of charge at different energy states. From quantum mechanics, these energy states for electrons to migrate are discrete. For any isolated atoms, the energy can be described by the Bohr model by solving the Schrödinger equation in three-dimensional space.[12] Taking hydrogen as an example, the discrete energy level of hydrogen given by:

$$E_n = \frac{1}{(4\pi\varepsilon_0)^2}\frac{me^4}{2n^2\hbar} \qquad -13.6eV \qquad (2.10)$$

where m is the mass of electron, ε_0 is the permittivity of free space, n is the principle

quantum number, $\hbar$ is the reduced Planck constant.[13] If there is a system of two hydrogen atoms the electronic orbital of the atoms is very closed to each other. By the Pauli Exclusion Principle, no more than two electrons in one system can have the same energy states.[14] The energy of the wavefunction of these approaching electrons starts to distort and cause a change in energy level. Overlapped orbital will cause the energy level to split into two distinct levels such that one of the electrons has a higher energy state and another one has a lower energy state. Now, if we consider there are *N* atoms in the system getting close to each other, the distortion of wavefunction will become significant, which causes more discrete energy states to overlap. Since the number of atoms is large, the discrete energy level will become two continuous energy bands. As shown in Figure 2.2, when the lattice spacing is close (at point *a* in Figure 2.2), the energy states form two different energy band. The one below is valence band (VB) and the one above is conduction band(CB).

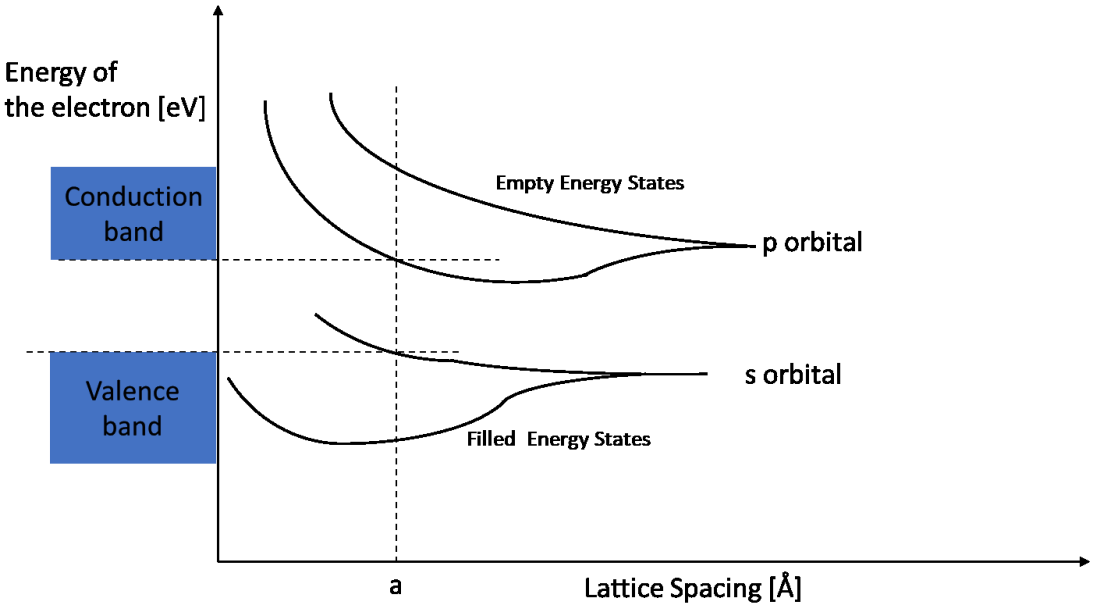

Figure 2.2 Energy-distance diagram of two approaching atoms. When the lattice spacing is large, there are two discrete energy states (p orbital and s orbital). When these electrons

are getting closed to each other, the energy states start to form continuous bands.

The valence band has the lower energy level and is fully filled with electron at absolute zero temperature. On the other hand, the conduction band has a higher energy which has no electron occupied at absolute zero temperature. Between the conduction band and valence band has no available energy states and therefore it is a forbidden band where no electrons can be found in this state.

Figure 2.3 shows the band structure of insulator, semiconductor and conductor. For an insulator or a semiconductor, conductivity at absolute zero temperature is poor because all electrons are lying in the valence band and all neighboring states are fully occupied. Nevertheless, if the temperature of the system is sufficiently high such that the electron can be excited from the VB to CB, the electron can now be mobilized if an electric field is applied to the material. The velocity of the electron can now be described by the carrier mobility which is defined in the last section. From the above phenomenon, the conductivity of a material depends on the energy gap between VB and CB. Such gap is generally defined as the band gap (E_g). If E_g of a material is large , at room temperature (~298K) the thermal energy is not sufficient to thermally excite electrons in VB to promote to the CB, and it is termed an insulator. The bandgap of an insulator is typically ~9eV. On the other hand, in semiconductor, the energy gap is relatively small (~1eV) such that the energy at room temperature is sufficient to excited electrons thermally from VB to CB for electrical conduction. In conductors, electrons can be found in CB even at absolute zero temperature, that means electrons can move freely inside conductors in any conditions.

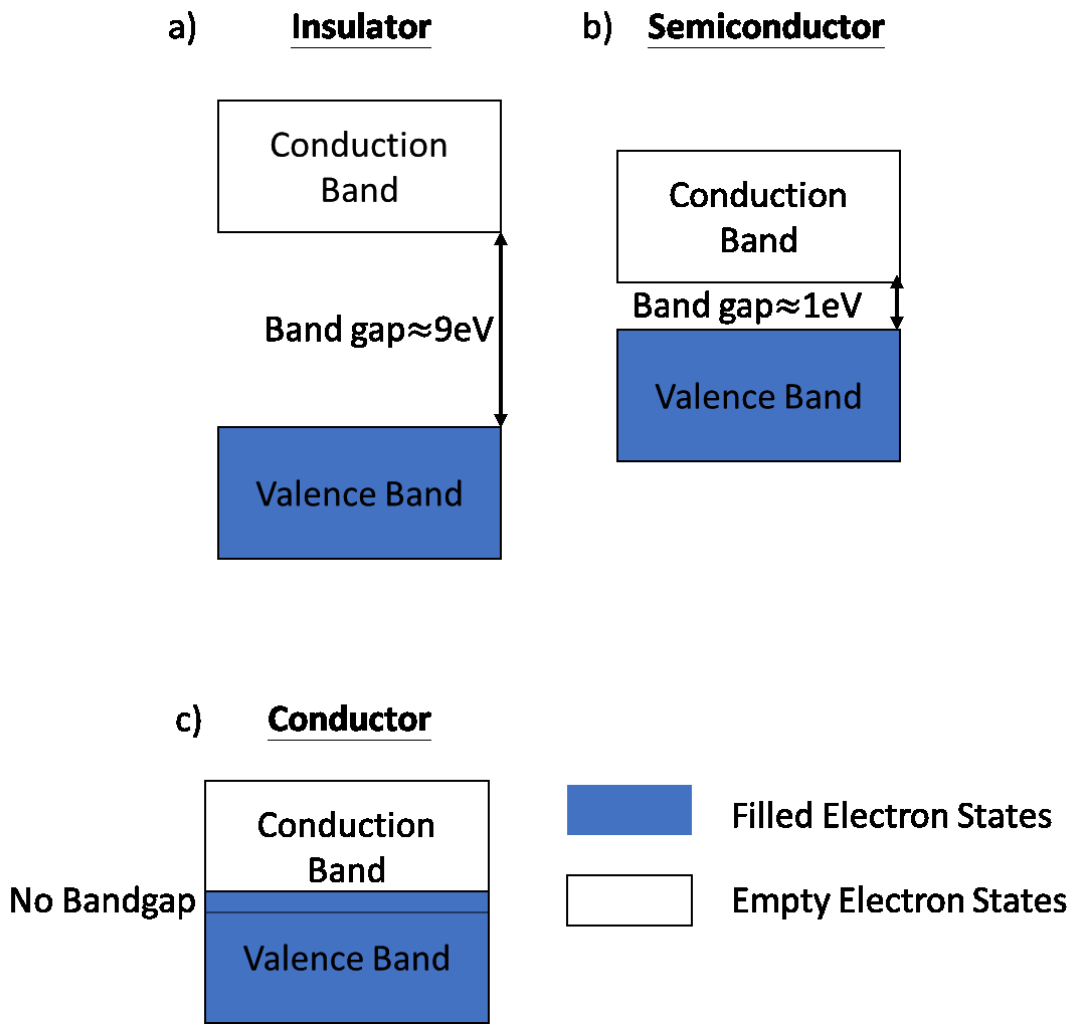

Figure 2.3 Energy band structure of a) insulator, b) semiconductor and c) conductor.

2.1.4 Electronic Structure of Organic Compounds

In general, Group 1-3 elements are metal, Group 4 elements such as Si and Ge are semiconductor and Group 5-8 elements are insulators. Hydrocarbon based molecules that consist of hydrogen and carbon are generally considered to be insulators. Nevertheless, in certain molecular arrangement, organic molecules are electrically conductive and behave as semiconductor. Shirakawa et.al found that polyacetylene has electrical conductivity of σ=38Ω^{-1}cm^{-1}.[15] Based on their following results,[16,17] a

lot of work using organic based compound has been conducted. The application of organic molecules has been growing gradually, such as flexible organic light emitting diodes (OLEDs) display,[18–23] and organic photovoltaic devices (OPVs).[24–33] To understand the working principle of these real-life devices, we will discuss the electronic structure and the theory behind the electrical conduction of hydrocarbon-based molecules.

The atomic orbital of carbon is illustrated in Figure 2.4. Since carbon has 6 electrons, it has the electron configuration of $1s^2 2s^2 2p^2$. The orbital (red region) represents the highest probability to find an electron. The 2s orbital is generally larger than 1s, which means the electron in the 2s orbital is probably be found further away from the carbon atom. Also, the node shell in the 2s orbital represents the space that 2s electrons can never be found. Secondly, in 2p orbital, there are 3 sub-orbitals, which are p_x p_y and p_z. Covalent bond is formed between carbon and adjacent atoms, at least one or more electron is being shared with the adjacent atom to the form such bond. To achieve this, outer most electrons (electrons in 2s and 2p orbital) in carbon atom will undergo hybridization. All 2s and 2p orbitals will be combined and form four equivalent hybrid orbitals with the same amount of energy as shown in Figure 2.5. The carbon is then considered to be sp^3 hybridized. In this way, carbon can form 4 single bonds with 4 adjacent atoms. For instance, the carbon atom in methane (CH_4) is sp^3 hybridized. Sometimes the carbon atom may have other hybridization configuration such as sp^2 hybridization. In this case, only the 2s orbital is hybridized with one of the p orbitals, leaving another p orbital unhybridized. Two single bonds and one double bond between carbon atom and the adjacent atom can be formed in this way. Taking ethene as an example, (Figure 2.6a) both carbon atoms in ethene are

sp^2 hybridized. As a result, all single C-H bonds in ethene are contributed by the sp^2 orbital and the C=C bonds are contributed by unhybridized p-orbital.

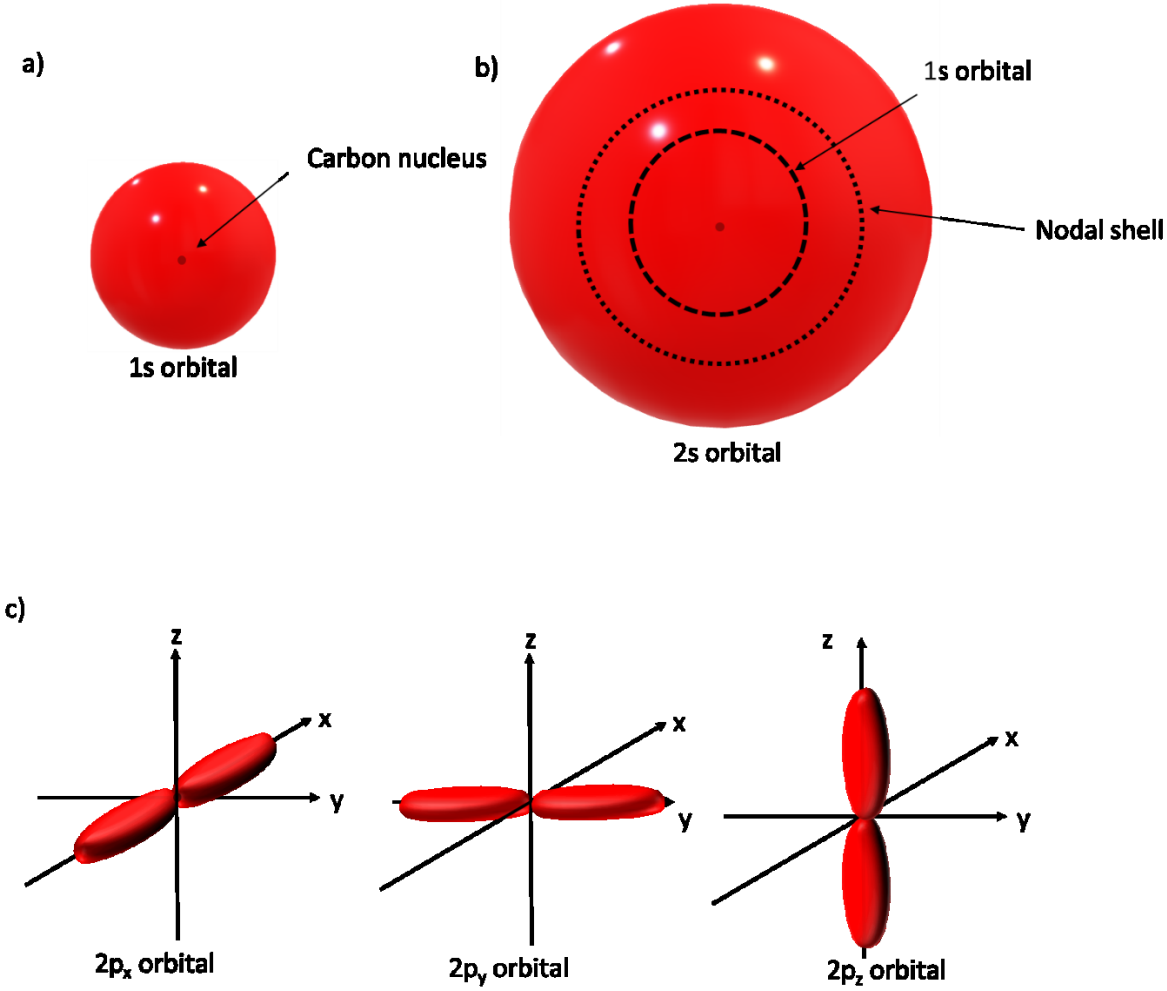

Figure 2.4 Illustrative diagram of a)1s, b) 2s, and c) 2p orbitals of a carbon atom.

Figure 2.5 Energy of the electrons inside a unhybridized and sp^3 hybridized carbon atom

A single bond is referred to be σ-bond and a double bond is a π-bond. σ-bonds are the strongest type of covalent bond because they are formed by head-on

overlapping of the orbitals. On the other hand, π-bond is relatively weak because the orbital has less overlapping. Since π-bond is the overlapping effect of p-orbitals, electrons in these orbitals are not confined in their own orbital. Instead, they can freely move within the overlapped orbital, causing delocalization effect of π electrons as shown in Figure 2.6.

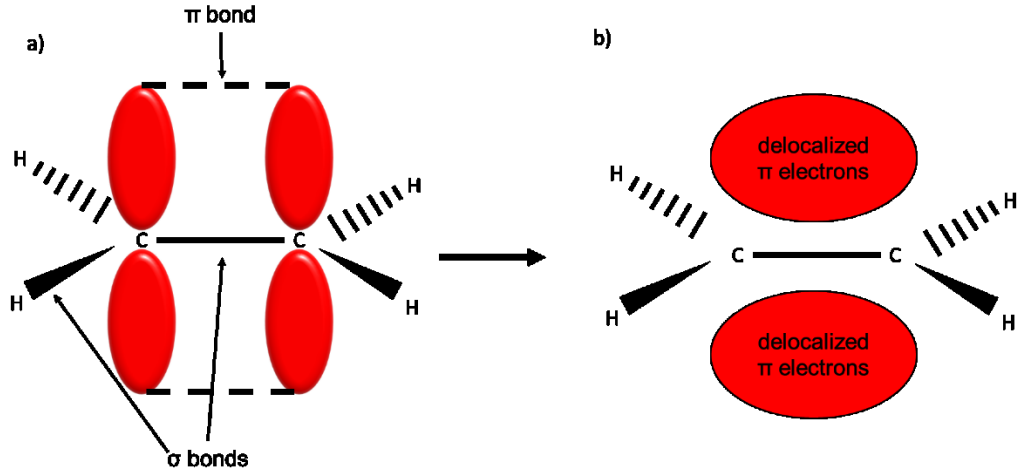

Figure 2.6 Illustration of p-orbital overlapping in ethene (a). The C-C bond and one of the bonds in C=C are sigma bonds. The orbitals labelled in red represents the p-orbitals. b) p-orbitals from each of the carbon will overlap and electrons inside the π bond are delocalized

Now, consider the organic structure of a benzene which consists of six carbon atoms, all carbon atoms are sp^2 hybridized and therefore electrons are delocalized within the whole benzene as shown in Figure 2.7. The delocalization of electron inside a hydrocarbon-based molecule is known as conjugation. Such conjugation of electrons allows hydrocarbons to conduct electricity. In the application OPVs and OLEDs, conjugated organic polymer and small molecules are often used. Developing high mobility conjugating organic polymer/small molecules has been a key focus in the community.[34–39]

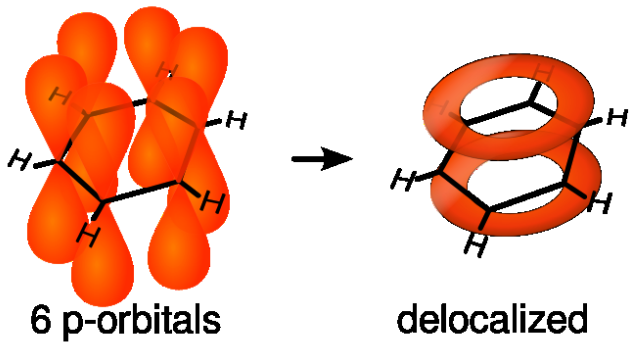

Figure 2.7 Delocalization of electrons in a benzene molecule.

2.1.5 Highest Occupied Molecular Orbital and Lowest Unoccupied Molecular Orbital

Consider now that we have two identical hydrogen atoms far away from each other. Both hydrogen atoms have one electron in their outer 1s shell, and they have the same energy. Since electrons can be regarded as a stationary wave inside the atom, the wavefunction of electron can either be in phase (Figure 2.8a) and out of phase (Figure 2.8b). When both of the atoms are approaching to each other, a bond between them can be formed to become hydrogen gas as shown in Figure 2.8c and Figure 2.8d. There are two types of bonding possible:

1) Bonding: The orbitals overlap and show constructive interference when the two electrons are combined in phase. In this situation, the probability to find an electron within the hydrogen gas can be described by the superposed wavefunction. The squared modulus of the superposed wavefunction $|\psi|^2$ can be interpreted as the probability density that the electron can be found. Solving for the energy states using Schrodinger equation,

$$-\frac{\hbar}{2m} \quad U\Psi = i\hbar \qquad (2.11)$$

it is found that the bonding has lower energy states.

2) Antibonding: In this case, the electron wavefunction is out of phase with another electron wavefunction. As a result, the overlapped orbitals undergo destructive interference. The overlapped wavefunction is different from bonding where the overlapped wavefunction has zero amplitude in the middle between two nuclei (node). That means electron can never be found at this point.

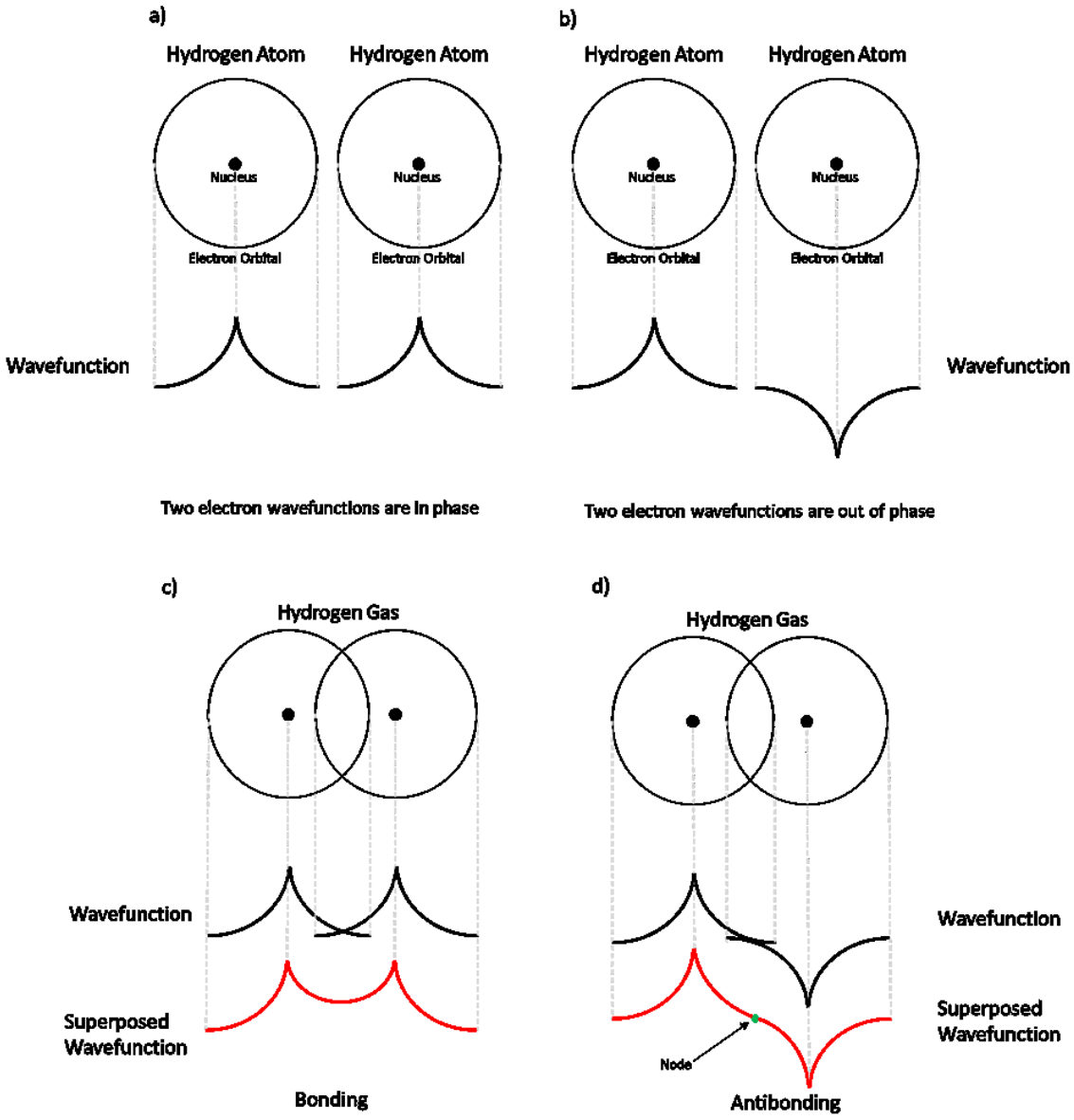

Figure 2.8 Diagram of two hydrogen atoms where two electron wavefunctions are a) in phase or b) out of phase). When two hydrogen atoms are bonded together, the superposed wavefunction when two electron wavefunctions are c) in phase and d) out of phase. The node in the antibonding phase represents the probability detect an electron at that point is zero.

Figure 2.9 shows the change in energy states of the two hydrogen atoms described above. The 1s energy states from each of the atom will split into two different states.

The one with higher energy is antibonding, which is usually unoccupied. The one with lower energy is bonding, which is occupied with two electrons in this example. In this situation, since there are only two electrons in the system, bonding is also the highest occupied molecular orbital (HOMO). HOMO is similar to valence band (VB) in inorganic semiconductor that facilitates the movement of holes. On the other hand, antibonding states are usually empty, so it is similar to conduction band (CB) that facilitates the movement of electrons. Due to the complexity of organic molecules, which consist of many carbons and hydrogen atoms, solving the Schrodinger equation to obtain HOMO and LUMO for organic material is fundamentally challenging. Therefore, the Born-Oppenheimer approximation was often used.[40] The approximation assumes that the movement of electron and the nucleus can be considered separately because the mass of nuclei is much heavier than electron. The calculation of HOMO and LUMO are usually done by computation using density functional theory (DFT).[41–45]

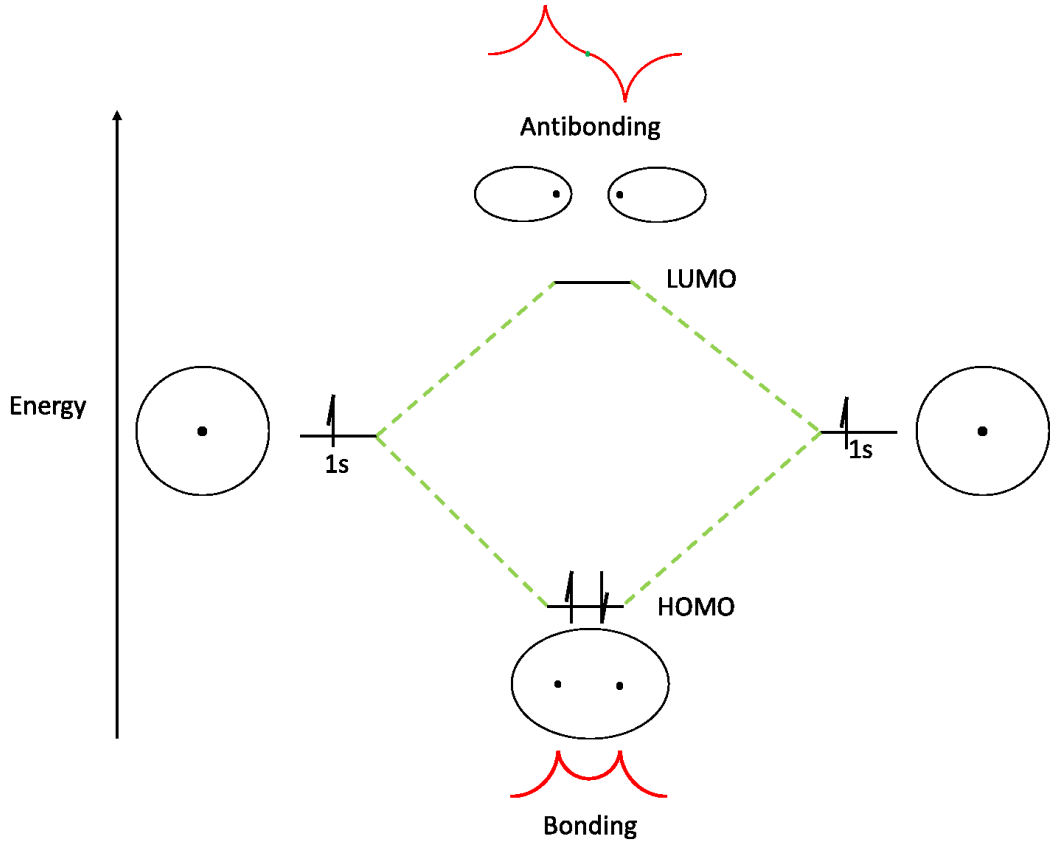

Figure 2.9 The energy diagram illustrating two hydrogen atoms bond together to form hydrogen. Two electron wavefunctions that are in phase will form an occupied bonding orbital (HOMO). Two electrons wavefunctions that are out of phase will form an unoccupied antibonding orbital (LUMO)

2.1.6 Hopping transport mechanism in organic semiconductor

Within the same molecule, carriers are mobilized within the same orbital. Take an asymmetric organic small molecule 1-ethylanthracene as an example (Figure 2.10a). Electrons are delocalized within the benzene ring because of the conjugation of π electrons. However, when charge carriers reach the end of the molecule, delocalization of electron is unlikely to happen between molecules because the range of intermolecular

separation is large (about 0.5-1nm). The overlapping effect between organic molecules is not significant (Figure 2.10b). Nevertheless, carriers can still be transported by another mechanism, the hopping transport mechanism. Charge transport in disordered system such as organic small molecules and organic polymers are dominated by hopping transport.[46–49]The hopping rate depends on the site energy as shown in Figure 2.11. Such energy states may not be the same for every hopping attempts due to many reasons. For instance, molecular orientation may affect the conformation of the hopping pathway. Also, defects may create trap states that have lower energy then neighboring states, trapping carriers the states when they pass through the molecule.

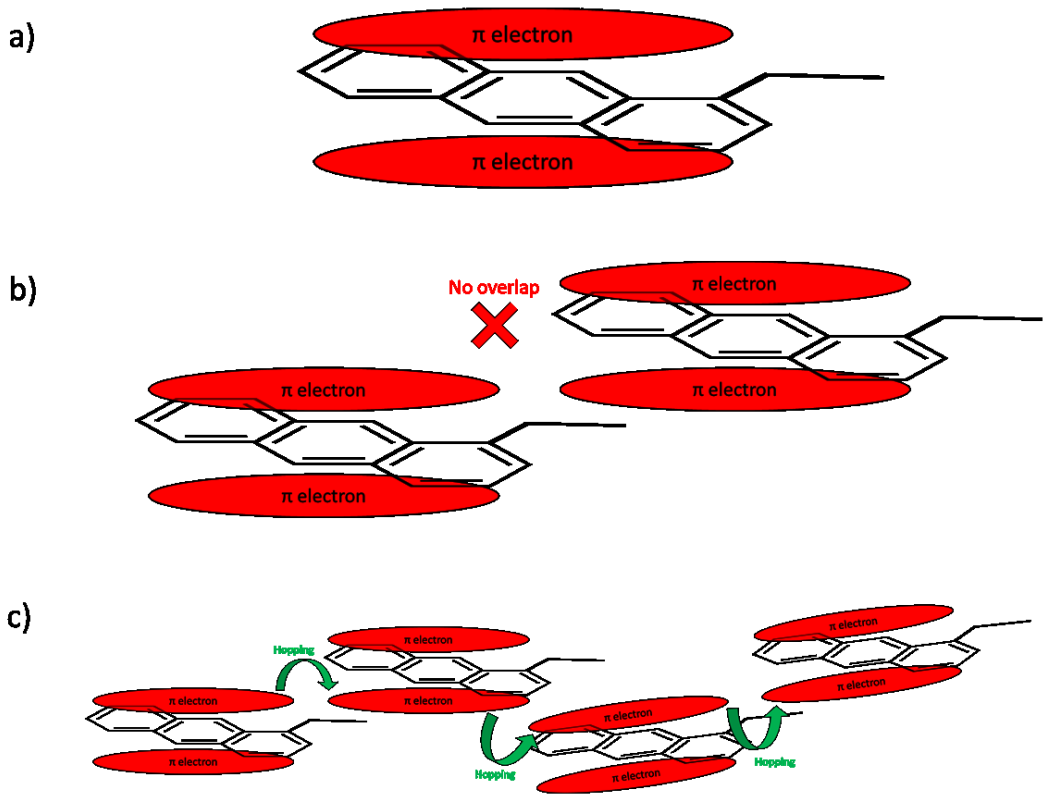

Figure 2.10 a) Molecular structure and delocalized π electron of 1-ethylanthracene. b) When two 1-ethylanthracene molecules are close to each other, the orbital overlap is insignificant. c) Hopping transport is required for carriers to transport between molecules.

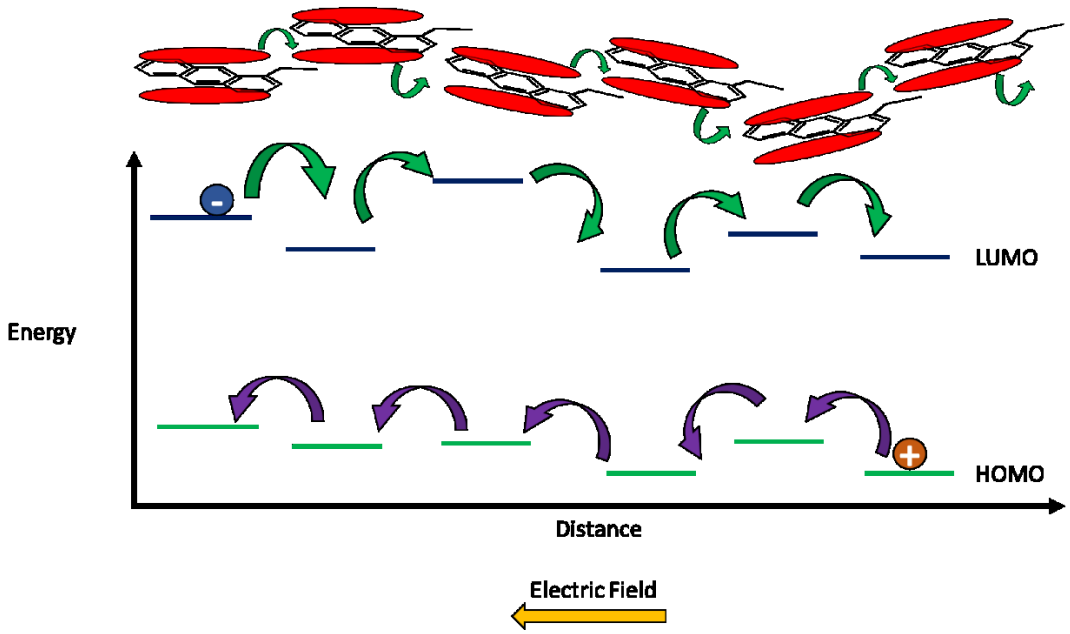

Figure 2.11 Energy distance diagram that illustrates the energy profile for carrier (holes and electrons) to transfer through the organic materials in the presence of electric field.

2.2 Working principles of semiconducting Devices

As discussed before, organic or inorganic semiconductors have a wide range of applications, such as photovoltaic device, light-emitting-diodes, transistors, photodetectors. We will start to discuss about the working principles of some of these devices in the following chapters.

2.2.1 Photovoltaic Device

A photovoltaic device converts light energy, usually from the Sun or indoor light, into electricity. When a photon is absorbed by an organic semiconductor, an electron-hole pair may be formed inside the photoactive material. By extracting those holes and electrons from the organic semiconductor, electrical energy can be harvested. The excited electron-hole pair are separated in a few nanometers and are initially

coulombically bound. Due to the low dielectric constant (ε=3-4) in organic materials, the binding energy of this charge-pair (an exciton) is high (~0.5eV), and is unlikely to separate into free charge carriers with only thermal energy.[50–53] As a result, in single organic materials, most photogenerated excitons tend to recombine to their ground state within a few nanoseconds.[54] In order to improve charge generation, a bilayer heterojunction system is often used.[55] In this system, an additional is material deposited on top (or below) of the photoactive material (Figure 2.12), which is used to aid exciton dissociation by supplying an energetic offset in energy levels with the other material, which drives exciton dissociation. The working principle of a bilayer heterojunction OPV can be divided in five parts. 1) Photon absorption: When the solar cell is under illumination, photons are absorbed in the photoactive material. 2) Exciton formation: Electrons inside the photoactive material absorb photon energy and being excited to form an electron-hole bound state. 3) Exciton recombination and diffusion: Carrier concentration in the photoactive material (shown as donor material in Figure 2.12) is higher than that of acceptor material. Some excitons are attracted to each other and recombined. Some excitons are then diffuse to the interface between the two layers. 4) Charge extraction: Charges reach to their electrode and extracted to the circuit to conduct electricity

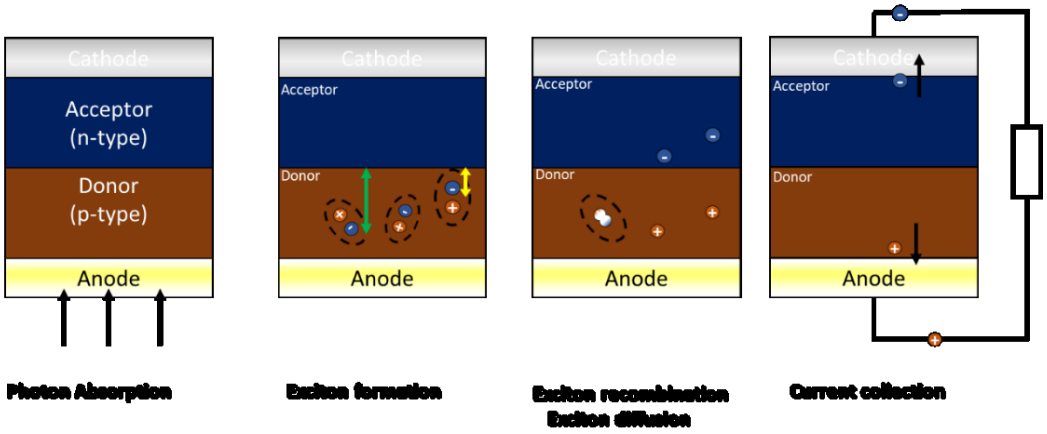

Figure 2.12 Schematic diagram of the working principle of organic solar cell under short-circuit condition in the form of energy diagram. a) Photon absorption, b) Exciton formation, c) Exciton recombination, d) Current collection

2.2.1.1 Photon Absorption

The absorbed intensity of the light, is directly proportional to the number of molecules, *N*, inside the semiconductor and its remaining intensity, *I*, that is

$$\frac{\mathrm{d}I}{dx} = -kNI \tag{2.12}$$

where *x* is the direction of the light travel and *k* is a proportionality constant.

Integrating (2.8) could yield the Lambert-Beer Law,

$$I = I_0 e^{-kNx} = I_0 e^{-\alpha x} \tag{2.13}$$

where α is the absorption coefficient and it varies at different wavelength. Absorption coefficient it is a parameter that depends on wavelength and shows the ability for a material to absorb light. The higher the absorption coefficient, the more light is absorbed. Table 2.3 shows the absorption coefficient at 550nm of silicon and the materials we used in this thesis.

Materials	**Absorption coefficient (at 500nm) [cm^{-1}]**
CuSCN	7×10^2
$PC_{70}BM$	2×10^4
$PC_{60}BM$	5×10^3
Silicon	1×10^4

Table 2.3 Absorption coefficient of CuSCN, $PC_{70}BM$, $PC_{60}BM$ and silicon at wavelength of 550nm

2.2.1.2 Radiative photogeneration of charge

When light is absorbed by the semiconductor, its energy is given by

$$E = h\nu \tag{2.14}$$

where h is the Planck constant and ν is the frequency of the photon. For a direct bandgap semiconductor, the highest point of the VB is directly below the lowest point of CB as shown in Figure 2.9a. When the photon energy is higher than the energy band gap or the difference in HOMO and LUMO energy levels, electrons in the valence band/HOMO can be excited to the conduction band/LUMO. At the same time, the escaped electron will leave a hole in the conduction band/LUMO. The photoexcited electron will then become mobile. As a result, charges can flow through the semiconducting device. On the other hand, for indirect bandgap semiconductor, the highest point of VB is not directly below of CB as shown in Figure 2.13b. Extra momentum is required from the vibration of the crystal lattice. Such crystal lattice will provide a quasi particle called phonon. When light is absorbed by the photoactive material, electron will be excited, and gain momentum from phonon such that it can reach the lowest point of the conduction band. Such excited electron is then being transported though the photovoltaic device. Since an extra phonon is required for the excitation of indirect bandgap semiconductor, the light absorption for such material is not as efficient as in direct bandgap semiconductor.

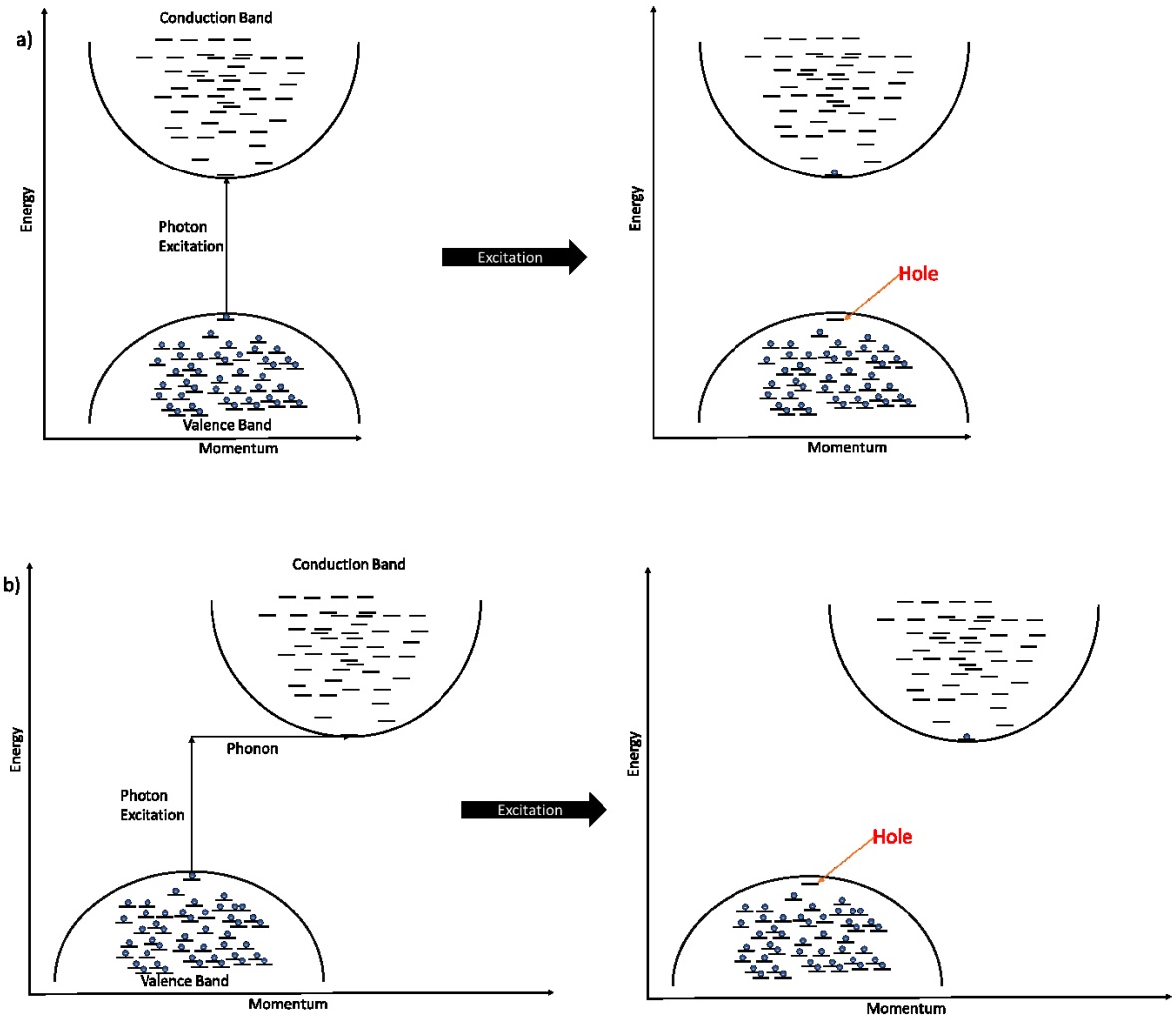

Figure 2.13 a) Excitation of a direct band gap material. The valence band maximum is directly below the conduction band minimum. Electron can be excited to the conduction band minimum and leaving a hole in the valence band. b) Excitation of an indirect band gap material. The valence band maximum is not directly below the conduction band minimum. A phonon is required to provide the change in momentum for the electron to be excited from valence band maximum to conduction band minimum.

2.2.1.3 Recombination of charge

After charges are excited, some of the charge will undergo recombination such that the photon electron conversion is unlikely to be 100%.[56–58] Recombination highly changes the performance of a solar cell. High recombination rate will case the

reduction of the collected current. Nevertheless, in practice, recombination rate is lower than photogeneration rate by a few orders of magnitude so that photogenerated carriers can be collected in the electrodes to produce electric current.[54] There are many reasons to cause recombination. For example, after an exciton, a bound state between a hole and an electron, is excited by a photon, the coulombic interaction is needed to overcome to prevent recombination. The coulombic force F is given by

$$F = -\frac{1}{4\pi\varepsilon_o\varepsilon_r}\frac{e^2}{r^2} \tag{2.15}$$

where ε_0 is the dielectric permittivity of free space, ε_r is the relative permittivity of the material, e is the elementary charge and r is the separation between two charges. Silicon has ε_r of about 11 and organic semiconductor is usually around 3-4. That means the coulombic interaction between holes and electrons in organic materials are 3-4 times stronger than in silicon, making the recombination rate higher.

In organic photovoltaic device, donor-acceptor planar heterojunction (PHJ) and bulk-heterojunctions (BHJ) configuration is often used. PHJ contains two separate layers and one of them is n-type (acceptor) that transports electrons and the other one is p-type (donor) that transports holes. Such film is usually fabricated by sequential evaporation or spin-coating deposition. On the other hand, a BHJ has a finely intermixed morphology of both donor and acceptor layers which usually gives better performance in devices. [59–62] It is usually fabricated by spin coating a pre-mixed donor and acceptor material. Figure 2.14 a and Figure 2.14 e shows the nanostructure of PHJ and BHJ. In general, BHJ solar cells display a better performance there is improved photo-charge generation compared to a PHJ, which arises due to its

morphology. If the diffusion length of the excitons is short, as it generally is in organic semiconductors (~10 nm) the excitons are likely to recombine (Figure 2.14b and Figure 2.14f) if the donor-acceptor interface is small, such as in a PHJ. In a BHJ, the interfacial area between the donor and acceptor materials can be increased significantly, and there are no large domain sizes of either material. The required diffusion pathway is therefore reduced and therefore the rate of exciton recombination can be reduced, leading to a large increase in the number of photogenerated carriers.

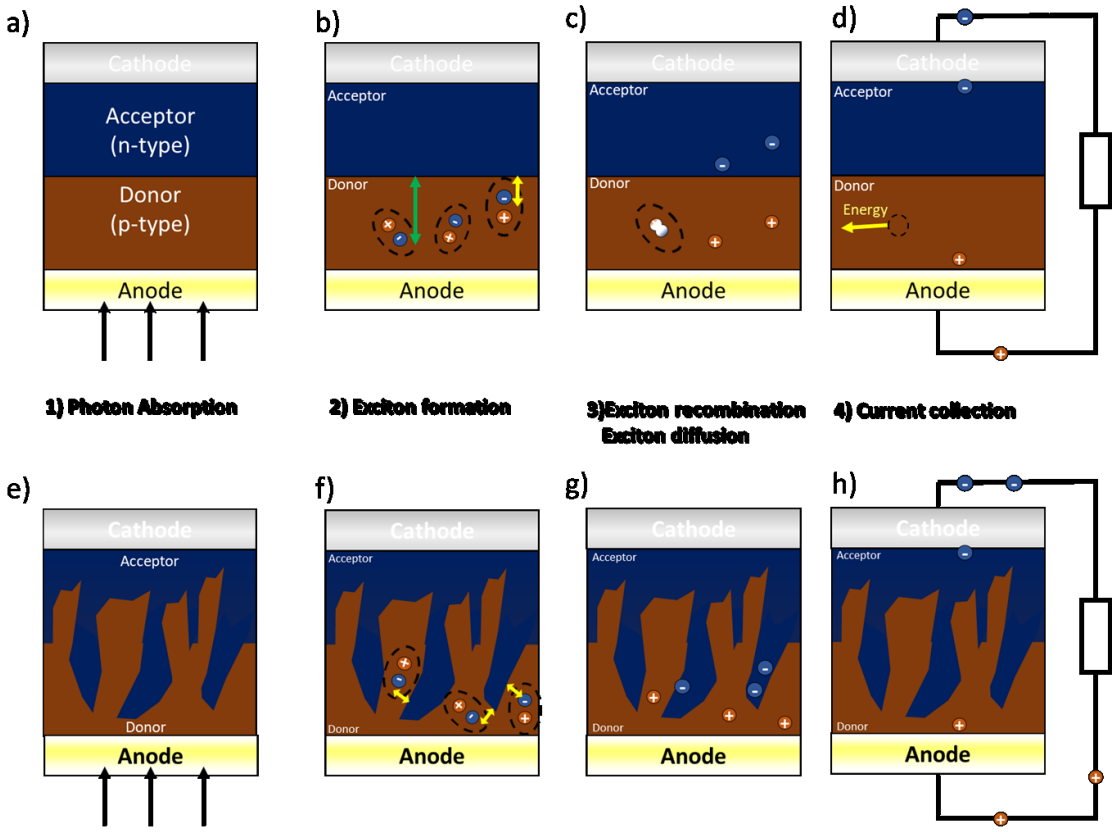

Figure 2.14 a) cross-sectional device structure of a PHJ device b) Exciton formation inside a PHJ system. The green arrow and yellow arrow show the long and short diffusion length, respectively. c) Exciton recombination and diffusion occurring inside PHJ device. Excitons that cannot reach the interface will eventually recombined. d) Electric current flows through the circuit whilst recombined exciton will release heat or photon. e) cross-sectional device structure of a BHJ device. f) exciton formation inside a BHJ system. Excitons require shorter diffusion path to reach the interface. g) Exciton diffusion inside BHJ device. h) Higher electric current flows through the circuit.

In general, there are two classifications of recombination, geminate and non-geminate recombination.[56–58] Geminate recombination represents the situation when the recombination occurs between the hole and the electron that are originated from the same photon excitation as shown in Figure 2.15 Once the electron-hole pair reaches the interface, a charge transfer (CT) state will form before becoming free carriers. The coulombic force between them is still in effect in the CT states so it is still possible for them to recombine as a geminate recombination process. After electron-hole pair are separated from each other, the internal electric field caused by the build-in voltage inside the photovoltaic device will help the carriers to accelerate towards their corresponding electrodes. When those free carriers are on their pathway to the electrodes, non-geminate recombination may occur. In general, there are three possible non-geminate recombination mechanisms, namely bimolecular recombination, trap-assisted recombination, and auger recombination.

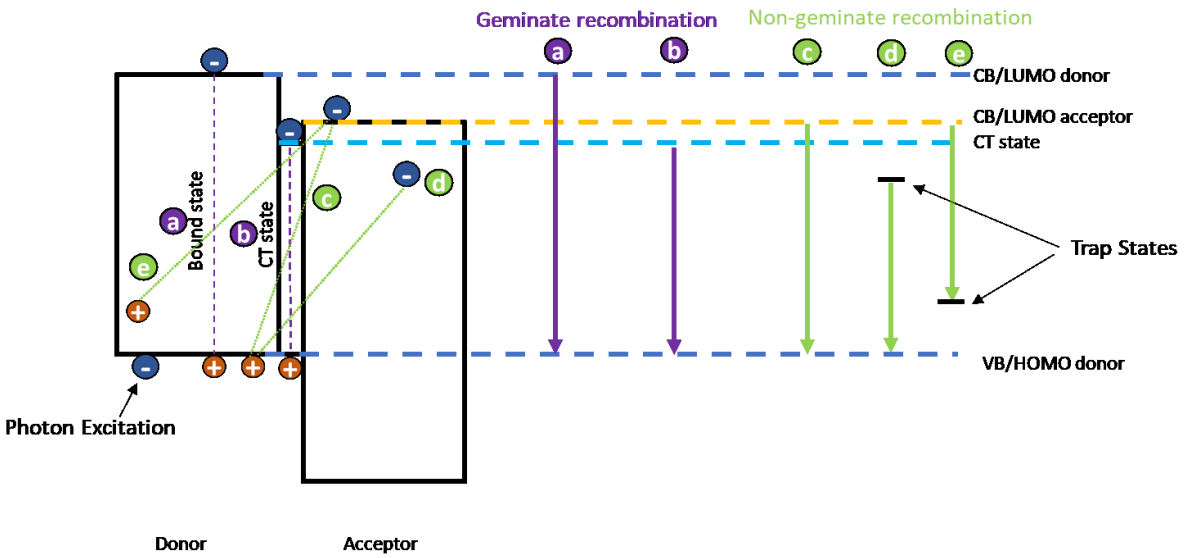

Figure 2. 15 Recombination processes in photovoltaic device. Germinate recombination: a) Recombination of excited bound states after photon excitation b) Recombination of charge transfer (CT) state. Non-geminate recombination: c) recombination of free hole and free electron. d) Recombination of trapped electron and a free hole. e) Recombination of free electron and trapped hole.

2.2.1.4 Bimolecular recombination

Bimolecular recombination occurs when a free electron recombines with a free hole. That means the electron and the hole are not excited from the original photon. Bimolecular recombination rate can be described by the Langevin expression,[58]

$$R_{Langevin} = \frac{q}{\varepsilon}(\mu_p + \mu_n)(np - n_i^2) \qquad (2.16)$$

where q is elementary charge, ε is the permittivity of the material, μ_p is the hole mobility in the donor, μ_n is the electron mobility in the acceptor, n is the charge density of electron, p is the charge density of holes, and n_i is the intrinsic carrier concentration. The higher the mobility of holes or electrons, the higher the bimolecular recombination rate.

2.2.1.5 Trap-assisted recombination

Trap-assisted recombination takes place when a hole or electron is trapped in a trap state. The trap states for hole and electron have higher energy and lower energy, respectively, than the valence and conduction bands. Once one of the carriers is trapped, the opposite carrier will be able to recombine with the trapped carrier once they find each other. This kind of trapping mechanism is also known as the Shockley-Read-Hall (SRH) recombination. The rate of the SRH recombination is given by[57]

$$R_{SRH} = \frac{C_n C_p N_{trap}(np - n_i^2)}{[(C_n(n + n_1)C_p(p - p_1)]} \tag{2.17}$$

where C_n and C_p are the probability that an electron or a hole can be trapped per unit time, N_{trap} is the trap density of electron traps. The parameters n_1 and p_1 are given by

$$n_1 = n_i e^{\frac{(E_T - E_c)}{k_B T}} \tag{2.18}$$

and

$$p_1 = n_i e^{\frac{(E_V - E_T)}{k_B T}} \tag{2.19}$$

where E_c is the energy of lowest conduction band level and E_v is the energy of highest valance band level. As a result, the rate of SRH recombination depends on the amount of trap states in both donor and acceptor in organic semiconductor.

2.2.1.6 Auger recombination

Auger recombination is a process of trimolecular recombination because it involves three charge carriers. In Auger recombination, one electron in CB/LUMO recombines

with a hole in VB/HOMO and releases energy. Such energy and momentum are then transferred to another particle. If this particle is an electron, then the electron will be excited into higher level in the CB/LUMO. On the other hand, if this particle is a hole, this hole will be excited into lower energy level in the VB/HOMO. Eventually both particles will return to the ground state. The energy eventually dissipated as heat. The rate of Auger recombination is given by two separate variables, R_{eeh} and R_{ehh}. R_{eeh} or R_{ehh} become significant when electrons or hole is the majority charge carrier respectively[54]

$$R_{eeh} = C_n n^2 p \tag{2.20}$$

and

$$R_{ehh} = C_p n p^2 \tag{2.21}$$

where C_n and C_p are the proportionality constant that depend on temperature.

The Auger recombination rate is given by

$$R_{Auger} = R_{eeh} + R_{ehh} = C_n n^2 p + C_p n p^2 \tag{2.22}$$

In an indirect bandgap semiconductor, electron transition requires the change in momentum. As a result, in such semiconductor the recombination will be dominated by Auger recombination.

2.2.1.7 Solar Spectra

According to Planck's law, the spectral radiance of an object in thermal equilibrium is given by

$$R = \frac{2hc^2}{\lambda^5} \frac{1}{e^{\frac{hc}{\lambda k_B T}} - 1} \tag{2.23}$$

where λ is the wavelength and k_B is the Boltzmann constant. Assuming the temperature at the surface of the Sun is 5778K and that it is a perfect blackbody, which absorbs all incoming light, then the spectral radiance is shown in Figure 2.16 (solid black line). However, when sunlight is passing through the atmosphere, the spectra will be attenuated due to various reasons. For example, part of the light can be reflected or absorbed by the air molecules in the atmosphere of the Earth. Gas molecules surrounding the Sun will also absorb part of the light. Thus, the solar spectra measured on Earth is given by the red line in Figure 2.16. The amount of incident light is the greatest when the sun is at directly overhead. The angle between the sun and zenith defines the optical air mass (AM) as shown in Figure 2.17. The optical air mass is given by

$$AM = \frac{1}{\cos\theta} \tag{2.24}$$

where the θ is the angle between zenith and the sun. For example, θ=0^o (i.e. directly above head) represents AM1. The typical air mass AM1.5 is defined with the angle θ=48.2 ^{o} AM1.5, which is generally used along with other standard test conditions, irradiance of 1000Wm^{-2} and cell temperature of 25^{o}C are used as a reference condition for photovoltaic cell testing.

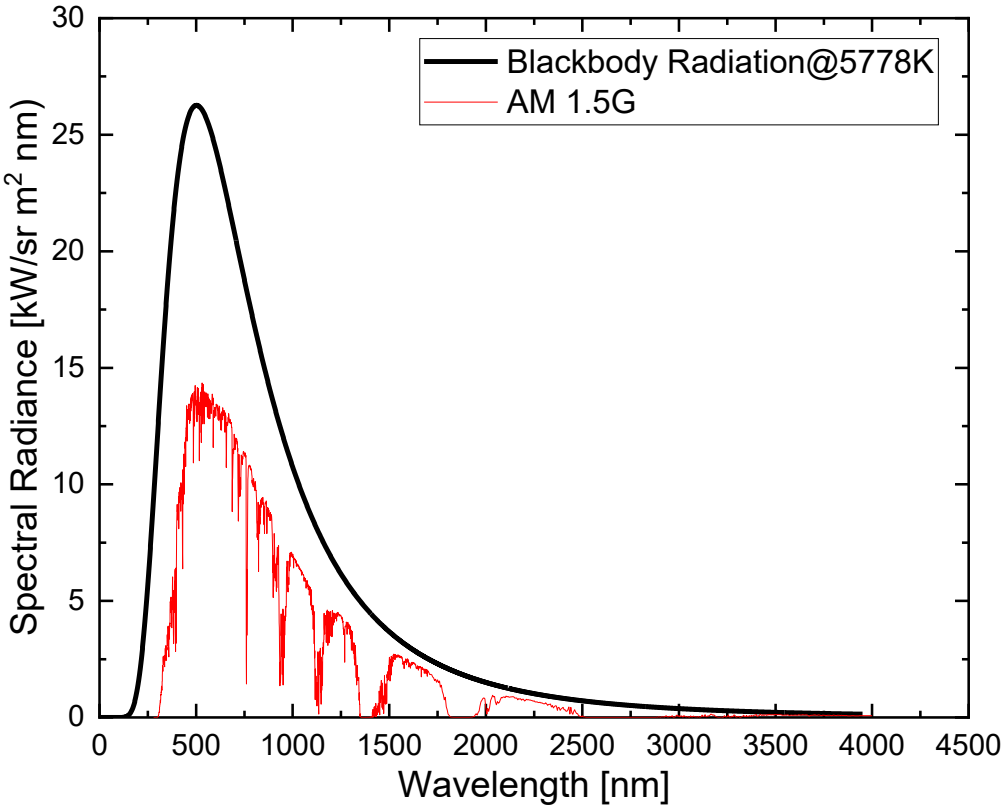

Figure 2.16 The relationship between the spectral radiance against wavelength. The black solid spectra show the simulated ideal black body radiation of the Sun at 5778K. The red line represents the AM1.5 spectra measured at the surface of the Earth.

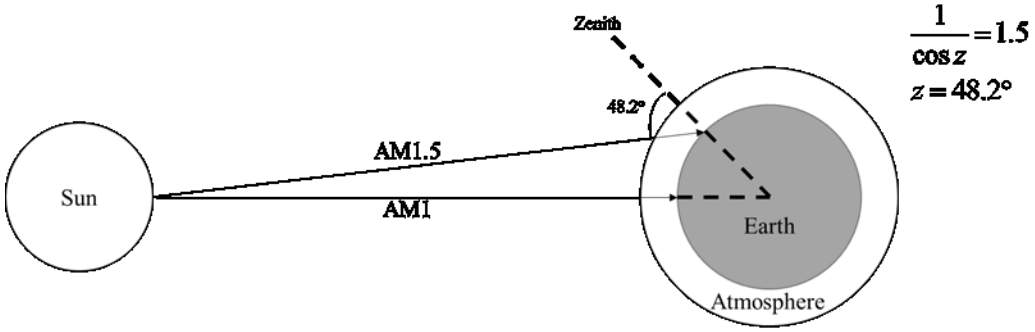

Figure 2.17 Schematic diagram of illumination direction of AM1 and AM1.5G

2.2.1.7 Current density-voltage characteristics

To characterize the performance of a solar cell, current density-voltage (*J-V*) characteristics are generally measured. The current inside solar cell is measured when both electrodes are given a negative bias to positive bias (Forward scan). Without the illumination of light, the solar cell should behave as a diode as shown in Figure 2.18. When the device is under illumination of light, ideally the AM1.5 spectra, the measured curve will be shifted down. The *y*-intercept is the short-circuit current, $J_{sc,}$ and the *x*-intercept is the open circuit voltage, V_{oc}. We can then measure fill factor (FF) and power conversion efficiency (PCE) using the J-V characteristics, which will be discussed briefly in the section below.

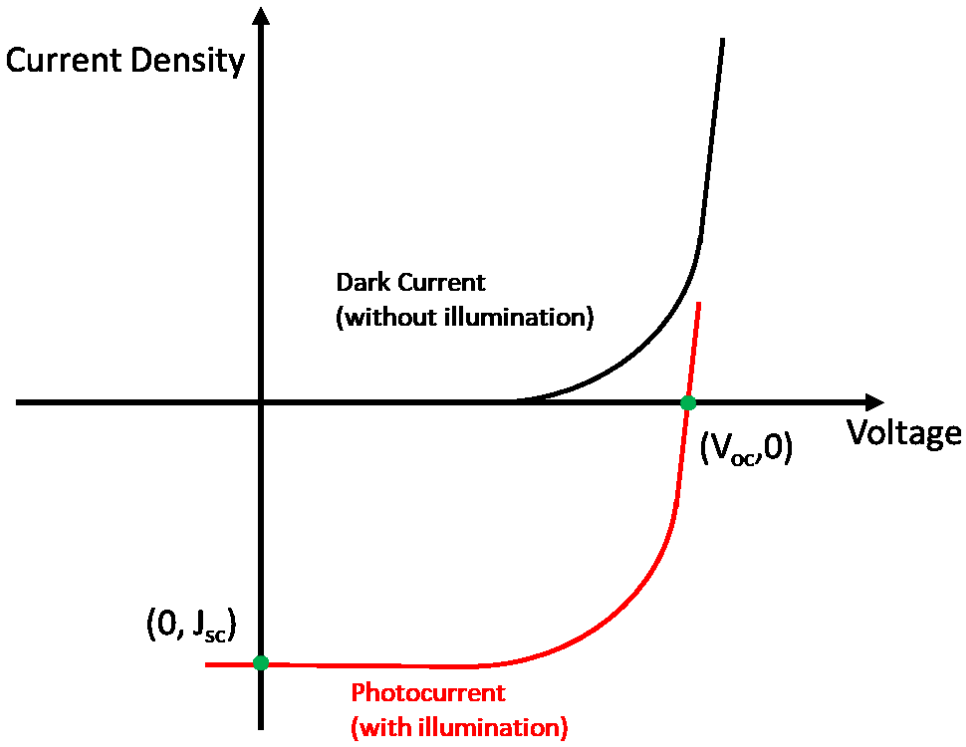

Figure 2.18 J-V characteristics of a solar cell. The black curve represents the current measured in dark condition whilst the red curve represents the photocurrent. Under

illumination, the y-intercept represents the short-circuit current, J_{sc}, while the x-intercept represents the open-circuit voltage (V_{oc}).

2.2.1.8 Short circuit current density

The short circuit current, I_{sc} is the current collected form a solar cell when it is in short circuit as shown in Figure 2.19, i.e. when the applied voltage is zero. The short circuit current density is defined by

$$J_{sc} = \frac{I_{sc}}{A} \tag{2.25}$$

where A is the device area. The short-current density is often used to measure the maximum current can be delivered by the solar cell device. This value is strongly related to light intensity as the photocurrent is originated from free charge carrier by photon excitation. Ideally, if there is no recombination the short circuit current should be equal to the photogenerated current J_{ph}.

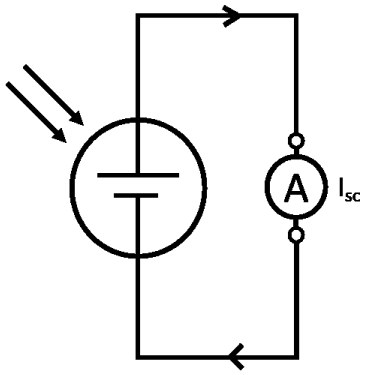

Figure 2.19 Schematic diagram of how short circuit current is measured.

2.2.1.9 Open-circuit voltage

The open circuit voltage, V_{oc} is the voltage across the device electrodes when no current flows through the device as shown in Figure 2.20. It is the maximum voltage can be delivered by the solar cell. The V_{oc} is given by[63]

$$V_{oc} = \frac{k_B T}{q} \ln\left(\frac{J_{ph}}{J_0} + 1\right) \tag{2.26}$$

where J_{ph} is photogenerated current density and J_0 is the dark saturation current density. Again, the open circuit voltage depends on the photogenerated current density, J_{ph}.

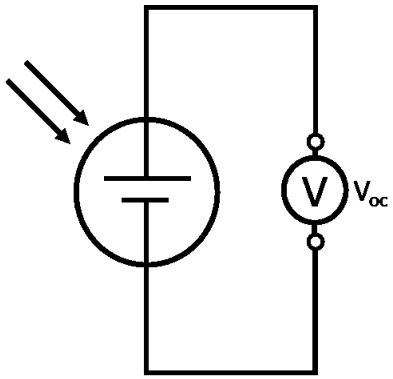

Figure 2.20 Schematic diagram of how open-circuit voltage is measured.

2.2.1.10 Fill factor

The fill factor is the ratio between the maximum power output and the product of open circuit voltage and short circuit current. The maximum power output is the point in the current-voltage characteristics curve (*J-V* curve) that generates the maximum power per unit device area. That is

$$FF = \frac{P_{\max}}{V_{oc} J_{sc}} = \frac{V_{\max} J_{\max}}{V_{oc} J_{sc}} \qquad (2.27.$$

Figure 2.21 shows a graphical interpretation of FF. The fill factor is the ratio of the point that delivers maximum power from the solar cell to the product of J_{sc} and V_{oc}

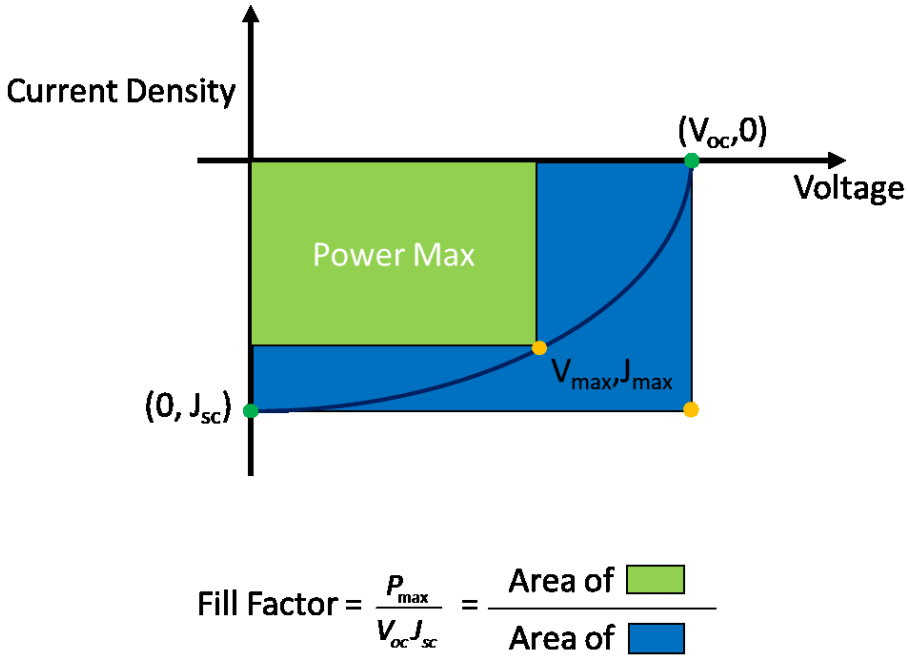

Figure 2.21 The current-voltage characteristics curve of a solar cell. Fill factor is calculated by the ratio of maximum power point per unit device area to the product of open circuit voltage and short circuit current. That is the ratio of the green area to the blue area.

2.2.1.11 Power Conversion Efficiency

Power conversion efficiency (PCE) is the ratio of electrical power harvested to the light power provided by the Sun. The PCE is given by

$$PCE = \frac{P_{\max}}{P_{in}} = \frac{J_{\max} V_{\max}}{P_{in}} = \frac{J_{sc} V_{oc} FF}{P_{in}} \quad (2.28$$

For example, a PCE of a solar cell with 22.8% efficiency means for every 100J of photon energy passing through such device, approximately 22.8J of electricity is harvested when operate at the maximum power point.[54]

2.2.1.12 External quantum efficiency

We can also characterize the photon-electron conversion ratio by using the wavelength dependent external quantum efficiency (EQE). It measures the ratio between the number of photons, n_{photon} passing through the device to the number of carriers n_{charge} successfully collected in the circuit at different incident wavelength, which is

$$EQE(\lambda) = \frac{n_{charge}}{n_{photon}} \quad (2.29.$$

Figure 2.22 shows a typical EQE spectra of a photovoltaic device. Short-circuit current density of the device can be calculated once we obtain the EQE spectra using the following relationship,[64]

$$J_{sc} = -q\int_{\lambda_1}^{\lambda_2} EQE(\lambda)\Phi_{AM1.5}(\lambda)d\lambda \quad (2.30$$

where $\Phi_{AM1.5}(\lambda)$ is the AM spectral photon flux of AM1.5.

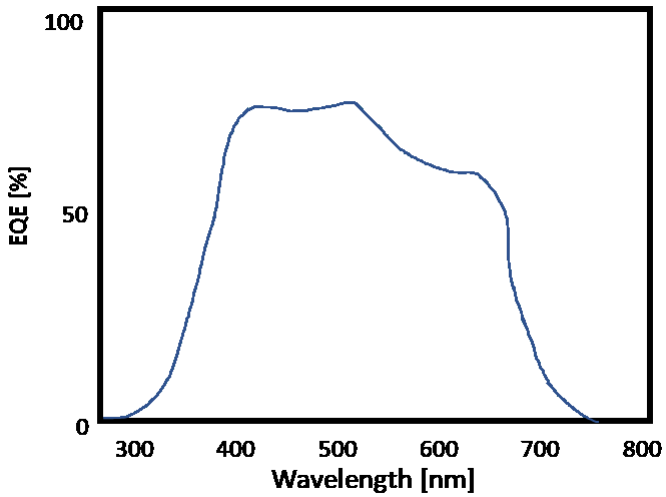

Figure 2.22 Illustrative diagram of EQE spectra of photovoltaic device.

2.2.2 Field effect transistors

The unipolar field effect transistor (FET) was first proposed by W. Shockley in 1952. It is also called thin film transistor (TFT) because the size of such transistor can be as thin as 100nm or less.[65] The development of transistor is then become a key role in integrated circuit as it is a key component in central processing unit (CPU). It is also a key component for most of the electronic devices like LEDs displays. Tsumura et. al reported the organic thin film transistor (OFET) using polythiophene in 1986.[66] Since then, the development of organic thin film transistors have shown its potential to become an cheap and flexible alternative of inorganic thin film transistors. There are reports that used OFETs as pressure and explosives sensors with high sensitivity.[67,68] OFETs have also proven to be highly useful in measuring the carrier mobility of semiconductors. This is because thick films (500μm~1μm) are usually required for testing mobility values using other techniques such as time-of-flight, which can be difficult to achieve using common solution processing techniques.[69,70] With OFETs, one can measure the intrinsic mobility with films of about 10-50nm thicknesses, which also reduces the amount of consumption of synthesized materials and may be more reflective of the thickness of actual devices.[71,72]

2.2.2.1 Structure and working principle of FETs

Figure 2.23 shows a structure of top-gate bottom-contact (TGBC) transistor device. Such transistor consists of three parts. 1) Three contact electrodes consisting of source,

drain, and gate electrodes; 2) insulating gate dielectric layer; 3) semiconducting layer.

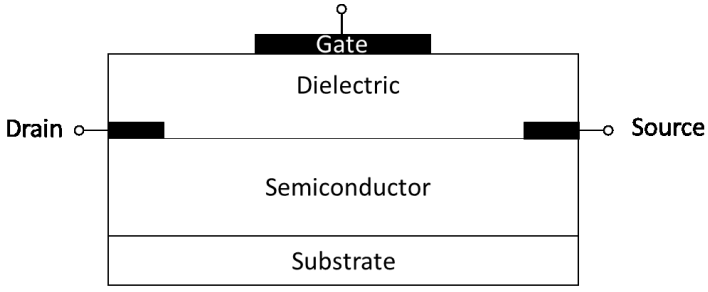

Figure 2.23 Device structure of a bottom-contact top-gate transistor.

In order to operate an FET, a gate voltage (V_g) and drain-source voltage (V_{ds}) are applied to the device. Figure 2.24 shows the working process of an FET. First, free carriers can be induced in the organic semiconductor when gate voltage is applied because of the dielectric layer. The amount of charge induced depends on the dielectric constant, which is given by

$$Q = \varepsilon_r \varepsilon_0 \frac{A}{d} V_g \qquad (2.31$$

where ε_r is the relative permittivity, A is the dielectric area and d is the thickness of the insulating dielectric layer. If V_g is positive, the induced carrier is electron and if V_g is negative, the carrier is hole. However, impurity or defects in the semiconductor could create trap states, which will be trapped by the induced charge. As a result, the semiconducting layer may not be conductive until all trap states are filled. Once V_g is larger than a threshold voltage (V_t), free carriers are accumulated between the source and drain electrodes. Now, a drain voltage (V_{ds}) can be applied between source and drain electrodes to mobilize the charges in the conducting channel and therefore drain current (I_{ds}) can be measured.

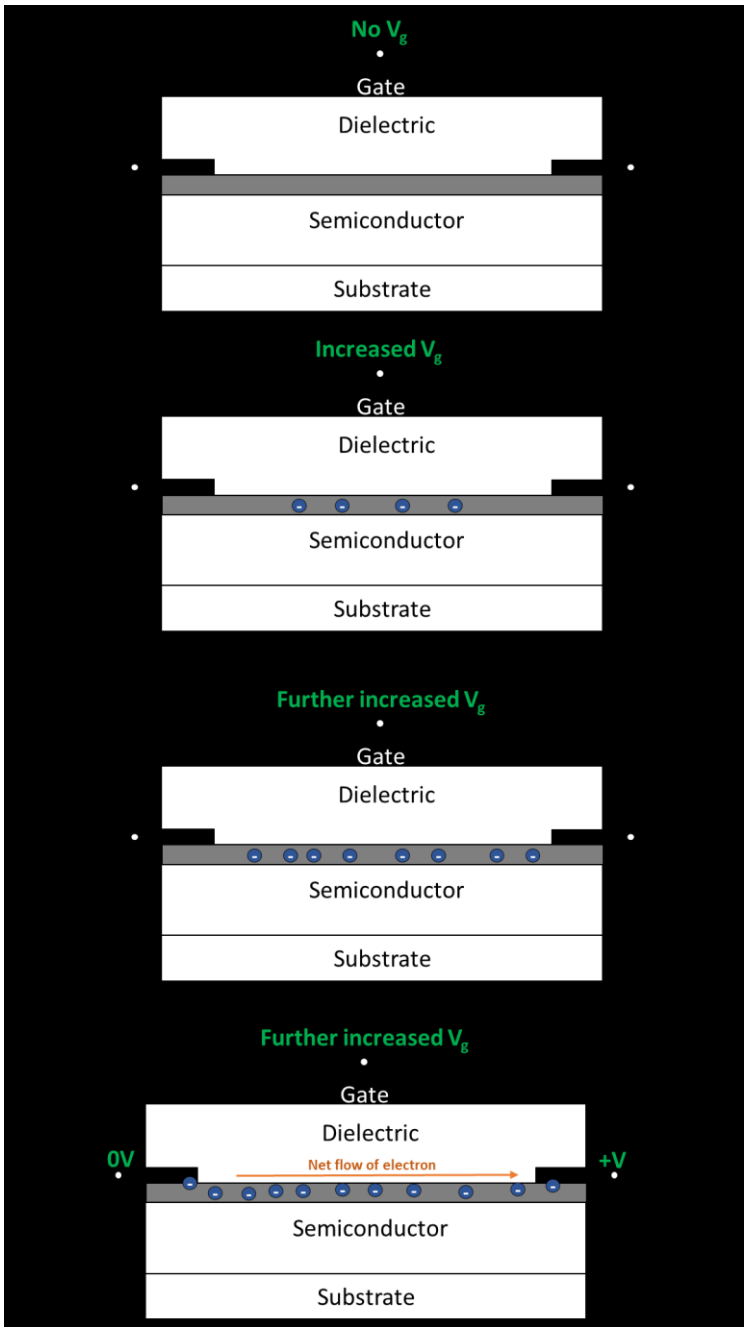

Figure 2.24 Working principle of a FET. The grey region represents the conducting channel. a) No gate voltage (V_g) is applied so no charges are induced in the conducting channel. b) Gate voltage has increased so that negative charges are induced in the conducting channel. c) Gate voltage is further increased, and more charges are induced in the channel. d) A voltage between source and drain electrode is applied and the accumulated charges in the conducting channel can be mobilized. The flow of net charge can be measured as the source-drain current, I_{ds}.

Two types of characteristics can be obtained in FET: Output characteristics and transfer characteristics.

Output characteristics: This characteristic consists of multiple scans of I_{ds} against V_{ds} with at the same gate voltage (V_g) for each scan. At low V_{ds}, I_{ds} is directly proportional to V_{ds} and this is defined to be the linear regime as shown in Figure 2.25. Then when V_{ds} is comparable to V_g, the voltage drop at drain contact will become zero and the conducting channel is pinched off . This region is defined as the saturation regime.

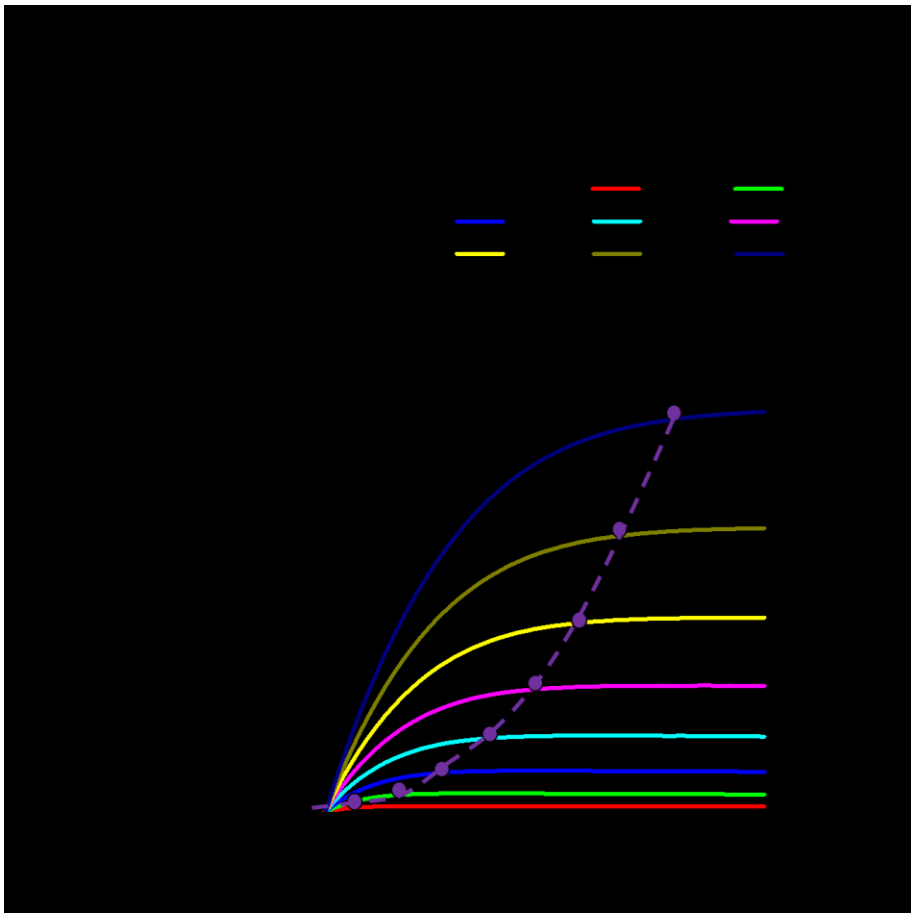

Figure 2.25 Typical output current-voltage characteristics from FET measurements of a hole only device.

Transfer characteristics (Figure 2.26): To obtain the transfer characteristics, V_{ds} is pre-chosen such that it is either in linear regime (low voltage) or in saturation regime (high voltage). For instance, in Figure 2.21, V_{ds}=-20V or V_{ds} =-100V was used as linear regime and saturation regime, respectively. At such constant V_{ds}, the I_{ds} is measured at different V_g.

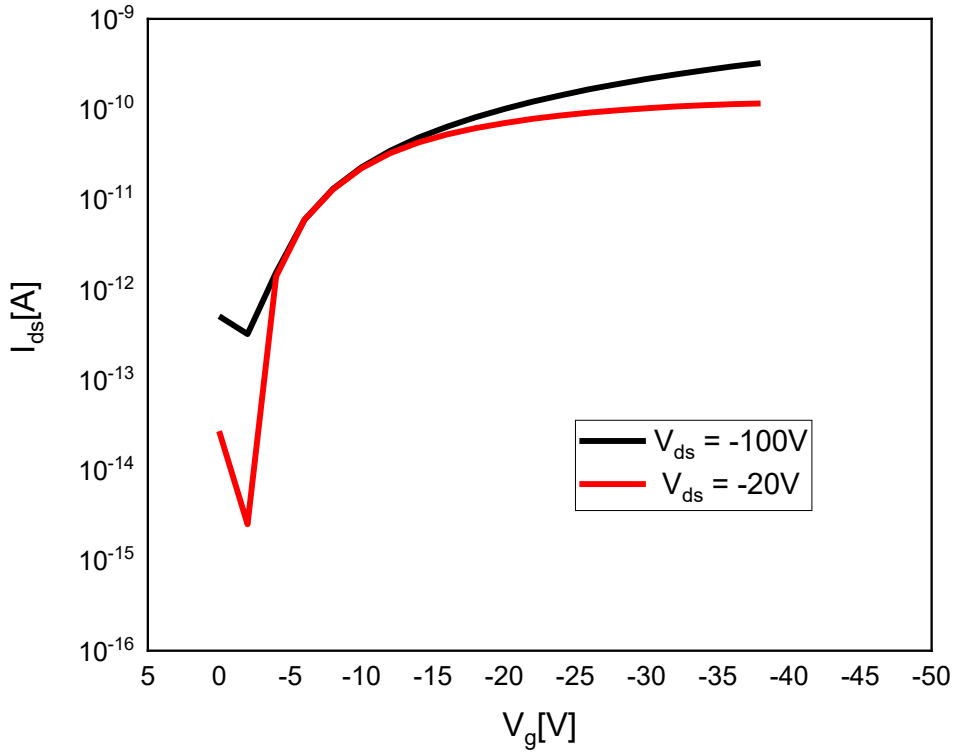

Figure 2.26 Transfer characteristics of a FET device with V_{ds} at -20V for linear regime and -100V for saturation regime.

Both output and transfer characteristics allow us to obtain the carrier mobility inside the organic semiconductor, which will be discussed in the next section.

2.2.2.2 Extraction of carrier mobility using FETs

To derive the equations, we need to extract carrier mobility from FET

measurements, a few assumptions are made: 1) Leakage current in negligible; 2) The direction of electric field has only one direction, which is from source to drain electrodes; 3) the semiconducting material has even thickness and homogeneous; iv) carrier mobility is constant in the semiconductor.[26,27]

After applying V_g and V_{ds} in the thin film transistor, the induced charges Q at the semiconductor is proportional to the potential difference V_g-$V(x)$ where $V(x)$ is the potential at position x under the influence of V_{ds}.

$$Q = C[V_g - V_t - V(x)] \tag{2.32}$$

where C is the capacitance of the gate dielectric layer and V_t is the threshold voltage. For a small V_{ds}, the mean induced charge density $\bar{Q}$ is equal to the induced charge density at the middle of the conducting channel:

$$Q = \bar{Q} = C(V_g - V_t - \frac{V_{ds}}{2}) = nqAt \tag{2.33}$$

where n is the carrier concentration, A is the device is the cross-section area of the device, and t is the film thickness. If we divide both sides by area, we obtain

$$\frac{Q}{A} = C_i(V_g - V_t - \frac{V_{ds}}{2}) = nqt \tag{2.34}$$

where C_i is the capacitance per unit area of the gate dielectric layer. By Ohm's law and the definition of current density, we can correlate V_{ds} and I_{ds},

$$J = \sigma E = \sigma \frac{V_{ds}}{L} = \frac{I_{ds}}{Wt} \tag{2.35}$$

where J is the current density, σ is the conductivity of the conducting channel, E is the electric field between the source and drain electrodes, L is the channel length, W is the channel width and t is the film thickness. By the definition of conductivity,

$$\sigma = qn\mu \tag{2.36}$$

Combining (2.30), (2.31), and (2.32), we obtain

$$I_{ds} = \frac{W}{L}\mu C_i\left[(V_g - V_t)\mathrm{V}_{ds} - \frac{V_{ds}^{\ 2}}{2}\right] \tag{2.37}$$

Considering the linear regime, where V_{ds} is small, that implies $V_{ds} << V_g - V_t$. As a result, (2.33) is simplified as

$$I_{ds} = \frac{W}{L}\mu_{lin} C_i(\mathrm{V}_g - V_t)V_{ds} \tag{2.38}$$

where μ_{lin} is the carrier mobility in the linear regime.

In contrast, if we consider the saturation regime, when the device carrier concentration starts to pinch-off the following expression holds,

$$V_{ds} = V_g - V_t \tag{2.39}$$

and (2.33) becomes

$$I_{ds} = \frac{W}{2L}\mu_{sat} C_i(\mathrm{V}_g - V_t)^2 \tag{2.40}.$$

As a result, we can obtain the carrier mobility from the output characteristics or the transfer characteristics in both linear and saturation regime.

2.2.2.3 Other architectures of FETs

In the previous sections, we have use TGBC device as example to illustrate the theory of FETs. In practice, there are four possible configurations of FETs as shown in Fig. 2.27. They are top-gate bottom-contact (TGBC), top-gate top-contact (TGTC), bottom-gate top-contact (BGTC), and bottom-gate bottom-contact (BGBC). BGTC and TGBC are commonly used in research field because of the straightforward processing method. Although BGBC wafer using SiO_2 as the dielectric layer is commercially available and only the deposition of semiconductor is required, which is continent to conduct quick test on materials. However, contact and wetting issue makes it not ideal to optimize FET system.

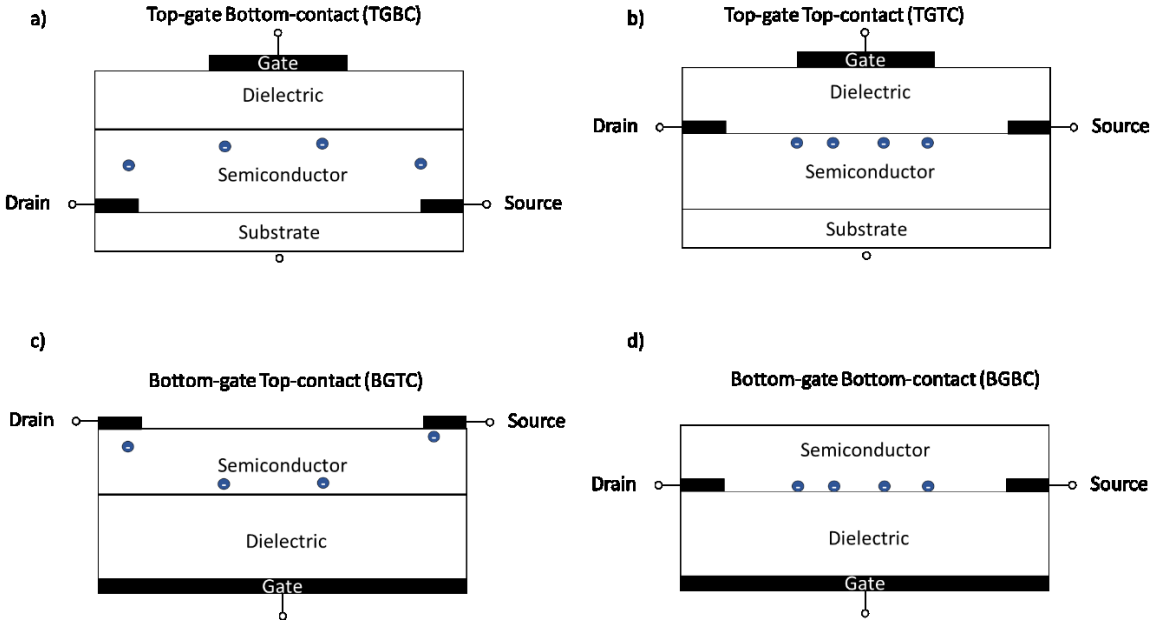

Figure 2.27 Four different configurations of field effect transistors: a) Top-gate bottom-contact (TGBC) b) Top-gate top-contact (TGTC) c) Bottom-gate top-contact (BGTC) d) Bottom-gate bottom-contact (BGBC).

2.2.2.4 Charge transport direction

Although a FET is a convenient technique for measuring mobility of semiconducting material, the transport direction in FET is not the same as most of other optoelectronic devices such as photovoltaic devices and light emitting diodes. In PV and LEDs, carriers are transported in the vertical direction whilst charge carriers in FETs travel in the horizontal direction as shown in Figure 2.28. If the semiconducting material is not isotropic, or it forms crystalline structure, the measured carrier mobility in FETs may not be the bulk mobility in device applications.

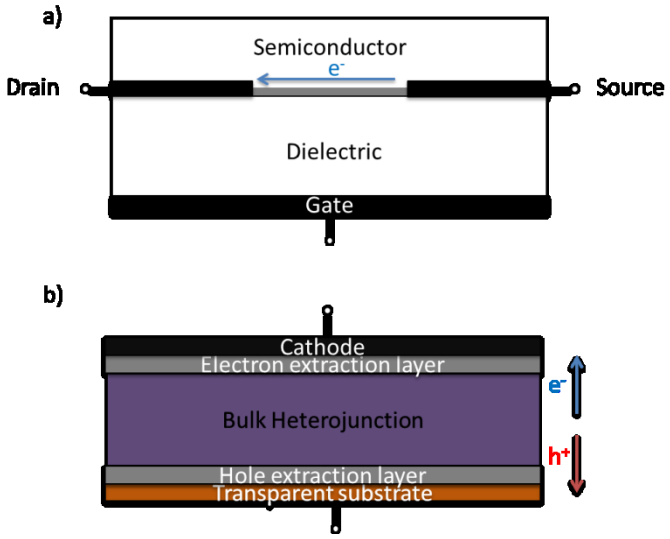

Figure 2.28 Charge transport direction in a) OTFTs and b) OPVs

2.2.3 Phototransistor

The development of organic transistors has been widely studied. It has wide range of applications such as toggle switches, current amplifier, sensors, RFID,

photodiodes and phototransistors for microelectronics. [73–80] In this chapter, we will discuss the fundamental concept of phototransistors.

The structure of phototransistor is fundamentally the same as an ordinary transistor as shown in Figure 2.29. The structure is the same as a normal FET. In such device, light will be illuminated to the photoactive semiconducting material, which create free carriers in the conducting channel. Then the source-drain current, I_{DS} can be measured, when a bias is applied in the source-drain electrode.

To characterize the performance of a phototransistors, responsivity (R), photosensitivity (P), and specific detectivity (D^*).[81]

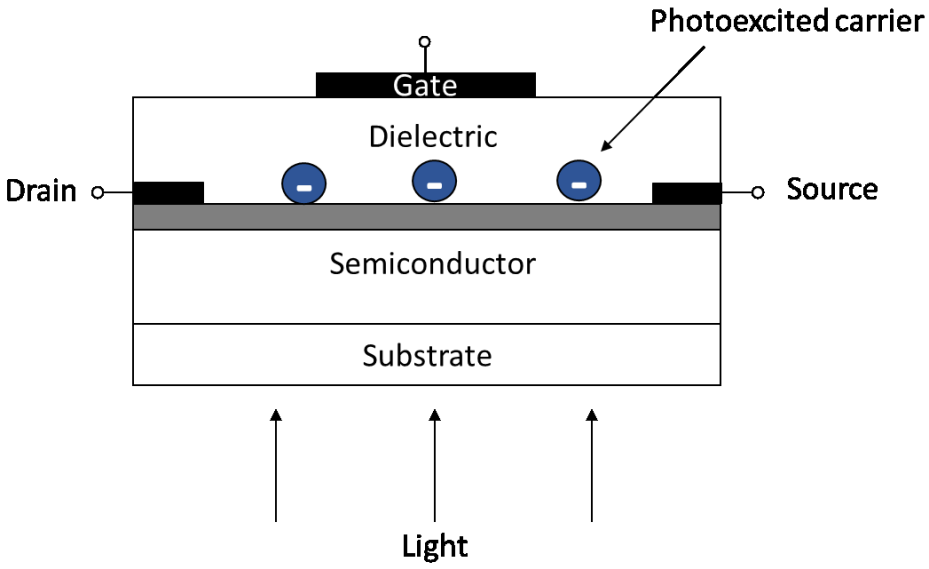

Figure 2.29 Device structure of a TGBC phototransistor.

2.2.3.1 Responsivity

Responsivity, R , is defined as

$$R = \frac{I_{ph}}{P} = \frac{I_{illum} - I_{dark}}{P_{opt}} \quad (2.41)$$

where I_{ph} is the drain photocurrent, *Popt* is the optical power incident on the device, I_{illum} is the drain current under illumination, and I_{dark} is the drain current in dark condition.

2.2.3.2 Photosensitivity

Photosensitivity, P is often regarded as the signal to noise ratio of the device, which is given by

$$P = \frac{I_{ph}}{I_{dark}} = \frac{I_{illum} - I_{dark}}{I_{dark}} \quad (2.42).$$

2.2.3.3 Detectivity

Detectivity is defined as

$$D* = \frac{\sqrt{a}R}{S_{noise}} \quad (2.43).$$

where a is the area of the device and S_{noise} is the noise spectral density. It is reported that D^* includes multiple sources of noise such as Johnson noise (thermal fluctuation noise), and shot noise. Nevertheless, the shot noise in the dark current is believed to be the major noise to the overall background noise.[82–86] As a result, the shot-noise limited detectivity can be defined as,

$$D^* = \frac{\sqrt{a}R}{\sqrt{2qI_{dark}}} \quad (2.44).$$

Reference

[1] E. M.Purcell, *New Yourk: McGraw-Hill*, **1985,** *Electricity and Magnetism*

[2] J. P.Hurley, C.Garrod, *Phys. Teach.* **1978**, *16*, 408.

[3] C.Jacoboni, C.Canali, G.Ottaviani, A.Alberigi Quaranta, *Solid State Electron.* **1977**, *20*, 77.

[4] P. G.LeComber, W. E.Spear, *Phys. Rev. Lett.* **1970**, *25*, 509.

[5] A. R.Moore, *Appl. Phys. Lett.* **1977**, *31*, 762.

[6] K. I.Bolotin, K. J.Sikes, Z.Jiang, M.Klima, G.Fudenberg, J.Hone, P.Kim, H. L.Stormer, *Solid State Commun.* **2008**, *146*, 351.

[7] A. J.Mozer, N. S.Sariciftci, *Chem. Phys. Lett.* **2004**, *389*, 438.

[8] S.V.Rakhmanova, E. M.Conwell, *Appl. Phys. Lett.* **2000**, *76*, 3822.

[9] L. B.Schein, A.Peled, D.Glatz, *J. Appl. Phys.* **1989**, *66*, 686.

[10] P.Blom, M.deJong, M.vanMunster, *Phys. Rev. B - Condens. Matter Mater. Phys.* **1997**, *55*, 656.

[11] T.Kreouzis, D.Poplavskyy, S. M.Tuladhar, M.Campoy-Quiles, J.Nelson, A. J.Campbell, D. D. C.Bradley, *Phys. Rev. B* **-2006**, *73*, 1. 235201

[12] L. W.Wang, A.Zunger, *J. Chem. Phys.* **1994**, *100*, 2394.

[13] R. L.Mills, *Int. J. Hydrogen Energy* **2000**, *25*, 1171.

[14] W. Pauli Phys. Rev. 58, 716, **1940**

[15] H.Shirakawa, E. J.Louis, A. G.MacDiarmid, C. K.Chiang, A. J.Heeger, *J. Chem. Soc. Chem. Commun.* **1977**, 578.

[16] M.Audenaert, G.Gusman, R.Deltour, *Phys. Rev. B* **1981**, *24*, 7380.

[17] A. J.Heeger, S.Kivelson, J. R.Schrieffer, W. P.Su, *Rev. Mod. Phys.* **1988**, *60*, **781.**

[18] W. H.Koo, S. M.Jeong, F.Araoka, K.Ishikawa, S.Nishimura, T.Toyooka, H.Takezoe, *Nat. Photonics* **2010**, *4*, 222.

[19] Y. J.Lee, S. H.Kim, J.Huh, G. H.Kim, Y. H.Lee, S. H.Cho, Y. C.Kim, Y. R.Do, *Appl. Phys. Lett.* **2003**, *82*, 3779.

[20] T. A.Lin, T.Chatterjee, W. L.Tsai, W. K.Lee, M. J.Wu, M.Jiao, K. C.Pan, C. L.Yi, C. L.Chung, K. T.Wong, C. C.Wu, *Adv. Mater.* **2016**, *28*, 7029.

[21] T.Sekitani, H.Nakajima, H.Maeda, T.Fukushima, T.Aida, K.Hata, T.Someya, *Nat. Mater.* **2009**, *8*, 494.

[22] A.Tsuboyama, Hironobu Iwawaki, Manabu Furugori, Taihei Mukaide, Jun Kamatani, Satoshi Igawa, Takashi Moriyama, Seishi Miura, T.Takiguchi, S.Okada, M.Hoshino, and Kazunori Ueno, *J. Am. Chem. Soc.* **2003**, *125*, 12971.

[23] K. H.Kim, J. L.Liao, S. W.Lee, B.Sim, C. K.Moon, G. H.Lee, H. J.Kim, Y.Chi, J. J.Kim, *Adv. Mater.* **2016**, *28*, 2526.

[24] Y. J.Cheng, S. H.Yang, C. S.Hsu, *Chem. Rev.* **2009**, *109*, 5868.

[25] M.Hiramoto, H.Fujiwara, M.Yokoyama, *Appl. Phys. Lett.* **1991**, *58*, 1062.

[26] A. K. K.Kyaw, X. W.Sun, C. Y.Jiang, G. Q.Lo, D. W.Zhao, D. L.Kwong, *Appl. Phys. Lett.* **2008**, *93*, 1.

[27] W.Li, L.Ye, S.Li, H.Yao, H.Ade, J.Hou, *Adv. Mater.* **2018**, *30*, 1.

[28] L.Meng, Y.Zhang, X.Wan, C.Li, X.Zhang, Y.Wang, X.Ke, Z.Xiao, L.Ding, R.Xia, H. L.Yip, Y.Cao, Y.Chen, *Science (80-.).* **2018**, *361*, 1094.

[29] J.Yuan, Y.Zhang, L.Zhou, G.Zhang, H. L.Yip, T. K.Lau, X.Lu, C.Zhu, H.Peng, P. A.Johnson, M.Leclerc, Y.Cao, J.Ulanski, Y.Li, Y.Zou, *Joule* **2019**, *3*, 1140.

[30] Z.Zheng, Q.Hu, S.Zhang, D.Zhang, J.Wang, S.Xie, R.Wang, Y.Qin, W.Li, L.Hong, N.Liang, F.Liu, Y.Zhang, Z.Wei, Z.Tang, T. P.Russell, J.Hou, H.Zhou, *Adv. Mater.* **2018**, *30*, 1.

[31] J.Zhao, Y.Li, G.Yang, K.Jiang, H.Lin, H.Ade, W.Ma, H.Yan, *Nat. Energy* **2016**, *1*, 2015.**27.**

[32] J.Liu, S.Chen, D.Qian, B.Gautam, G.Yang, J.Zhao, J.Bergqvist, F.Zhang, W.Ma, H.Ade, O.Inganäs, K.Gundogdu, F.Gao, H.Yan, *Nat. Energy* **2016**, *1*, 1.

[33] T.Aernouts, P.Vanlaeke, W.Geens, J.Poortmans, P.Heremans, S.Borghs, R.Mertens, R.Andriessen, L.Leenders, *Thin Solid Films* **2004**, *451–452*, 22.

[34] C.Sekine, Y.Tsubata, T.Yamada, M.Kitano, S.Doi, *Sci. Technol. Adv. Mater.* **2014**, *15*, 034203.

[35] N. M.Boag, M.Green, D. M.Grove, J. A. K.Howard, J. L.Spencer, F. G. A.Stone, *J. Chem. Soc. Dalt. Trans.* **1980**, 2170.

[36] H.Yan, Z.Chen, Y.Zheng, C.Newman, J. R.Quinn, F.Dötz, M.Kastler, A.Facchetti, *Nature* **2009**, *457*, 679.

[37] X.Zhan, D.Zhu, *Polym. Chem.* **2010**, *1*, 409.

[38] Y. C.Chen, C. Y.Yu, Y. L.Fan, L. I.Hung, C. P.Chen, C.Ting, *Chem. Commun.* **2010**, *46*, 6503.

[39] J. W.Jung, F.Liu, T. P.Russell, W. H.Jo, *Energy Environ. Sci.* **2012**, *5*, 6857.

[40] J.Benduhn, K.Tvingstedt, F.Piersimoni, S.Ullbrich, Y.Fan, M.Tropiano, K. A.McGarry, O.Zeika, M. K.Riede, C. J.Douglas, S.Barlow, S. R.Marder, D.Neher, D.Spoltore, K.Vandewal, *Nat. Energy* **2017**, *2*,

[41] J.Ku, Y.Lansac, Y. H.Jang, *Mater. Sci.* **2011**, 21508.

[42] C. F. N.Marchiori, M.Koehler, *Synth. Met.* **2010**, *160*, 643.

[43] P.Morvillo, E.Bobeico, *Sol. Energy Mater. Sol. Cells* **2008**, *92*, 1192.

[44] Y. A.Duan, Y.Geng, H.BinLi, J. L.Jin, Y.Wu, Z. M.Su, *J. Comput. Chem.* **2013**, *34*, 1611.

[45] Y.Kanai, J. C.Grossman, *Nano Lett.* **2008**, *8*, 908.

[46] H.Bässler, G.Schönherr, M.Abkowitz, D. M.Pai, *Phys. Rev. B* **1982**, *26*, 3105.

[47] H.Bässler, *Phys. Status Solidi* **1993**, *175*, 15.

[48] R.Goyena, *J. Chem. Inf. Model.* **2019**, *53*, 1689.

[49] N.Karl, *Synth. Met.* **2003**, *134*, 1026.

[50] D. E.Markov, E.Amsterdam, P. W. M.Blom, A. B.Sieval, J. C.Hummelen, *J. Phys. Chem. A* **2005**, *109*, 5266.

[51] S. R.Scully, M. D.McGehee, *J. Appl. Phys.* **2006**, *100*

[52] P. E.Shaw, A.Ruseckas, I. D. W.Samuel, *Adv. Mater.* **2008**, *20*, 3516.

[53] R. R.Lunt, N. C.Giebink, A. A.Belak, J. B.Benziger, S. R.Forrest, *J. Appl. Phys.* **2009**

[54] C. M.Proctor, M.Kuik, T. Q.Nguyen, *Prog. Polym. Sci.* **2013**, *38*, 1941.

[55] C. W.Tang, *Appl. Phys. Lett.* **1986**, *48*, 183.

[56] B.Walker, C.Kim, T. Q.Nguyen, *Chem. Mater.* **2011**, *23*, 470.

[57] S. R.Cowan, N.Banerji, W. L.Leong, A. J.Heeger, *Adv. Funct. Mater.* **2012**, *22*, 1116.

[58] G.Dennler, M.Scharber, C.Brabec, *Adv. Mater.* **2009**, *096401*

[59] M. C.Scharber, D.Mühlbacher, M.Koppe, P.Denk, C.Waldauf, A. J.Heeger, C. J.Brabec, *Adv. Mater.* **2006**, *18*, 789.

[60] L.Lu, T.Zheng, Q.Wu, A. M.Schneider, D.Zhao, L.Yu, *Chem. Rev.* **2015**, *115*, 12666.

[61] G.Zhang, J.Zhao, P. C. Y.Chow, K.Jiang, J.Zhang, Z.Zhu, J.Zhang, F.Huang, H.Yan, *Chem. Rev.* **2018**, *118*, 3447.

[62] Y.Yang Michael, W.Chen, L.Dou, W. H.Chang, H. S.Duan, B.Bob, G.Li, Y.Yang, *Nat. Photonics* **2015**, *9*, 190.

[63] S. M.Sze, K. K.Ng, *Physics of Semiconductor Devices: Third Edition*, **2006**.

[64] U.Aswathanarayana, *Green Energy Technol. Econ. Policy* **2010**, 21.

[65] W.Shockley, *Proceedings of the I.R.E,* **1952**, 1365.

[66] A.Tsumura, H.Koezuka, T.Ando, *Appl. Phys. Lett.* **1986**, *49*, 1210.

[67] S. C. B.Mannsfeld, B. C. K.Tee, R. M.Stoltenberg, C. V. H. H.Chen, S.Barman, B. V. O.Muir, A. N.Sokolov, C.Reese, Z.Bao, *Nat. Mater.* **2010**, *9*, 859.

[68] R. S.Dudhe, J.Sinha, A.Kumar, V. R.Rao, *Sensors Actuators, B Chem.* **2010**, *148*, 158.

[69] K. K.Tsung, S. K.So, *J. Appl. Phys.* **2009**, *106*, 083710.

[70] C. H.Cheung, K. C.Kwok, S. C.Tse, S. K.So, *J. Appl. Phys.* **2008**, *103* ,*093705*

[71] C. Y. H.Chan, K. K.Tsung, W. H.Choi, S. K.So, *Org. Electron. physics, Mater. Appl.* **2013**, *14*, 1351.

[72] W.-Y.Sit, S. H.Cheung, C. Y. H.Chan, K. K.Tsung, S. W.Tsang, S. K.So, *Adv. Electron. Mater.* **2016**, *2*, 1500273.

[73] D.Natali, M.Sampietro, *Nucl. Instruments Methods Phys. Res. Sect. A Accel. Spectrometers, Detect. Assoc. Equip.* **2003**, *512*, 419.

[74] Y. Y.Noh, D. Y.Kim, K.Yase, *J. Appl. Phys.* **2005**, *98*, DOI 10.1063/1.2061892.

[75] J. Y.Park, H. M.Le, G. T.Kim, H.Park, Y. W.Park, I. N.Kang, D. H.Hwang, H. K.Shim, *Synth. Met.* **1996**, *79*, 177.

[76] S.Veprek, **2004**, *317*, 313.

[77] Y.Guo, C.Du, C. A.Di, J.Zheng, X.Sun, Y.Wen, L.Zhang, W.Wu, G.Yu, Y.Liu, *Appl. Phys. Lett.* **2009**, *94*, 114511.

[78] M. C.Hamilton, S.Martin, J.Kanicki, *IEEE Trans. Electron Devices* **2004**, *51*, 877.

[79] B.Lucas, T.Trigaud, C.Videlot-Ackermann, *Polym. Int.* **2012**, *61*, 374.

[80] K. S.Narayan, T. B.Singh, *Appl. Phys. Lett.* **1999**, *74*, 3456.

[81] W.Huang, Y. H.Lin, T. D.Anthopoulos, *ACS Appl. Mater. Interfaces* **2018**, *10*, 10202.

[82] X.Liu, E. K.Lee, D. Y.Kim, H.Yu, J. H.Oh, *ACS Appl. Mater. Interfaces* **2016**, *8*, 7291.

[83] W.Zhang, M. H.Chiu, C. H.Chen, W.Chen, L. J.Li, A. T. S.Wee, *ACS Nano* **2014**, *8*, 8653.

[84] L.Caranzi, G.Pace, M.Sassi, L.Beverina, M.Caironi, *ACS Appl. Mater. Interfaces* **2017**, *9*, 28785.

[85] W.Choi, M. Y.Cho, A.Konar, J. H.Lee, G. B.Cha, S. C.Hong, S.Kim, J.Kim, D.Jena, J.Joo, S.Kim, *Adv. Mater.* **2012**, *24*, 5832.

[86] X.Gong, M.Tong, Y.Xia, W.Cai, J. S.Moon, Y.Cao, G.Yu, C. L.Shieh, B.Nilsson, A. J.Heeger, *Science (80).* **2009**, *325*, 1665.

Chapter 3 Experimental Details

3.1 Substrate Preparation

For photovoltaic devices, pre-patterned indium tin oxide (ITO) (2cm × 2 cm) with a sheet resistance of 15Ω/□ were purchased from Kintec Hong Kong. Figure 3.1 shows the layout of the pre-patterned ITO substrate. For thin-film transistors or photodetector devices, plain glass substrates were used. These substrates were first rubbed with cotton swaps with acetone to remove impurities such as glue and dust. ITO substrates were then immersed in propan-2-ol and acetone for 20 minutes each in an ultrasonic bath to further remove impurities. Ultraviolet-ozone treatment of 20 minutes was then performed on the substrates to remove carbon contamination. In addition, such treatment will also increase the work function of ITO to about -4.7eV for better hole injection efficiency. Illuminating UV-ozone on the substrates not only changes the composition of indium, tin, and oxygen in ITO, the surface energy will also change. Therefore, the wetting of the solution can be improved.[1] After the above cleaning procedures, ITO or glass substrates are ready for film deposition.

Experiment	Sample Structure	Number of devices	Device Area
Photovoltaic Devices	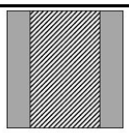	8	5mm²
Thin film transistors or phototransistors	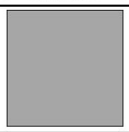	50	W=1000μm L=30-100μm

Figure 3.1 Layout of pre-patterned indium tin oxide (ITO) substrate and glass substrate. The shaded and grey area are ITO and glass, respectively

3.2 Solution Preparation and Spin-coating

Organic materials are dissolved in organic solvents prior to spin-coating. Common solvents such as chlorobenzene (CB), dichlorobenzene (DCB), tetrahydrofuran (THF), dimethylformamide (DMF) are often used. The choice of organic solvent for spin-coating depends on its properties such as boiling point, polarity, and the solubility of the solute. Figure 3.2 shows the preparation procedure for organic materials. The organic material is first dissolved in organic solvent. The concentration of the solution typically ranging from 0.5mg/mL to 50mg/mL. Higher concentration may cause saturation to the solution, which may cause inhomogeneous film formation or poor wetting issues. Depending on the material, heating the solution may also help the solubility. The undissolved impurity may exist in the solution. Therefore, a polyvinylidene fluoride (PVDF) or polytetrafluoroethylene (PTFE) filter of pore size 0.45μm was used to filter away solid impurities. The filtered solution is then put on a hotplate to ensure high solubility for spin-coating.

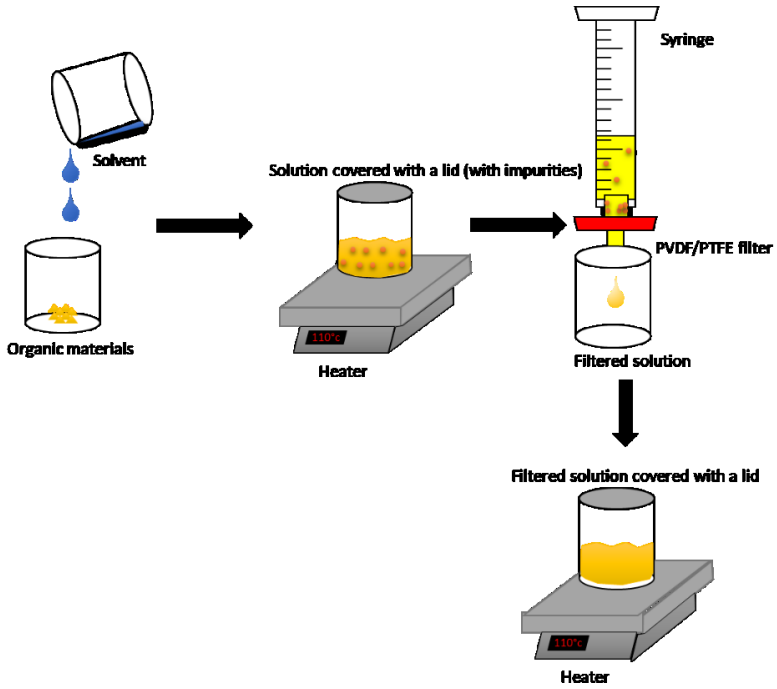

Figure 3.2 Schematic diagram of the procedure for preparing a solution for spin-coating.

After preparing the substrates from UV-ozone treatment, the substrates are ready to perform spin-coating. There are two methods for spin-coating: 1) Static spin-coating and 2) Dynamic spin-coating: For static spin-coating, the spin-coater chuck was kept stationary when the solution is dropped onto the substrate. Approximately 100µL to 150µL of solution is sufficient for a 2cm×2cm substrate. The spin-coater chuck then starts to spin at 800 revolutions per minute (rpm) to 2000 rpm for 60 seconds. Higher spin speed will yield a thinner film. For dynamic spin-coating, the chuck starts to spin at the desired spin-coating speed, the solution is then dropped onto the substrate while the substrate is rotating. With dynamic spin-coating, the amount of solution required can be reduced to 50uL to 100uL, which helps to reduce the consumption of organic materials. After the spin-coating process, the substrates

were then placed on the hotplate for thermal annealing to evaporate the excess organic solvent, leaving an organic thin film on the substrate. According to Hall et al[2], spin-coating consists of two different stages. Firstly, once the solution is dropped on the substrate, the film thinning process is purely due to radial outflow, which means the excess solution is spun away from the substrate. In this stage, solvent evaporation is negligible, and the concentration of the solution is assumed to be constant. Secondly, the thin film will enter the solvent evaporation stage where the thickness of the film is further reduced. It is worth noting that the angular acceleration of the spin coating chuck plays a critical role to form a homogeneous film. For instance, CYTOP, a high dielectric constant polymer which is used for dielectric layer in organic thin film transistors, has high viscosity. CYTOP has dynamic viscosity in the order of ~10^2m Pa·s compared to 1mPa·s for water. If CYTOP was spun at a high angular acceleration, it has insufficient time to spread out to the whole film and therefore inhomogeneous film was formed.

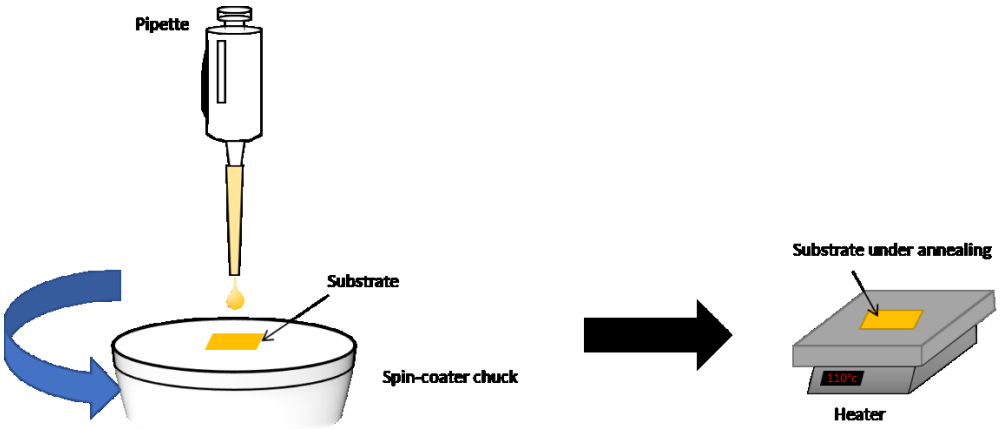

Figure 3.3 Schematic diagram for spin-coating and thermal annealing process.

Table 3.1 shows the spin-coating condition for the materials that we have used. For CuSCN:$PC_{70}BM$ mixed layer, the substrate should spin-coated when the substrate is at around 100°C. The substrate temperature will affect the device performance of CuSCN:$PC_{70}BM$. The details of such behavior will be discussed in Chapter 5. For CYTOP, which was dissolved in perfluorotributylamine (PFTBA), has high viscosity. It is advised to set the angular acceleration to be the lowest to help CYTOP solution to slowly spread out to the whole substrate at the beginning of the spin-coating process. This would help the film to be more homogeneous and reduce the number of gas bubbles inside the film. Such bubbles inside CYTOP may cause a low breakdown voltage or high leakage current of the transistors. In chapter 5, we have use aluminium and silver nanoparticles. These particles were synthesized by Dr. George Kakavelakis from Technological Educational Institute of Crete.

Material	Concentration [mg/ml]	Solvent	Dissolving Temperature [°C]	Spin-speed [rpm]	Duration [seconds]	Thickness [nm]	Annealing Temperature [°C]	Remark
$PC_{70}BM$	30	CB	75°C	2000	60	50	100	
CYTOP		PFTBA	Room Temperature	2000	120	110	100	Lowest angular acceleration

Table 3.1 Spin-coating conditions for the materials that were used in this thesis. CuSCN was dissolved in diethyl sulfide (DES), $PC_{70}BM$ was dissolved in chlorobenzene (CB), and CYTOP was dissolved in perfluorotributyleamine (PFTBA).

3.3 Thermal Evaporation

Apart from spin-coating, thermal evaporation is another technique that is used to deposit thin film. Thermal evaporation is widely used because some organic

materials may not have decent solubility in the organic solvent, for instance, pentacene. Thermal evaporation also enables patterning electrodes as it is difficult to spin coat a pattern on substrates. In addition, substrate temperature, source temperature, and deposition rate can be controlled, which could alter the nanostructure of the deposited material for optimizing device performance.[3,4] Figure 3.4 shows the schematic diagram of a thermal evaporator. Organic materials or metals are first placed inside the organic source or metal source respectively. The chamber is then closed to the pump down stage. Nitrogen gas inside the chamber will first evacuated by mechanical pump. The pressure will decrease to 10^{-3} mbar (low vacuum) in this stage. After reaching low vacuum, the turbopump will start to further evacuate the gas inside the chamber to reach 5×10^{-6} mbar (high vacuum). In such pressure, the boiling or sublimation point of metal/organic materials will decrease such that they can be evaporated onto the substrates at a lower temperature than in atm. The metal source or organic source is then heated up to reach the boiling/sublimation point. Metal or organic vapor is now leaving the source and its deposition rate is monitored by a crystal sensor. The deposition rate is tuned to about 1Å/s to10 Å/s to ensure a smooth film. Such slow rate can prevent the metal atoms to penetrate the film. Before reaching the desired coating rate, a shutter is used to block the materials from the films. Once the rate become stable, the shutter is then opened, the substrate holder will rotate about its axis to ensure uniform film thickness. Table 3.2 shows the deposition rate and thickness that we have used in this thesis.

Material	Thickness [nm]	Deposition rate [Å/s]	Remark
BCP	10	0.2	
Gold	40	0.5-1	Source/Drain electrodes for transistors

Table 3.2 Thickness and deposition rate of different materials we used in thermal evaporation.

For photovoltaic devices, the electrode should be patterned on the substrate in order to have a well-defined device active area as shown in Figure 3.5. Figure 3.5a and Figure 3.5b show the substrate that is used for the photovoltaic device and its shadow mask respectively. After depositing photoactive material on the substrate by spin coating, the film will be fully covered by the organic material (Figure 3.5c). The patterned electrode is then thermally deposited through a shadow mask such that only certain area of the substrate is covered by metal. The active area of the substrate is defined by the overlapping area between ITO, photoactive material, and metal as shown in Figure 3.5d. The 3-dimensional illustration for an actual device is shown in Figure 3.5e. For transistor devices, Figure 3.6a and Figure 3.6b show the plain glass substrate and the diagram of shadow masks. The device configuration is illustrated in Figure 3.6c, where L and W denote the channel length and channel width respectively. Figure 3.6d shows the channel length distribution of the shadow mask. For all devices, channel width, W is the same (1000μm) and channel length, L has a

range from 30μm to 100μm.

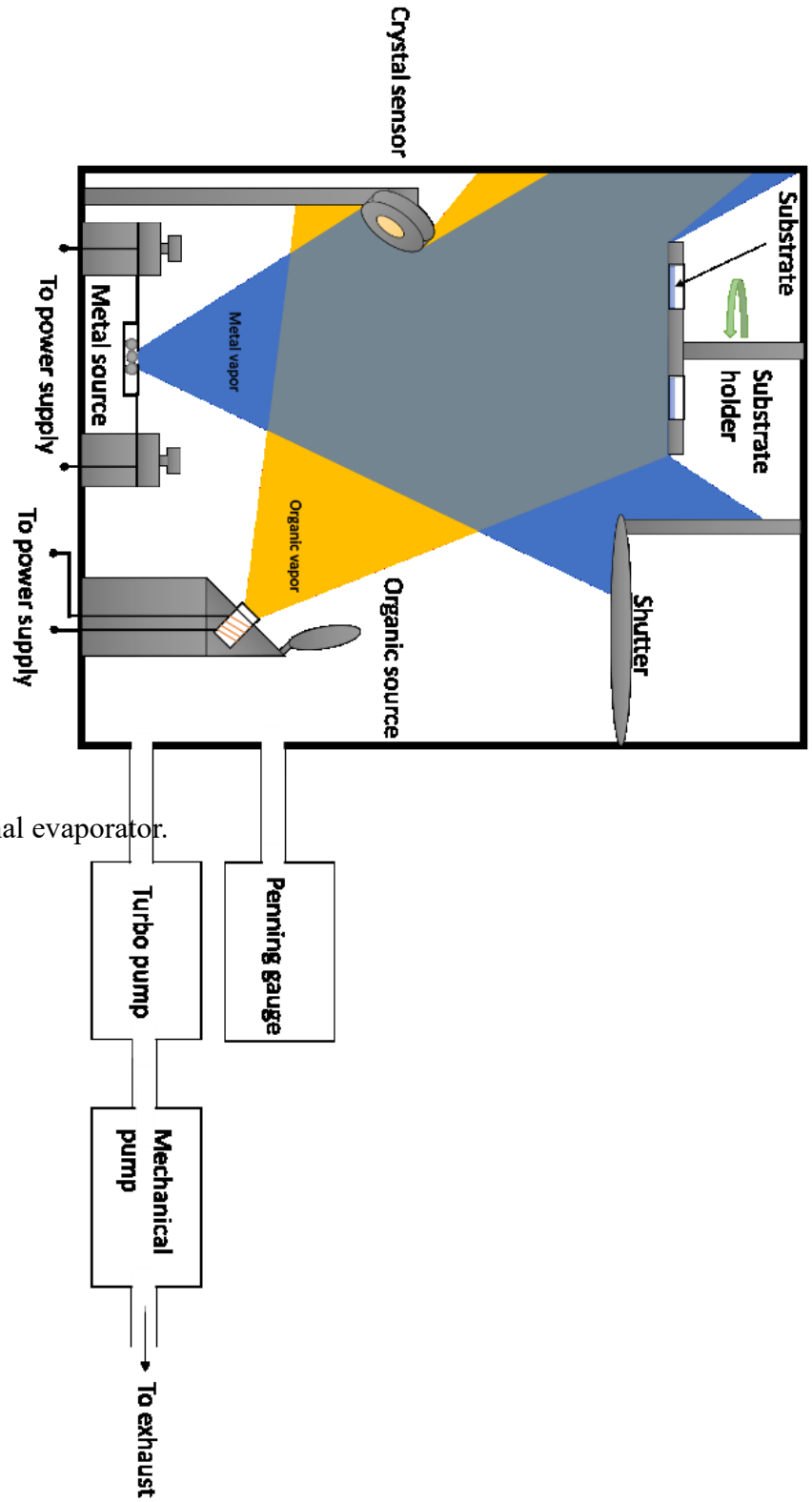

of metal and organic thermal evaporator.

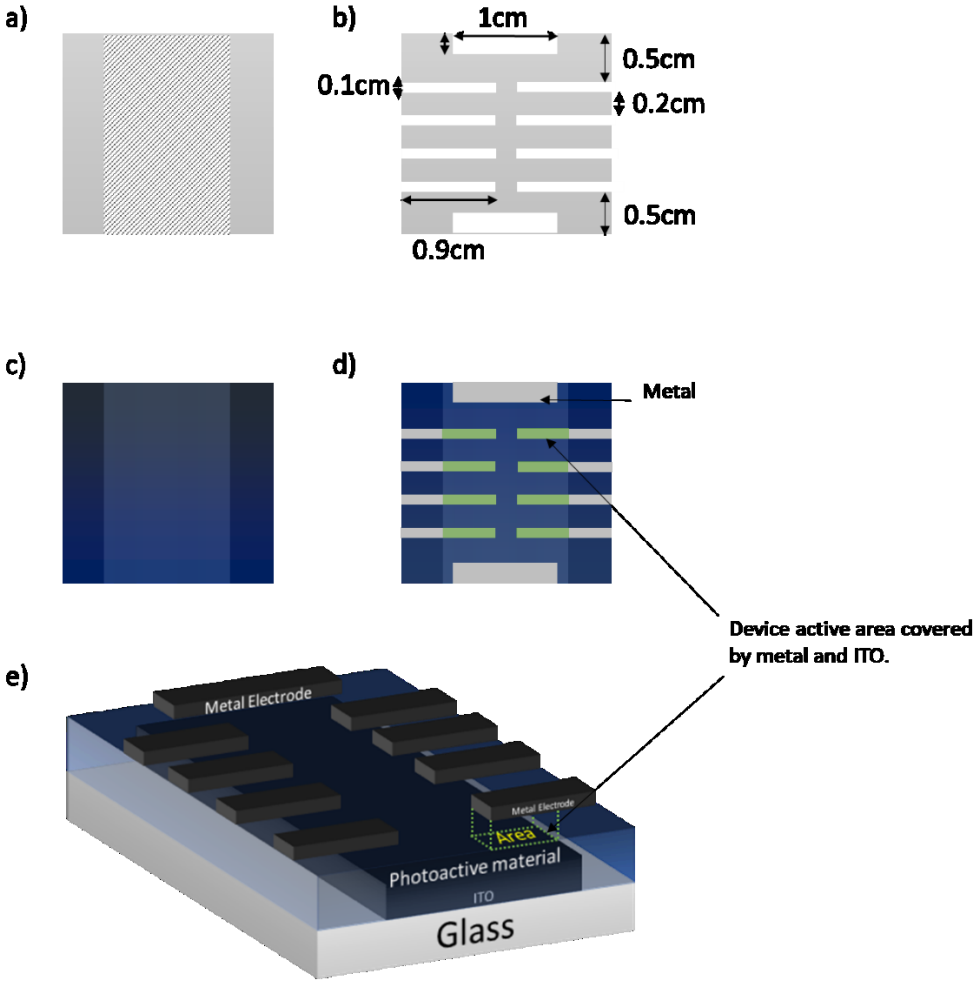

Figure 3.4 Top-view of a) substrate, b) shadow mask, c) substrate covered with photoactive material, and d) actual device covered with metal electrode where the green region denotes the active area of the device. e) The 3-dimensional structure of an actual device.

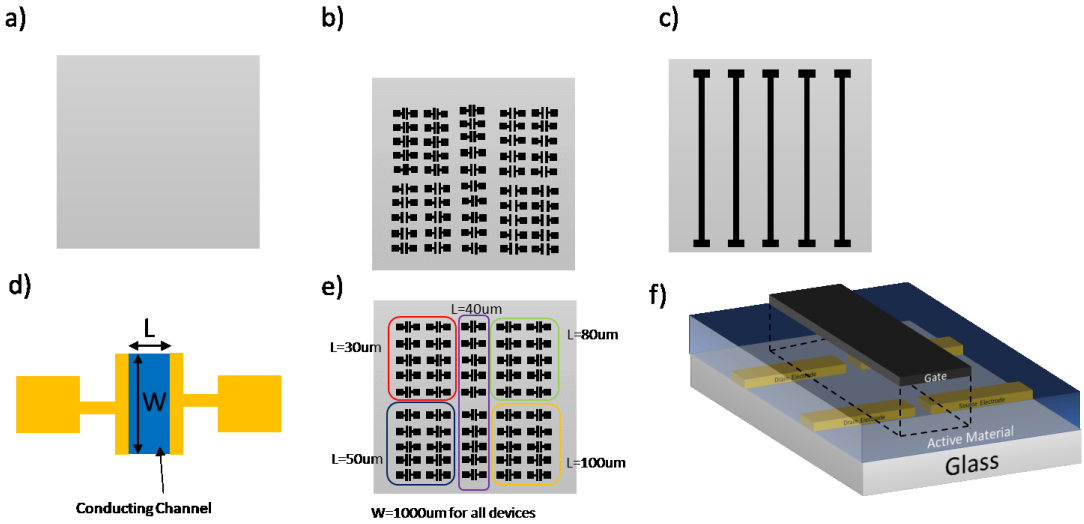

Figure 3.5 a) Plain glass substrate, b) shadow mask for source and drain electrodes, c) shadow mask for gate electrode, d) Structure of a transistor device. Metals are coated on orange region. Blue region is the conducting channel. W is the channel width, which is 1000µm for all devices and L is the channel length, and e) Different channel length on the shadow mask ranging from L=30µm to L=100µm. f) 2-D and 3-D diagram of the actual thin film transistor device.

3.4 Photovoltaic Device Characterization

The sample and sample holder are initially placed inside a nitrogen-filled glovebox to prevent device degradation due to oxygen and moisture exposure. Figure 3.7a and Figure 3.7b shows the diagram of the sample holder and the experimental setup for photovoltaic device characterization, respectively. The solar simulator is turned on and warm-up for 30 minutes to stabilize the light intensity. A photodiode is then used to calibrate the power at the measurement distance such that the light intensity is 100mW/cm^2. After calibrating the power from the solar simulator, Current density-Voltage characteristics (*J-V*) characteristics of the photovoltaic cell were measured by Keithley 2400 SourceMeter. In order to characterize the power conversion efficiency (*PCE*) of a photovoltaic device, short-circuit current (J_{sc}), open-circuit voltage (V_{oc}), and fill factor (*FF*) are measured by this setup. The *PCE* can be

calculated by the following relationship:

$$FF = \frac{V_{Max} J_{Max}}{V_{OC} J_{SC}} \tag{3.1}$$

,where V_{max} and J_{Max} are the maximum power output from the device as discussed in Chapter 2. The power conversion efficiency is then calculated by:

$$PCE = \frac{V_{Max} J_{Max}}{P_{in}} = \frac{FF \cdot V_{OC} \cdot J_{SC}}{P_{in}} \tag{3.2}.$$

After the measurement, the lamp is then turned off, but the system remains on to allow the lamp to cool down for at least 30 minutes before shutting down the system.

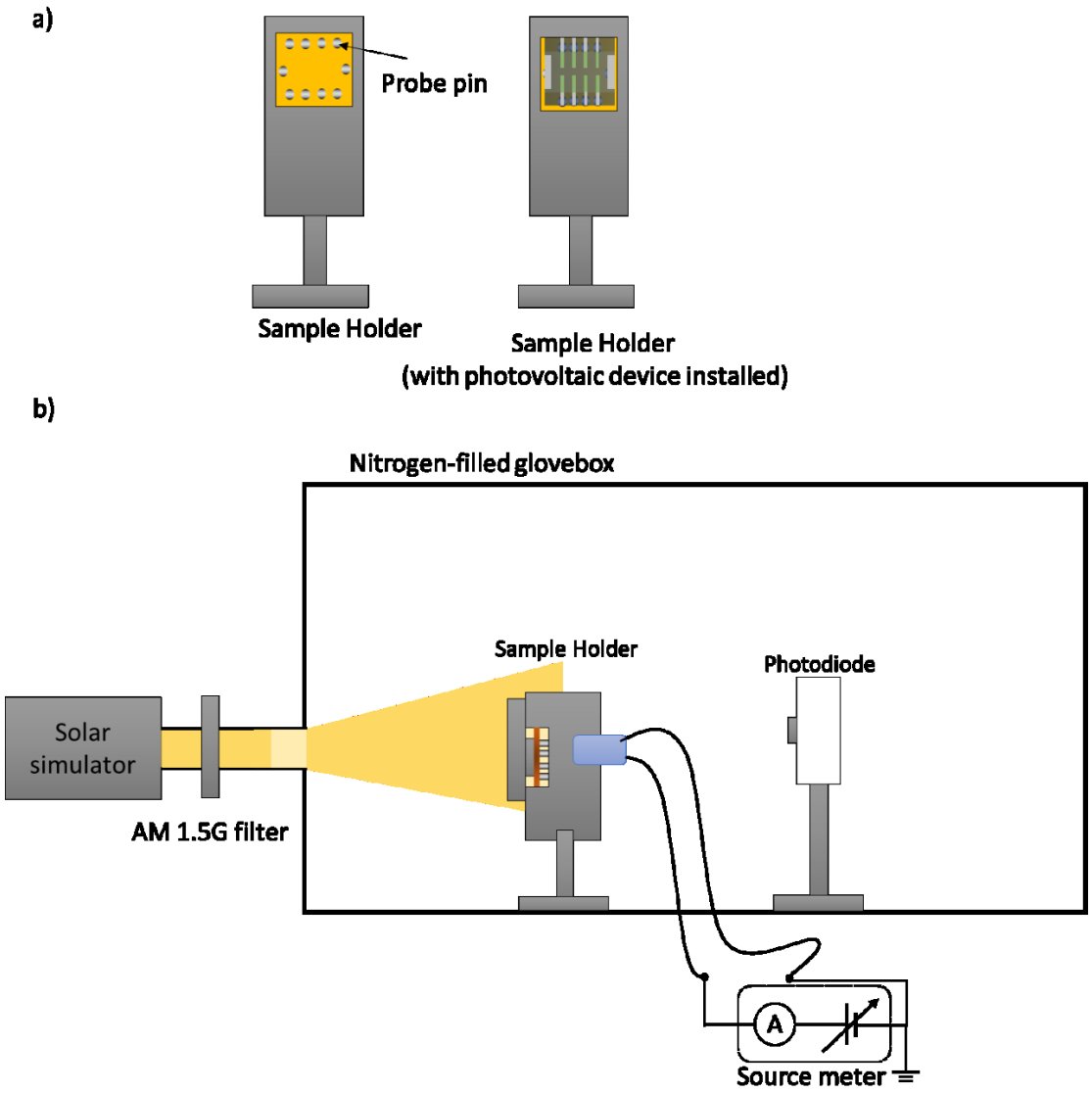

Figure 3.6a) Schematic diagram of the sample holder. b) Experimental setup for photovoltaic device characterization.

3.5 Transistor Characterization

Similar to photovoltaic devices, transistors and phototransistors are characterized inside a nitrogen-filled glovebox. Figure 3.8 shows the experimental setup for thin-film transistor measurement. The device is first placed firmly on a Teflon platform. Three different probe pins are connected from source, drain, and the gate electrode to the Agilent Source Meter. Since the dimension of these electrodes is relatively small,

a magnifying camera is used to help to align those pins to the electrode. The source meter is able to provide $\pm$ 200V to the device and measure the current through it. The transfer characteristics (Figure 3.9a) and output characteristics (Figure 3.9b) can be measured in this way. In transfer characteristics, both drain current and the gate current are measured. Drain current represents the electrical current passing from source electrode to drain electrode whilst gate current represents the electrical current going from source/drain current to the gate current. Ideally, the gate current should be minimized as the dielectric layer is insulating when the device is at ON state ($V_g > V_t$). However, due to device defects such as inhomogeneous dielectric layer or the active layer, the gate current may have the same order of magnitude to drain current and result in a poor device. A preferred device typically has drain to gate current ratio to be more than 10, that is:

$$\frac{I_{DS}}{I_{GS}} > 10 \qquad (3.3).$$

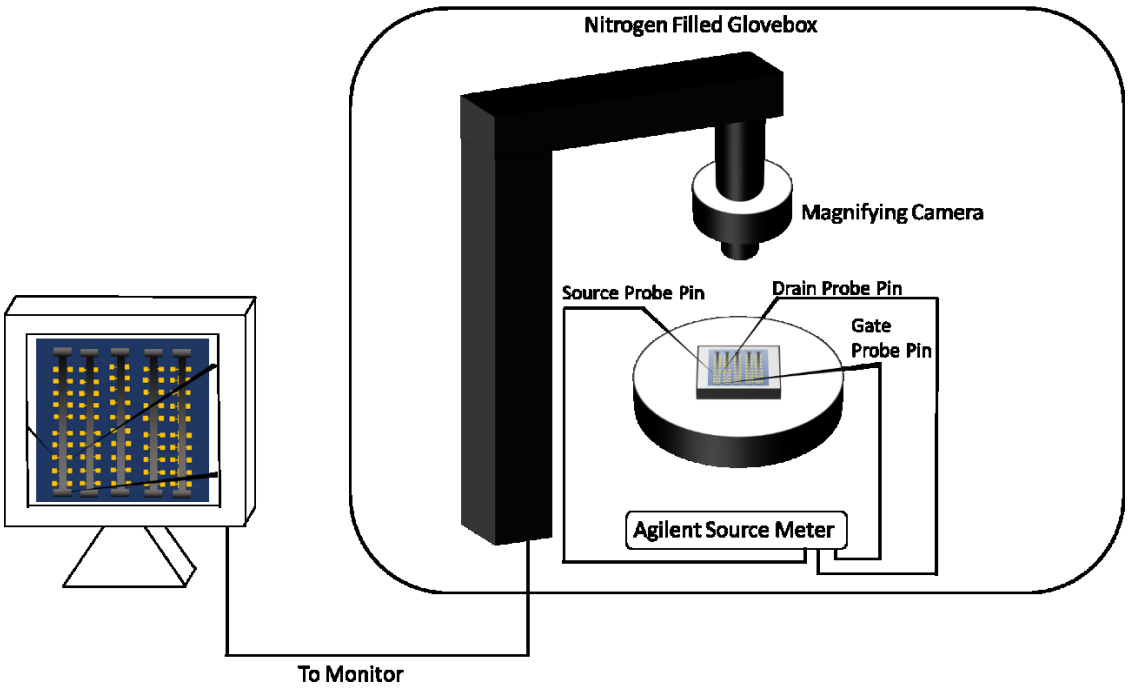

Figure 3.7 Experimental setup of thin film transistor characterization

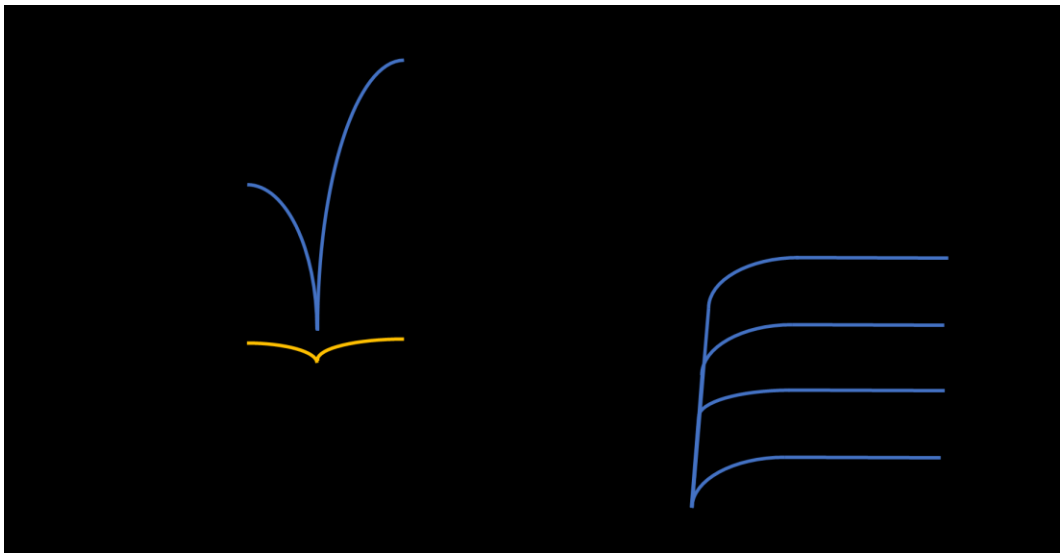

Figure 3.8 Typical transfer characteristics and output characteristics of the measured transistor

3.6 Phototransistor Characterization

The setup of the phototransistor is very similar to the thin film transistor. The device is placed in a hollow platform that allows light to be illuminated from the back of the device (Figure 3.10). LEDs with wavelengths of 480nm, 540nm, and 650nm were used in our analysis. Figure 3.11 shows the spectra of the LEDs. As photons will excite free carriers in the photoactive materials, those carriers contribute to the current conduction and thus photocurrent can be measured as shown in Figure 3.12. The measurement method is similar to ordinary transistors as shown in Section 3.5.

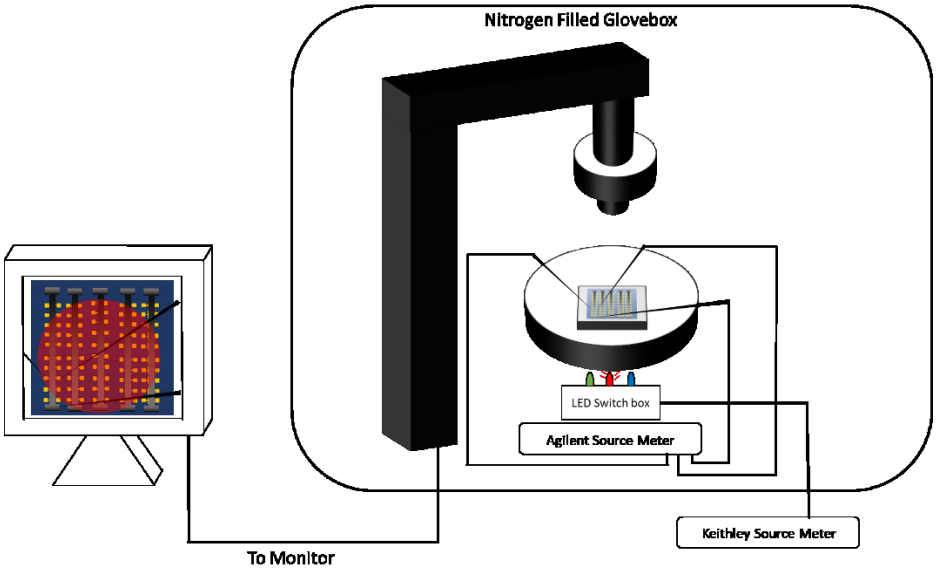

Figure 3.9 Experimental setup of phototransistor characterization with red LED is on.

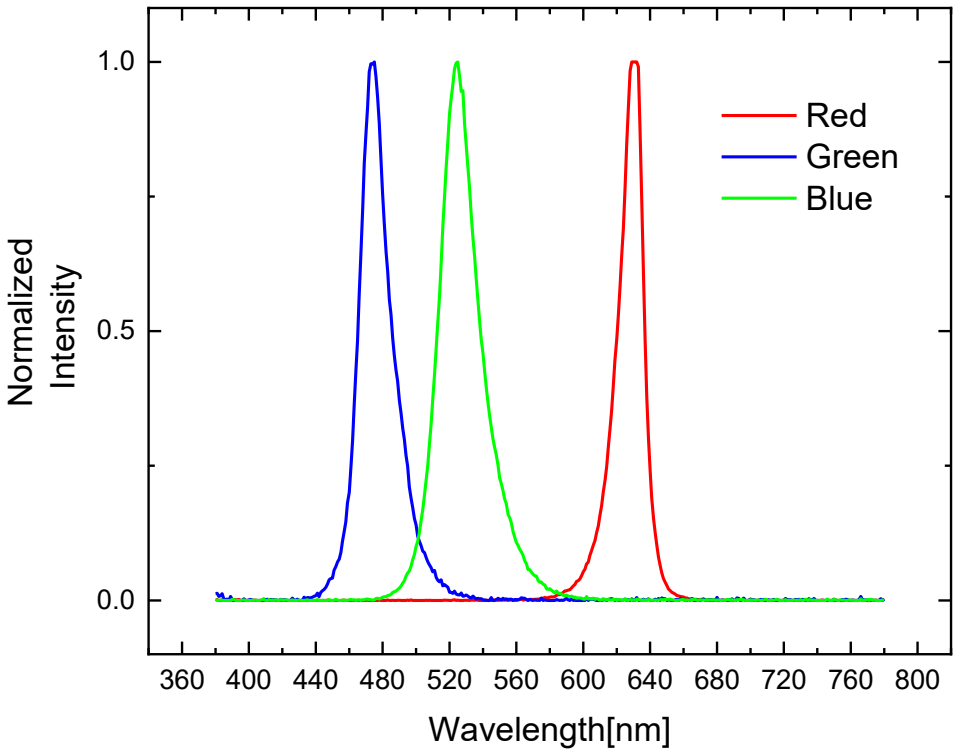

Figure 3.10 Emission spectra of LED lights of blue (λ=480nm), green (λ=540nm), and red (λ= 650nm).

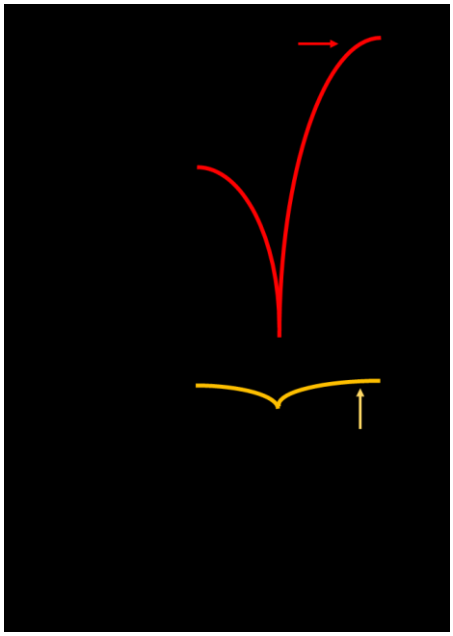

Figure 3.11 Transfer characteristics of a phototransistor with and without LEDs.

Reference

[1] K.Sugiyama, H.Ishii, Y.Ouchi, K.Seki, K.Sugiyama, H.Ishii, Y.Ouchi, J. Appl. Phys, 2000, **87,** 295

[2] D. B.Hall, P.Underhill, J. M.Torkelson, Chem. And Bio. Eng., 1998, 38, **2039**.

[3] K.Hong, M.Xie, R.Hu, H.Wu, Nanotechnology, 2018, **085604**,

[4] A.Umar, S. H.Kim, J. H.Kim, A.Al-hajry, Y.Bong, Journal of alloys and compounds. 2008, 463, **516**.

Chapter 4. High-Efficiency Fullerene Solar Cells Enabled by a Spontaneously Formed Mesostructured CuSCN-Nanowire Heterointerface

To date, most of the commercial solar cells are based on inorganic semiconductor with silicon being by far the most widely used material. This is because silicon offers high diffusion length and a significant absorption spectrum in the visible range. However, to manufacture high efficiency silicon based solar cell is still costly, as high purity silicon requires costly purification technology. Although other inorganic-based solar cells technologies exist (e.g. $CuInGaSe_2$ (CIGS), InGaN/GaN) the cost of manufacturing remains relatively high and the power conversion efficiency moderate.[1–3]

Organic solar cell represent one emerging solar cell technology that promises to offer a viable replacement to inorganic technologies as it provides numerous advantages: low-cost, mechanical flexibility, easy processing and compatibility with large area fabrication, and tunable bandgap for optimal light absorption spectra. However, organic materials tend to have low carrier mobility and poor stability due to chemical reactivity with various atmospheric oxidants.

Organic-inorganic hybrid solar cells have started to become popular in recent years. Combining the advantages of both organic and inorganic materials to improve the solar cell performance.[4] For instance, inorganic materials usually offer higher carrier mobility to improve the carrier transport inside the material. Inorganic materials are more stable, which helps the stability and lifetime issue for organic devices. Organic materials enable researchers to adjust the optical bandgap for better light absorption spectrum. One of most successful organic-inorganic hybrid solar cell to date is perovskite solar cell. It has high carrier mobility and high optical absorption in the visible

range. The recent researched showed that perovskite solar cell could achieve 25.2% power conversion efficiency (PCE), compared to the highest PCE achieved by organic solar cell to date, which is 16.5%.[5]

Here, we have used a similar approach to fabricate organic-inorganic solar cell using methanofullerenes and CuSCN in both planar and mixed active layer structures. We have found that CuSCN nanowires form spontaneously in mixtures of methanofullerenes with CuSCN, leading to improved solar cell performance.

4.1 Copper (I) Thiocyanate

Copper (I) thiocyanate (CuSCN) is a metal pseudohalide that exhibits excellent electrical and optical properties for use in various semiconductor applications. Figure 4.1a shows the powder form of CuSCN with the chemical structure of CuSCN shown in Figure 4.1b. CuSCN exhibits two dominant polymorphs, both α-CuSCN and β-CuSCN, and it has been previously found that both α-CuSCN and β-CuSCN (shown in Figure 4.1b) exist in thin films prepared from n-alkyl sulfide solvents. The two phases of CuSCN differ by the S-C-N bond angle and the C-N bond length, with the differences in crystal structure summarized in Table 4.1. In practice, β-CuSCN is the dominant polymorph found in solution processed thin film, with most electrical and optical properties stemming this type. [6] I will thus focus my descriptions of CuSCN on this phase from here onwards.

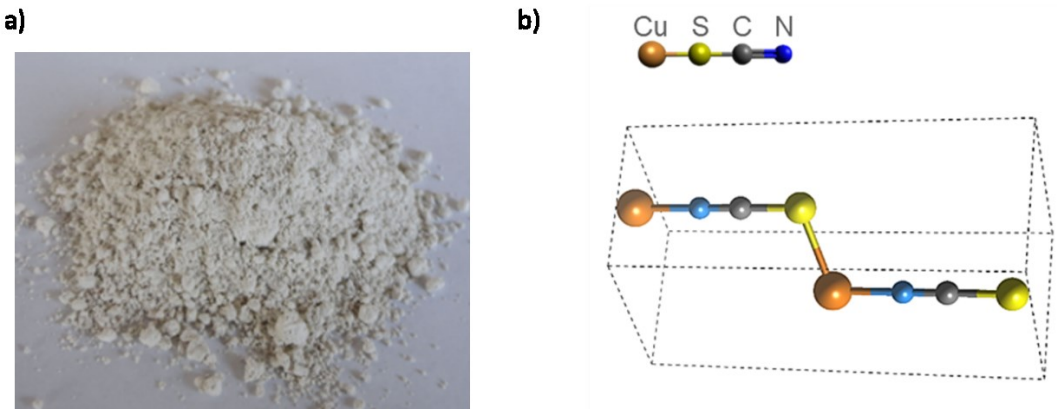

Figure 4.1 a) CuSCN powder b) chemical formula of CuSCN and 3D structure of β-CuSCN.

CuSCN is also an intrinsic p-type semiconductor which transports holes efficiently, a property which stems from a strong character of hybridized Cu 3d and S 3p states and cyanide antibonding near the band edges, which leads to a high dispersion near the top of the valence band. It has thus been found that field-effect hole mobility of CuSCN is on the order of 0.01-0.1 cm^2/Vs measured in top-gate bottom-contact (TGBC) TFT configuration.[6] However, this mobility value depends on the processing condition and is difficult to reproduce. For instance, in our analysis, which will be presented in Chapter 6, the hole mobility in CuSCN is found to be 0.0001 – 0.001 cm^2/Vs if CYTOP was used as the gate dielectric layer and TGBC contact configuration was used.

	α-CuSCN	β-CuSCN
SCN bond angle	177°	160°
Crystal Structure	Orthorhomic	Hexagonal/Rhombohedral

Table 4.1 Structural properties of α-CuSCN and β-CuSCN.

In terms of its optical properties, CuSCN has low absorption coefficient over the visible range (Figure 4.2). As a result, CuSCN is highly transparent and thus a promising interlayer for photovoltaic or other optoelectronic devices as it exhibits small absorption.[7] To this end, density functional theory (DFT) calculations show that CuSCN has a theoretical indirect bandgap of 3.5 eV, while experimentally, Pattanasattayavong *et al* determined a direct bandgap of 3.87 eV and indirect bandgap of 3.49 eV using UV-Vis spectroscopy.[8] Further, the VB of CuSCN has been shown to lie around -5.5 eV, making it compatible with hole extraction and injection with many polymers commonly used in organic solar cells, with the CB around -2 eV.

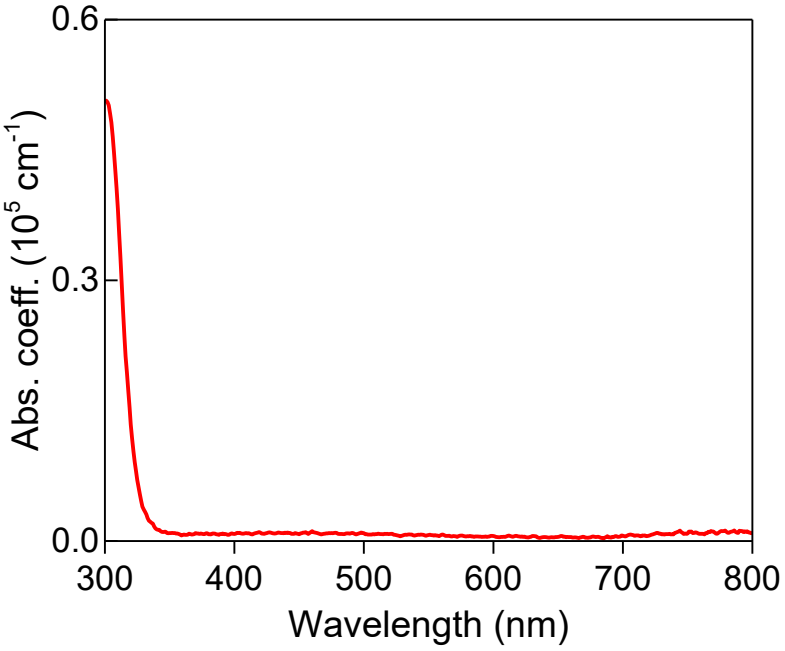

Figure 4.2 Absorption coefficient of CuSCN

The solution processing method of CuSCN is relatively simple. Typically, CuSCN is dissolved in diethyl sulphide (DES)[7,9,10] or dipropyl sulphide (DPS)[11–13]. However, the solubility of CuSCN in DPS is low, such that the thickness CuSCN films

deposited from this solvent is limited. A thin CuSCN film may cause poor coverage of the layer beneath it and therefore leakage current problem may arise, making DES (in which CuSCN has a maximum solubility of around 40 mg/ml) the preferred solvent for fabricating CuSCN thin films. For example, when using DES as the solvent during spin-casting, a CuSCN concentration of 20-35mg/mL will lead to approximately 55-95nm thick films at a spin speed of 2500 rpm.

Because of its favorable properties for use as a hole transport layer (HTL) in solar cells, CuSCN is often used to compare or replace its common counterpart in this application, PEDOT:PSS, a conductive polymer with good hole mobility and easy solution processability and a similar VB to CuSCN. However, due to its acidic property, PEDOT:PSS has been shown to etch away organic layers beneath or above it.[14] This effect may not only cause stability and lifetime problem, but may also lead to the increase of leakage current of the device. This contrasts to CuSCN, where the high valence band energy helps to block electrons to reduce leakage current and has been shown to have increased short circuit current. [7,15,16] CuSCN also shows improved visible transmittance compared to PEDOT:PSS.[6]

Due to above properties, CuSCN has been shown to have vast number of potential applications when it is employed as the hole transporting layer. For example, CuSCN has been used in dye-sensitized solar cell (DSSC) to fill in the porous TiO_2 , which increased the surface contact area and therefore the power conversion efficiency.[17,18] Also, recently CuSCN was also used as the HTL in a perovskite solar cell that achieved more than 20% power conversion efficiency.[7,15,16,19,20] Apart from the results above, CuSCN was also used to make thin film transistors (TFTs),[8,21,22] organic photovoltaic devices (OPVs),[7,9,16] photodetectors,[23–25] and organic light

emitting diodes (OLEDs).[26–30]

4.2 Buckminsterfullerene and its derivatives

Buckminsterfullerene (C_{60}) (Figure 4.3a) is a carbon-based molecule. Consisting of 60 carbon atoms, each carbon is bonded with three adjacent carbon atoms, with two of them singly bonded and one of them doubly bonded. The double bond in the carbon atom allows the conjugation of π electrons, which enables electrical conduction in C_{60}, with a measured electron mobility of C_{60} of 0.25-5 cm^2/Vs.[31] This mobility value is relatively high compared to other organic materials. A related molecule is C_{70} (Figure 4.3b), another molecule in the family of fullerene as shown in Figure 4.3b, with 70 instead of 60 carbon atoms in the cage. It has lower mobility of 0.002 cm^2/Vs.[32] Both C_{60} and C_{70} were widely used in the early stages of organic photovoltaic device research and they require thermal vapor deposition for planar heterojunction solar cell, as solution processed C_{60} or C_{70} film has low solubility to make thick film. As discussed before, solution processing is a cost effective and convenient deposition method for large area fabrication of electronic devices. Recently, it has been found that C_{60} and C_{70} become more soluble when they are mixed together to a certain ratio.[33,34]

The other approach to make C_{60} or C_{70} become solution processible is to alter the molecules chemically. By adding side chain to C_{60} and C_{70}, phenyl-C61-butyric acid methyl ester ($PC_{60}BM$) (Figure 4.3c) and [6,6]-phenyl C71 butyric acid methyl ester ($PC_{70}BM$) (Figure 4.3d) started to become popular from 2003 as a replacement of C_{60}.[35] $PC_{60}BM$ and $PC_{70}BM$ are both asymmetric compared to C_{60} and C_{70}, which enables the lowest-energy transition and therefore increases the light absorption and therefore more sunlight can be harvested. Secondly, the branched chain of $PC_{60}BM$

and $PC_{70}BM$ helps them to have higher solubility, which facilitated the development of solution processed large area photovoltaic devices. [35,36]

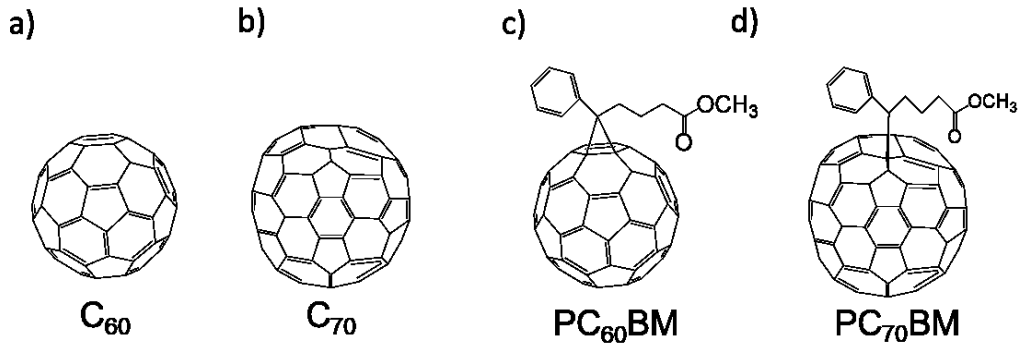

Figure 4.3 Chemical structure of a) C_{60} , b) C_{70}, c) $PC_{60}BM$, and d) $PC_{70}BM$.

The LUMO and HOMO energy of $PC_{60}BM$ and $PC_{70}BM$ are shown in Figure 4.4. It is worth noting that the reported HOMO and LUMO of the fullerenes and their derivatives may vary from different groups obtained by different methods. Figure 4.5 shows the UV-vis optical absorption spectrum for both methanofullerenes. Both $PC_{60}BM$ and $PC_{70}BM$ are absorptive in the visible range and $PC_{70}BM$ has a significantly higher absorption coefficient than $PC_{60}BM$.

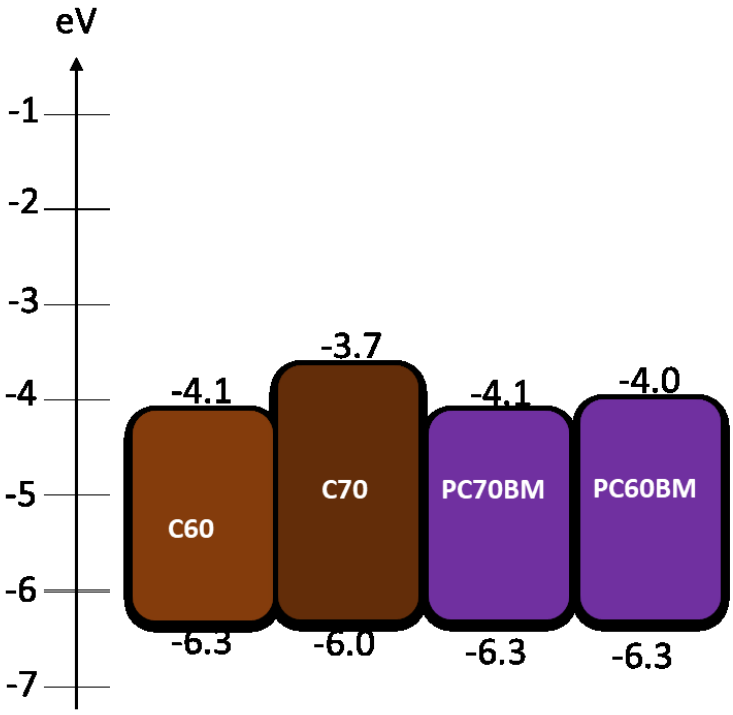

Figure 4.4 Energetic diagram of fullerene and its derivatives.

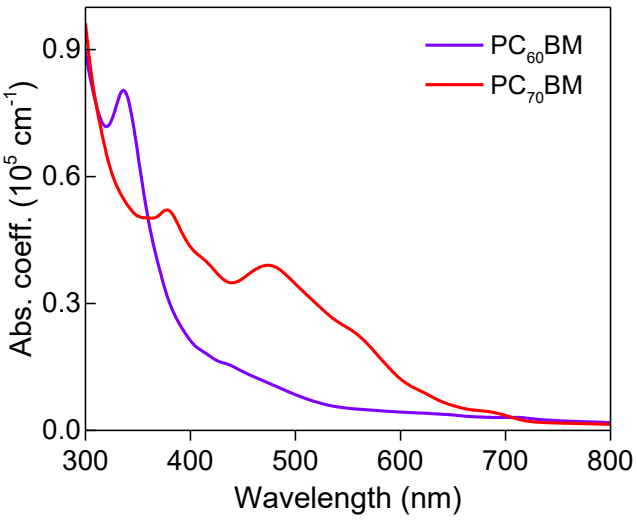

Figure 4.5 Absorption coefficient of $PC_{60}BM$ and $PC_{70}BM$. The films were deposited on quartz.

In order to understand the electrical properties of the fullerenes, we fabricated top-gate, bottom contact (TG-BC) thin film transistors devices of $PC_{60}BM$ and $PC_{70}BM$

using CYTOP as the gate dielectric layer. The channel length and width are 30 μm and 1000 μm, respectively. Figure 4.6 shows the transfer characteristics for $PC_{60}BM$ and $PC_{70}BM$ and Table 4.2 shows the extracted parameters from the results. Both $PC_{60}BM$ and $PC_{70}BM$ exhibit good ambipolar transport, with electron mobilities of 4×10^{-1} and 1.8×10^{-1} cm^2/Vs, respectively, and hole mobilities around half of those values, respectively. Comparing, these carrier mobilities to values from other studies (Table 4.2), I note that these are amongst the highest values found for these materials, whilst also noting that the carrier mobility appears to depend heavily on the TFT architecture, and the dielectric used. For instance, a hole mobility of $2\times10^{-5}cm^2/Vs$ of $PC_{70}BM$ was measured when bottom-gate bottom-contact configuration and dielectric layer of SU8 was used while in this work we measured a value of 9×10^{-2} cm^2/Vs.[9][37][38][39][40] Finally, I note that very few organic materials have been reported that both absorb visible light and processes such good ambipolar transport, which makes these methanofullerenes an interesting proposition for use in single material organic photovoltaic devices.

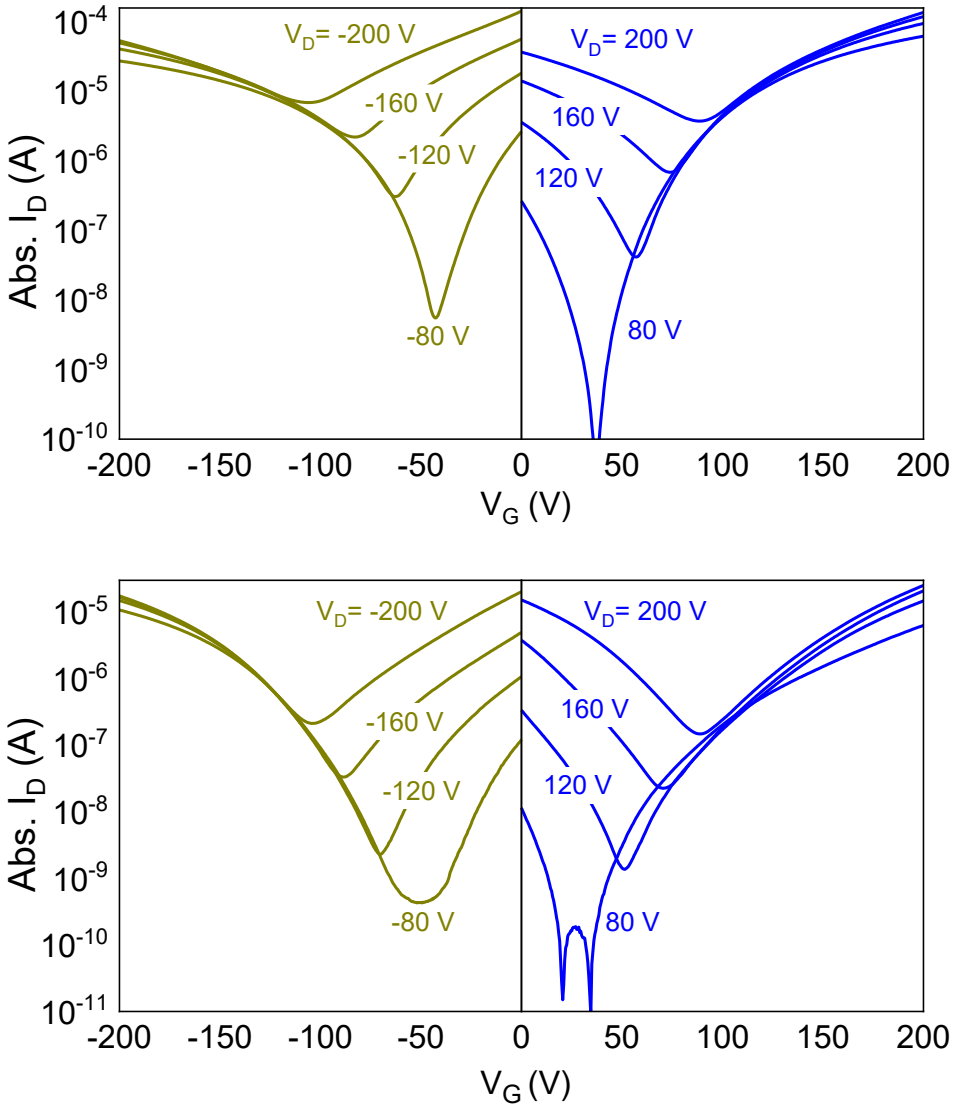

Figure 4.6 Transfer characteristics of a) $PC_{60}BM$ and b) $PC_{70}BM$. Top-gate bottom contact configuration was used. CYTOP was employed to be the gate dielectric layer. The source and drain voltage were scanned from -200 V to -80 V (p-type) and from +80V, and +200V (n-type). The channel lengths and widths are 30 μm and 1 mm respectively. Device structure is shown in the inset of the top panel.

Material	Carrier	Carrier mobility	Measurement Method	Configuration	Dielectric/SAM	Ref.
$PC_{60}BM$	e	$2x10^{-1}$	FET	BG-TC	BCB	[9]
	e	$4.2x10^{-1}$	FET	TG-BC	CYTOP	This work
	h	$8x10^{-3}$	FET	BG-BC	SiO_2/HMDS	[37]
	h	$1.8x10^{-1}$	FET	TG-BC	CYTOP	This work
$PC_{70}BM$	e	$1.2x10^{-1}$	FET	TG-BC	CYTOP	This work
	e	$1x10^{-2}$	FET	BG-TC	SiO2/HMDS	[38]
	e	$1x10^{-3}$	SCLC	N/A	N/A	[39]
	h	$2x10^{-5}$	FET	BG-BC	SU8	[40]
	h	$9x10^{-2}$	FET	TG-BC	CYTOP	This work

Table 4.2 Summary table of the carrier mobility values for $PC_{60}BM$ and $PC_{70}BM$ from this work and other reported literature.

4.3 Planar PCBM based photovoltaic device

Having confirmed the potential suitability of $PC_{60}BM$ and $PC_{70}BM$ in terms of their optical and electric properties for use in a single-material solar cell, I thus attempted to fabricate a working device. It has previously been shown that using PEDOT:PSS as the HTL in $PC_{70}BM$ single junction solar cells results in only a low photocurrent,[41] probably due to the poor electron blocking capabilities of PEDOT:PSS, which results in high recombination rates at the contacts. Since CuSCN has the necessarily high CB for electron blocking, I decided to attempt to incorporate CuSCN into such a device. Figure 4.7a thus shows the device structure and Figure 4.7b shows the energy diagram of the materials that was used in the photovoltaic cell incorporating CuSCN and fullerenes. The use of PEDOT:PSS/CuSCN as a combination in the early stage development is because PEDOT:PSS was used to planarize the surface roughness of indium tin oxide (ITO). On the cathode side, 2,9-dimethyl-4,7-diphenyl-1,10-phenanthroline (BCP) was used as the hole blocking layer, as opposed to the commonly used Ca, because of its low HOMO value in order to reduce recombination at the cathode. The chemical structure of PEDOT:PSS and

BCP are shown in Figure 4.8.

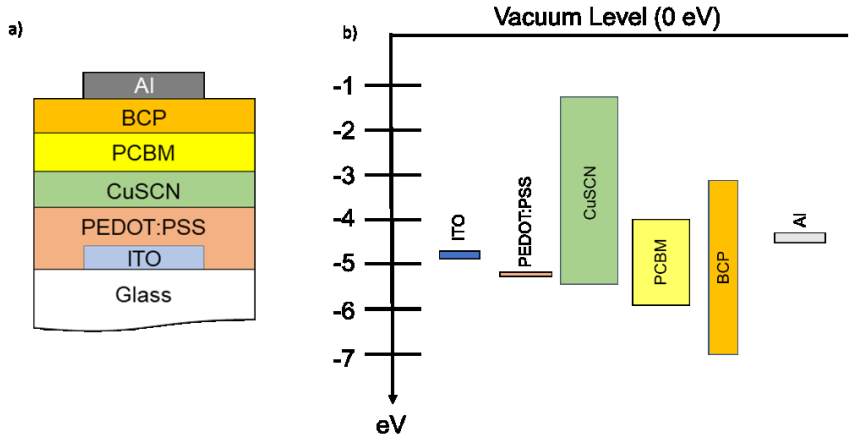

Figure 4.7 a) Device structure of single material solar cell using PCBM as the photoactive layer. b) Energy diagram of the material we used in the PCBM only photovoltaic device.

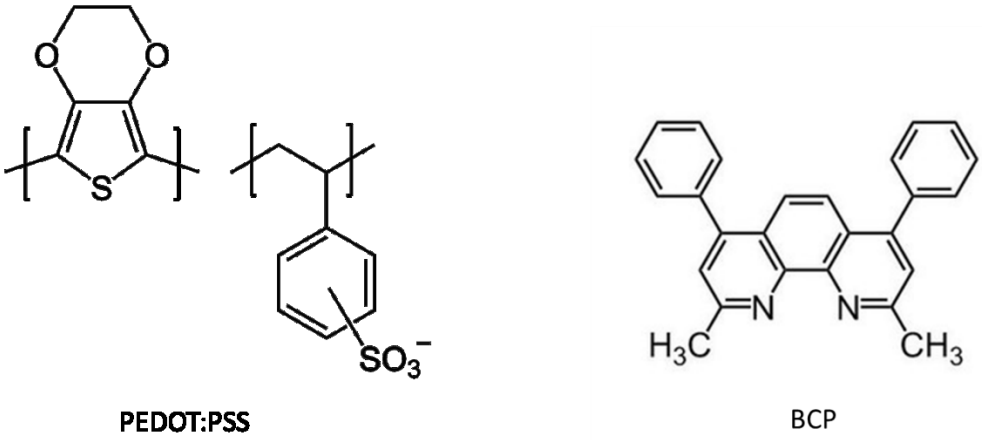

Figure 4.8 Chemical structure of PEDOT:PSS and BCP.

Figure 4.9 shows the device performance of planar $PC_{60}BM$ and $PC_{70}BM$ and Table 4.3 summarizes the device performance. It shows that the devices are capable to deliver short-circuit current of 1.4 mA/cm^2 and 2.3 mA/cm^2 in $PC_{60}BM$ and

$PC_{70}BM$ respectively. Although this value of J_{sc} is rather low compared to the most efficient bulk-heterojunction solar cells currently under research, it is significantly higher than the results without CuSCN (Figure 4.10) and is still promising because of the simple device structure employed, Ideally, the energetics of $PC_{60}BM$ and CuSCN suggest that the $PC_{60}BM$/CuSCN planar device could deliver up to 1V of open circuit voltage. The measured value of 0.55 V suggests there is a huge loss in V_{oc}, which could due to severe recombination, which led to a low J_{sc} of 1.4mA/cm^2. Also, this device suffers from high series resistance, suggesting further optimization of the PCBM layer, or change in device structure is required. On the other hand, the performance for $PC_{70}BM$ device is significantly better. High open circuit voltage of 0.9V is measured, which is closer to the theoretical V_{oc} from the energetic diagrams, resulting in a promising PCE 1.1%.

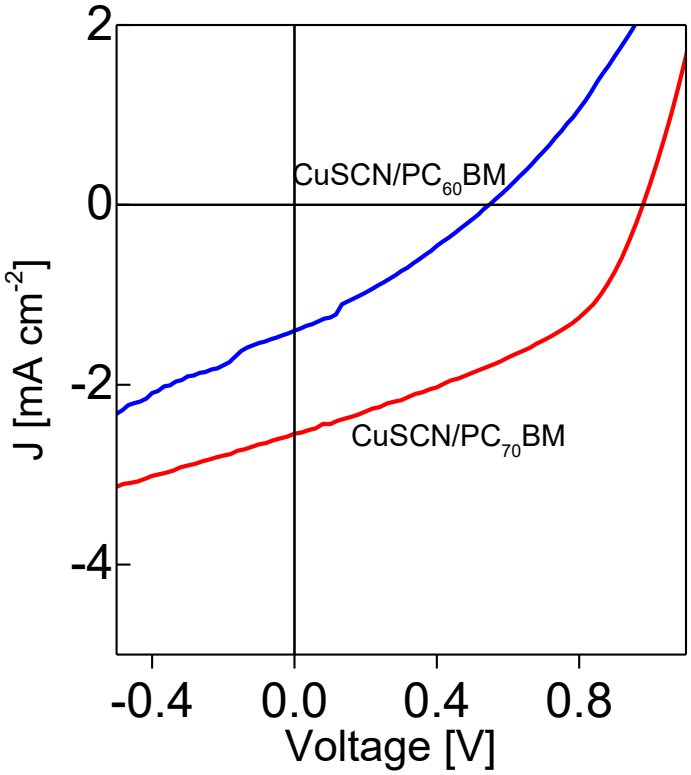

Figure 4.9 Current-voltage characteristics of planar $PC_{60}BM$ (blue) ,and $PC_{70}BM$

(red) photovoltaic device.

	V_{oc} [V]	J_{sc} [mAcm^{-2}]	*FF* [%]	*PCE* [%]
CuSCN/$PC_{60}BM$ (bilayer)	**0.52± 0.03 (0.55)**	**1.1±0.3 (1.4)**	**25±5 (29)**	**0.17± 0.05 (0.22)**
CuSCN/$PC_{70}BM$ (mixed layer)	**0.90± 0.01 (0.91)**	**2.2±0.1 (2.3)**	**50±3 (51)**	**1.1± 0.9 (1.1)**

Table 4.3 Device performance of planar $PC_{60}BM$ and $PC_{70}BM$ solar cells. The best device performance is shown in bracket

To understand the effectiveness of CuSCN and BCP, I also fabricated devices without CuSCN and BCP using $PC_{70}BM$ planar device, with the results shown in Figure 4.10. I note that in this control device, the open circuit voltage is 1 V, which is significantly different than the device in Figure 4.9. We have repeated similar experiment multiple times and found that the V_{oc} of CuSCN device fluctuates between 0.88 V to 1 V. Compared to organic solar cell, the variance in V_{oc} in the same device should be no more than 0.1 V. This variance could due to the processing conditions and the film formation inconsistency of CuSCN. Examining then, the results without the BCP layer, the device performance becomes slightly worse. There is a small drop in short circuit current, from 3.01 mA/cm^2 to 2.16 mA/cm^2 and a reduction in both open circuit voltage and fill factor leads to a decrease in the power conversion efficiency of 0.71% compared to 1.2% in the control device. Further, if only PEDOT:PSS is used as the hole transporting layer, the results show that without CuSCN device performs significantly worse than the control device. The short circuit current is reduced from 3.01 mA/cm^2 to only 0.45 mA/cm^2, in agreement with previous studies, and the open circuit voltage also reduces from 1 V to 0.28 V and the

overall power conversion efficiency is reduced from 1.2 to 0.04%. This indicates CuSCN plays a crucial role in this structure, perhaps due to the excellent electron blocking property to reduced exciton recombination.

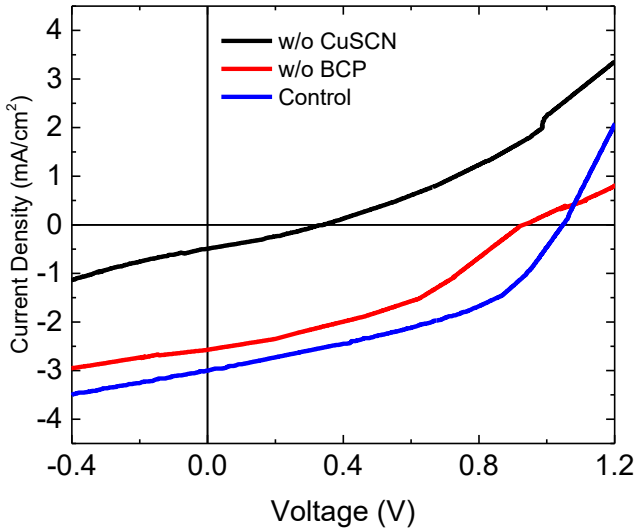

Figure 4.10 Device performance of $PC_{70}BM$ planar device without CuSCN (Black) or BCP (Red) as the interlayer. Blue curve represents the control device. The device performance is shown in Table 4.4.

	V_{oc} [V]	J_{sc} [mAcm^{-2}]	*FF* [%]	*PCE* [%]
ITO/PEDOT:PSS/CuSCN/$PC_{70}BM$/BCP/Al	**1.0± 0.2 (1.0)**	**3.0±0.5 (3.0)**	**38±3 (41)**	**1.0± 0.2 (1.2)**
ITO/PEDOT:PSS/CuSCN/PC70BM/Al	**0.78± 0.07 (0.82)**	**2.0±0.2 (2.2)**	**40±2 (40)**	**0.68±0.03 (0.71)**
ITO/PEDOT:PSS/$PC_{70}BM$/BCP/Al	**0.27± 0.03 (0.28)**	**0.45±0.05 (0.45)**	**28±2 (29)**	**0.02±0.02 (0.04)**

Table 4.4 Summary table of the planar $PC_{70}BM$ device performance without CuSCN or BCP as the interlayer. The best device performance is shown in bracket

To understand the energetic origin of the photocurrent, I measured the external quantum efficiency (EQE) of the CuSCN/$PC_{70}BM$ device (Figure 4.11), showing a

low EQE of less than 20%, but also that charge generation occurs across the whole absorption spectrum of $PC_{70}BM$. We also observed two peaks at around 380 nm and 480 nm, which corresponds to two strong absorption peaks from $PC_{70}BM$, confirming that $PC_{70}BM$ was the only light absorbing material for this photovoltaic device. It suggests that only approximately 10% of the incoming photons can eventually become charge to deliver electricity. Light absorption and charge dissociation efficiency have to be improved in order to make the device more efficient.

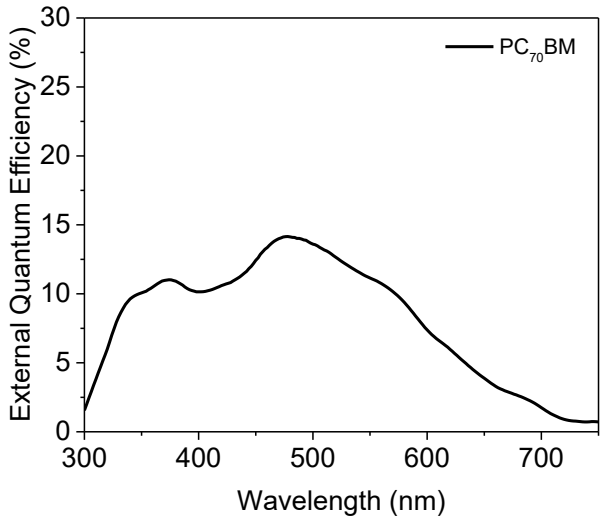

Figure 4.11 External quantum efficiency of the planar $PC_{70}BM$ device.

In order to understand whether the film morphologies of the layers affect device performance, atomic force microscope (AFM) images of size 1μm × 1μm of each layer were taken for film surface analysis (Figure 4.12). It shows that the CuSCN film is relatively compact, with a root mean square roughness of 4.4 nm and consists of elongated grain-like CuSCN nanocrystalline with a length of about

30-50 nm. On the other hand, pin holes are observed in films of $PC_{70}BM$ and $PC_{60}BM$, with a higher number found in $PC_{60}BM$ and of a smaller size than the pin holes in the $PC_{70}BM$ film. These pin holes are likely be the reason of poor device performance for planar $PC_{60}BM$ device because they might limit the current flow percolation and increase charge carrier recombination. Similarly, the presence of pin-holes in the $PC_{70}BM$ layer may explain the relatively low FF in devices and suggest further improvement may be possible if the pin holes can be eliminated. The height distribution (Figure 4.13) of the layer suggests that CuSCN is significantly rougher than other layers; this roughness may be detrimental to the formation of compact PCBM layer on top of the CuSCN.

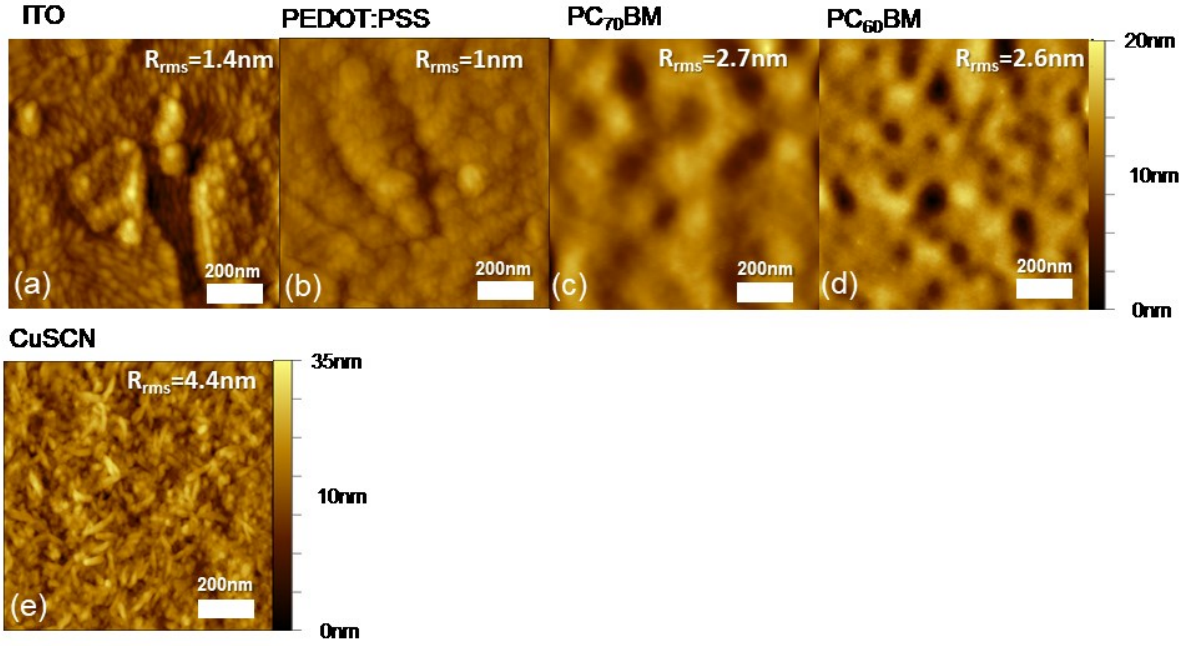

Figure 4.12 Atomic force microscope image of size 1μm × 1μm of a) ITO b) PEDOT:PSS c)$PC_{70}BM$ d) $PC_{60}BM$ e) CuSCN. The root mean square roughness is shown at the top right corner of each image.

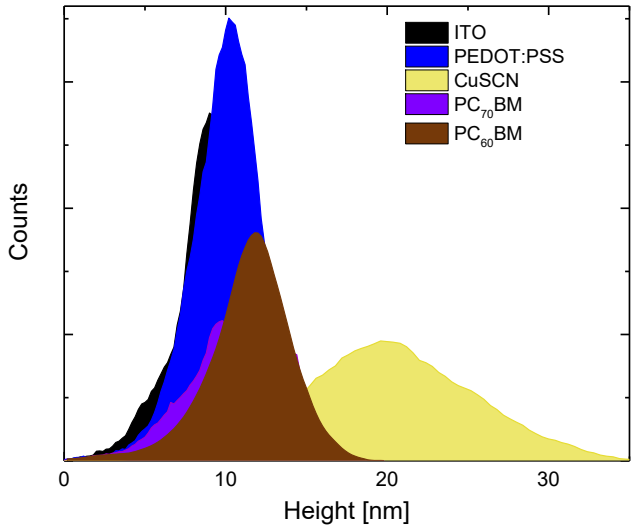

Figure 4.13 Height distribution of ITO, PEDOT:PSS, CuSCN, $PC_{70}BM$, and $PC_{60}BM$.

Figure 4.14 shows the thickness dependence measurements of CuSCN/$PC_{70}BM$ planar device with different $PC_{70}BM$ thickness. As the thickness is thin, the light absorption is not effective, which causes low short circuit current (1.4 mA/cm^2 at 35nm). If the $PC_{70}BM$ film thickness increases, the short circuit current increases up to an optimum value of 2.2 mA/cm^2 when film thickness is at 80 nm. However, higher film thickness will reduce the short-circuit current as the required diffusion length for the carrier is increased. This also suggests that the CuSCN/$PC_{70}BM$ interface facilitates charge generation. However, compared to the exciton diffusion length (≈10 nm), the device film thickness is still too thick for the carrier to be dissociated. Therefore, we have tried mixing PCBM and CuSCN to make a bulk heterojunction structure, which will be discussed in the next chapter.

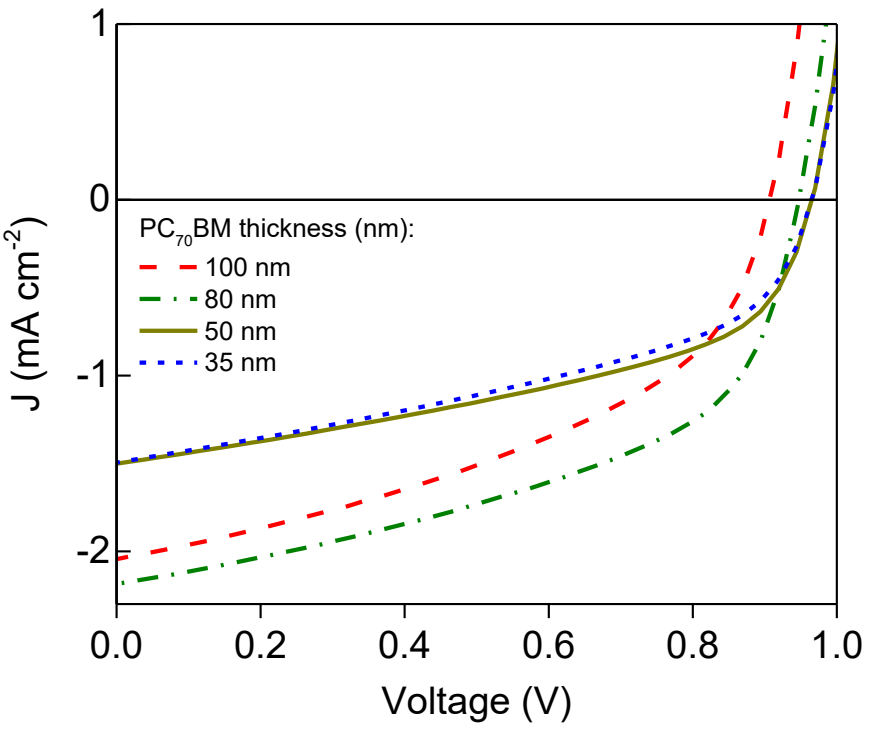

Figure 4.14 Device performance of $PC_{70}BM$ planar device at different $PC_{70}BM$ thickness.

$PC_{70}BM$ Thickness	V_{oc} [V]	J_{sc} [mA cm^{-2}]	*FF* [%]	*PCE* [%]
100 nm	**0.89**	**2.05**	**43**	**0.80**
80 nm	**0.93**	**2.2**	**47**	**0.94**
50 nm	**0.96**	**1.3**	**43**	**0.55**
35 nm	**0.96**	**1.4**	**44**	**0.57**

Table 4.5 Thickness dependence measurement of $PC_{70}BM$ layer of CuSCN/$PC_{70}BM$ device. Average values are shown.

4.4 Mixed phased PCBM based photovoltaic device

Whilst I have shown that in a planar configuration, a CuSCN/PCBM device can achieve a high open circuit voltage of up to 0.96 V, a limitation of such a cell

is the short-circuit current, which was only about 2 mA/cm^2. This is likely due to the small interface between CuSCN and PCBM, which limits charge generation. In order to address this, we therefore attempted to fabricate a solar cell with an increased CuSCN/PCBM interface by mixing CuSCN with methanofullerenes ($PC_{60}BM$ or $PC_{70}BM$) in the same solution in order to make a bulk-heterojunction-like device. We used a device structure is similar to the one used for the planar heterojunction as shown in Figure 4.15.

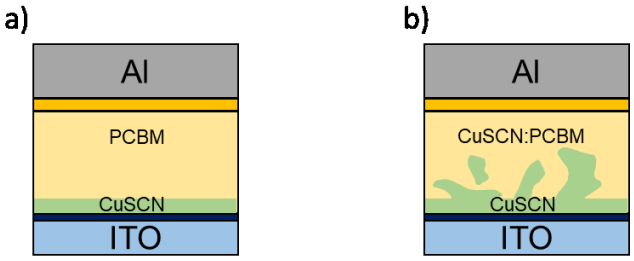

Figure 4.15 Structure of a) Planar CuSCN/PCBM and b) Mixed CuSCN:PCBM devices.

In this device, PEDOT:PSS has removed from the structure because we have found that PEDOT:PSS does not have any impact on the device performance. The current-voltage characteristics of devices mixing CuSCN with $PC_{70}BM$ and $PC_{60}BM$ are shown in Figure 4.16. In CuSCN:$PC_{60}BM$ blend, the V_{oc} has increased from 0.55V to 0.9V compared to the planar heterojunction. However, the short circuit current of 2.3mA/cm^2 is still low so that the power conversion efficiency is only 1.1%. The series resistance is also high and therefore poor fill factor was measured. On the other hand, the CuSCN:$PC_{70}BM$ blend has a significant improvement. The short-circuit current increased from 2.8mA/cm^2 to 10.8mA/cm^2. The open-circuit voltage stayed at a similar value of 0.93V, as compared to 0.9-0.96V was measured in the planar heterojunction device. Fill factor is increased to 58% because low series

resistance and high shunt resistance were measured. Such improvement helped the overall efficiency to achieve 5.1%. We also observed batch-to-batch variation. In some batch of the device, same recipe yielded approximately 4.3% to 5.9% PCE. It is unclear what caused such problem.

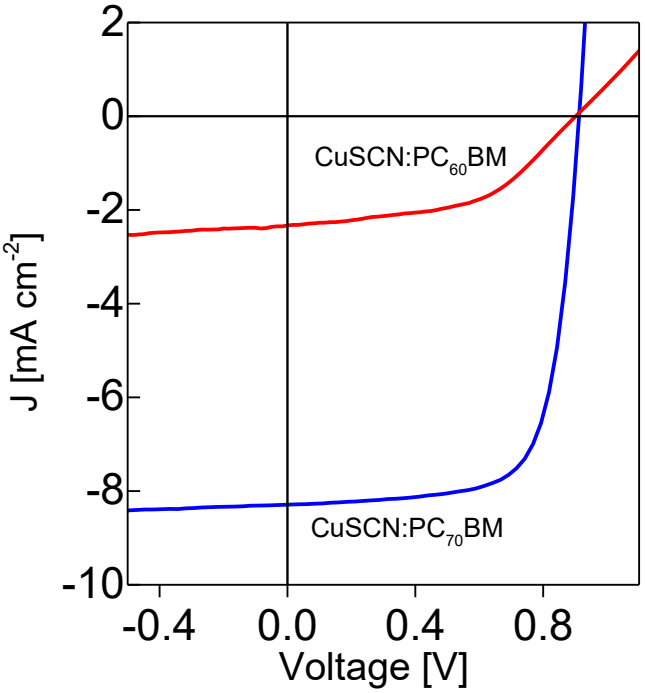

Figure 4.16 J-V characteristics of mixed CuSCN:$PC_{60}BM$ and mixed CuSCN:$PC_{70}BM$ device. The pre-mixed ratio of precursor solution of CuSCN:$PC_{76}BM$ ratio CuSCN:$PC_{70}BM$ are 1:3 volume ratio.

Active Layer	J_{sc} [$mAcm^{-2}$]	V_{oc} [V]	*FF* [%]	*PCE* [%]	R_{series} [Ω]	R_{shunt} [Ω]
CuSCN:$PC_{60}BM$	2.3	0.90	51	1.1	736	1556
CuSCN:$PC_{70}BM$	7.9	0.91	71	5.1	32	21300

Table 4.6 Performance of mixed CuSCN:$PC_{60}BM$ and CuSCN:$PC_{70}BM$ devices.

An optimization process was done to achieve the power conversion efficiency. The precursor CuSCN:$PC_{70}BM$ solution was made by mixing the CuSCN:$PC_{70}BM$ solution under different volume ratio. Figure 4.17 shows the

comparison of CuSCN:$PC_{70}BM$ device at three different ratios. The mixed CuSCN:$PC_{70}BM$ device works best when the volume ratio is 1:3 (25μL :75μL). Changing the ratio between then will change the short circuit current significantly, meaning the charge generation or charge collection will become ineffective at other ratios. Also, the open circuit voltage has no significant difference at different ratio. In our best device (ratio of 1:3), the V_{oc} is 0.91 V.

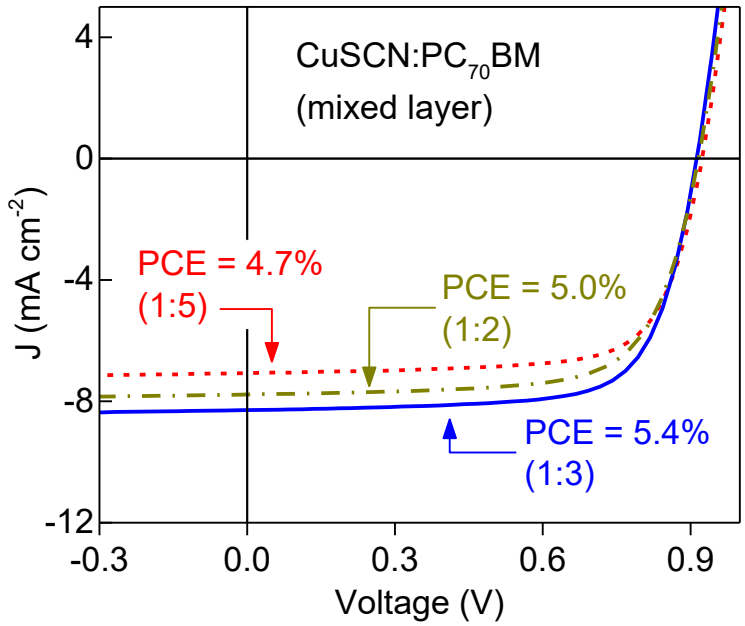

Figure 4.17 J-V characteristics mixed CuSCN:PC7$_0$BM device under different volume ratio in the precursor solution.

CuSCN:$PC_{70}BM$	V_{oc} [V]	J_{sc} [mA cm^{-2}]	*FF* [%]	*PCE* [%]
1:5	0.92	7.0	71	4.6
1:3 (Best)	0.91 (0.91)	7.9 (8.3)	71 (72)	5.1 (5.4)
1:2	0.91	7.8	70	5.0

Table 4.7 Performance of mixed CuSCN:$PC_{70}BM$ devices at different volume ratio.

As discussed before, a large batch-to-batch variation is observed in our device as

shown in Figure 4.18. In the figure, we have shown the distribution of totally 58 identical devices of CuSCN:$PC_{70}BM$ device at 1:3 ratio. The device performance is randomly distributed with the mean power conversion efficiency of about 5.1%.

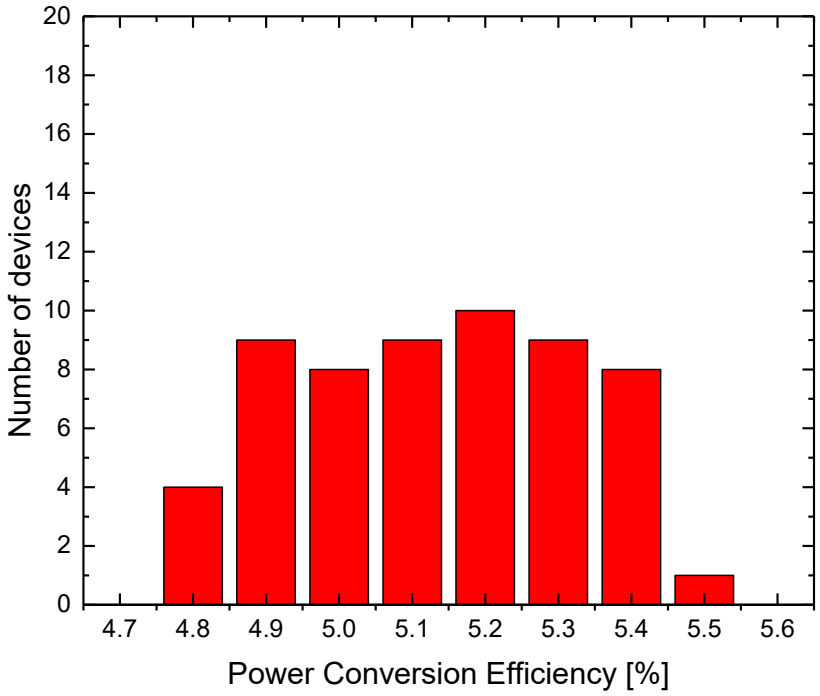

Figure 4.18 Distribution of power conversion efficiency of 58 CuSCN:$PC_{70}BM$ device with identical structure and processing method. The mean is 5.15% and standard deviation is 1.9%

We also measured the EQE spectrum of mixed CuSCN:$PC_{70}BM$ and compared it to planar CuSCN/$PC_{70}BM$ devices (Figure 4.19). The result shows that the external quantum efficiency can now achieve more than 50% in the mixed phase. The integrated photocurrent of 7.93 mA/cm^2 also agrees with the experimental results.

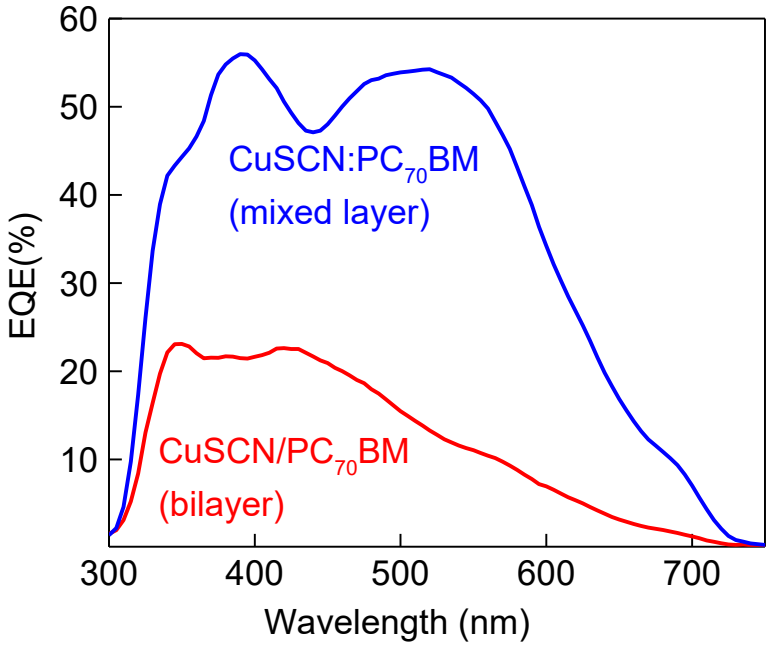

Figure 4.19 External quantum efficiency spectrum of planar CuSCN/$PC_{70}BM$ and mixed CuSCN:$PC_{70}BM$.

In order to find out the origin of the improvement of mixed CuSCN:$PC_{70}BM$ device, we have measured the cross-sectional image using the high-resolution transmission electron microscopy (TEM). Figure 4.20a and Figure 4.20b shows the cross-sectional TEM image of planar CuSCN/$PC_{70}BM$ and mixed CuSCN:$PC_{70}BM$, respectively. We found that both photoactive layers turned out to be very different from each other. First, in planar CuSCN/$PC_{70}BM$ device, we could clearly see all the interlayers. The compact CuSCN layer is relatively rougher than other layers, which agrees with the result from the AFM analysis, where CuSCN shows the highest root-mean-square roughness. Also, the thicknesses of all layers agree with our measurements. From the image, the photoactive layer of $PC_{70}BM$ is about 50 nm, which is much greater than the electron-hole pair diffusion length. We believe

this is the origin of the low J_{sc} in the planar device. On the other hand, for mixed CuSCN:$PC_{70}BM$ device, instead of bulk heterojunction structure of CuSCN and PCBM, which both materials should be mixed together randomly. Instead, we could observe nanowires (NWs) protrude from the compact hole transporting CuSCN layer. The NWs are randomly oriented, and the length of the NWs ranging from 30 nm to 100 nm. Note that these images were taken with PEDOT:PSS was still used as the hole injection layer on top of ITO. Nevertheless, later we have taken similar images without PEDOT:PSS and CuSCN NWs can still be found in the photoactive layer (Figure 4.21).

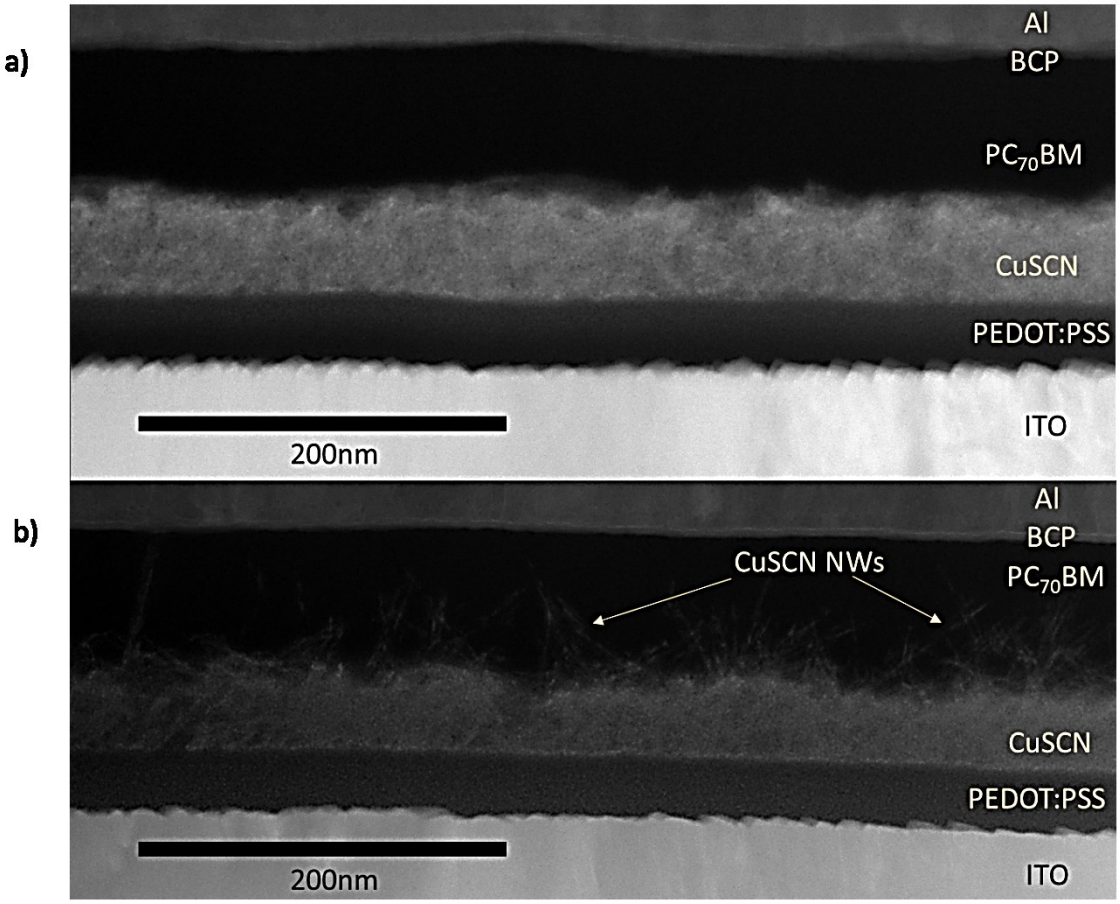

Figure 4.20 Cross-sectional TEM image of a) Planar CuSCN:$PC_{70}BM$ device and b) Mixed CuSCN:$PC_{70}BM$ device. These images were taken by Dr. Claire Burgess.

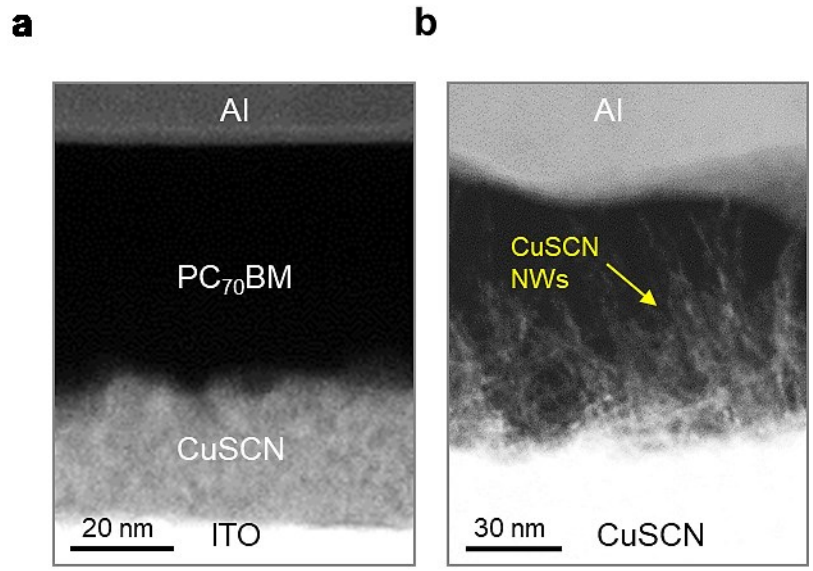

Figure 4.21 Cross-sectional TEM image of a) Planar CuSCN:$PC_{70}BM$ device and b) Mixed CuSCN:$PC_{70}BM$ device without PEDOT:PSS as the hole injection layer. These images were taken by Dr. Claire Burgess.

To further confirm the composition of such nanowires, we have performed the elemental mapping using the electron energy loss spectroscopy (EELs). Figure 4.22 shows the EELs cross sectional image of planar CuSCN/$PC_{70}BM$ and mixed CuSCN:$PC_{70}BM$ devices, where copper and carbon elements are marked in green and red, respectively. We could confirm that the NWs are made by CuSCN and these NWs are the origin of remarkably increase of short circuit current in the device.

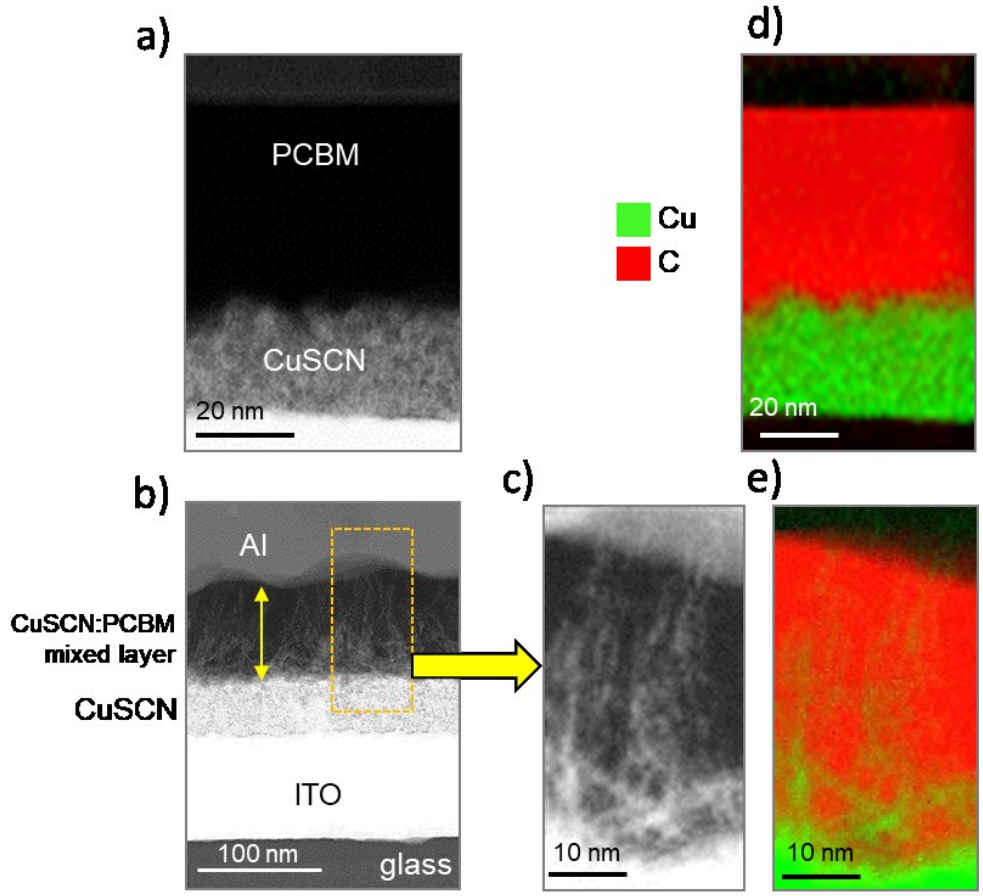

Figure 4.22 Cross-sectional TEM image of planar CuSCN/$PC_{70}BM$ device. b) Cross-sectional TEM image of mixed CuSCN:$PC_{70}BM$. c) Enlarged image of CuSCN NWs in mixed CuSCN:$PC_{70}BM$ film. d) EELs image of planar CuSCN/$PC_{70}BM$ device. e) EELs image of mixed CuSCN:$PC_{70}BM$ device. Red color denotes carbon rich region and green color denotes copper rich region. These images were taken by Dr. Yuliar Firdaus.

Although there are other reports about the application of CuSCN NWs used in photovoltaic applications, which are mainly based in inorganic solar cell, their CuSCN NWs are usually thicker and longer (from 200 nm to up to 1 μm), which is not suitable for organic photovoltaics.[11,42] It is because the typical film thickness of organic solar cell is in the range of 100 nm, which is limited by the diffusion length of carriers. However, in the CuSCN NWs we observed, it may possibly be an improvement of

ordinary bulk heterojunction system. In fact, such nanostructure is very similar to the ideal bulk heterojunction to achieve maximum charge dissociation efficiency (Figure 4.23). In ideal bulk heterojunction (Figure 4.23b), both electron donor and acceptor overlap on each other to maximize the interfacial area. Such large interfacial area provides charge extraction sites for photoexcited electron hole pairs. In such nanostructure, holes and electrons can diffuse to their corresponding electrodes in a short range without undergoing recombination process. However, in practice, making such nanostructure is challenging. In the current research in organic solar cell, bulk heterojunction is usually reported to be a random mixture of both donor and acceptor. Such morphology may also change under certain processing conditions.[43–45] For instance, PCBM are found to aggregate under thermal annealing near the cathode to improve the charge extraction efficiency.[46,47] On the other hand, we have demonstrated a new type of nanostructure created by CuSCN, which is similar to the ideal bulk heterojunction structure. Such long and ultra-thin CuSCN NWs provide large interfacial area for the holes of a bounded exciton to be collected.

Figure 4.24 shows the illustrative diagrams of both BHJ and CuSCN NW devices to compare the charge separation effectiveness. In BHJ device, both electron donor and electron acceptors are randomly formed inside the bulk layer, which means there could be some isolated domains that holes, or electrons could not be transported to the corresponding electrodes. Energetically, the trapped carrier trapped by due to this isolation because there are no energy states nearby with similar energy level as shown in Figure 4.25. This effect forces those isolated carriers to eventually recombine and thus reduced the short-circuit current. On the other hand, in the CuSCN NWs layer, since CuSCN NWs protrude from the compact CuSCN hole transporting layer, most

carriers that are formed near the CuSCN NWs can be transported to the corresponding electrodes because the CuSCN NWs are connected to the compact CuSCN layer.

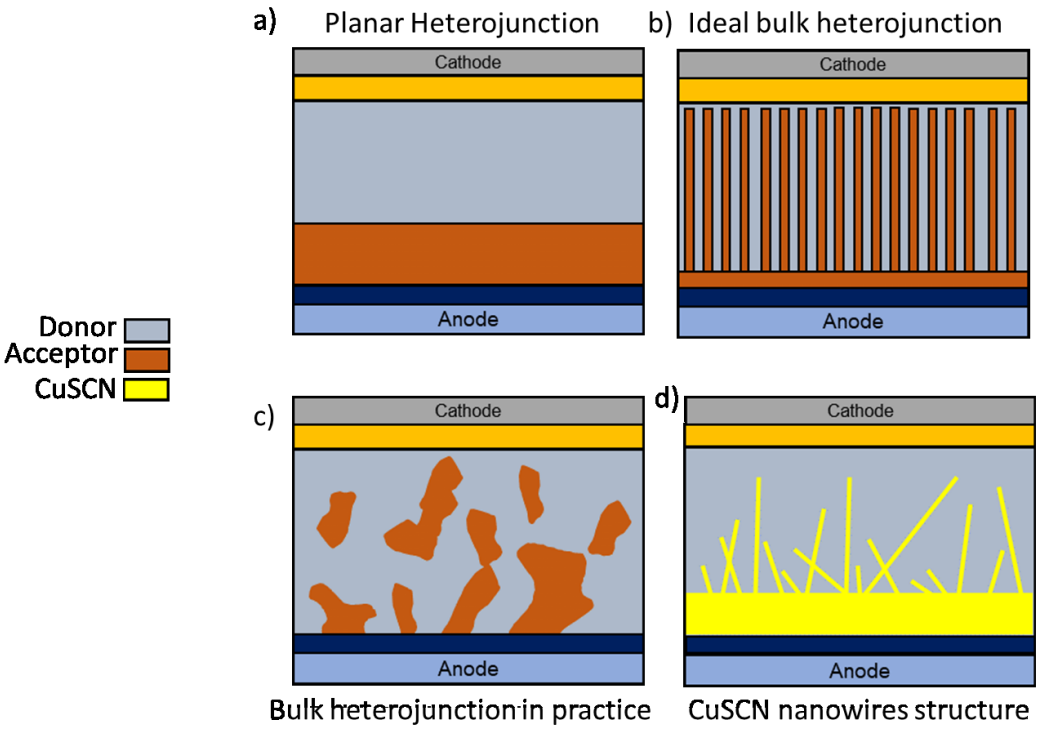

Figure 4.23 Illustrative diagram of a) planar heterojunction, b) ideal bulk heterojunction, c) bulk heterojunction in practice, and d) CuSCN nanowires structure.

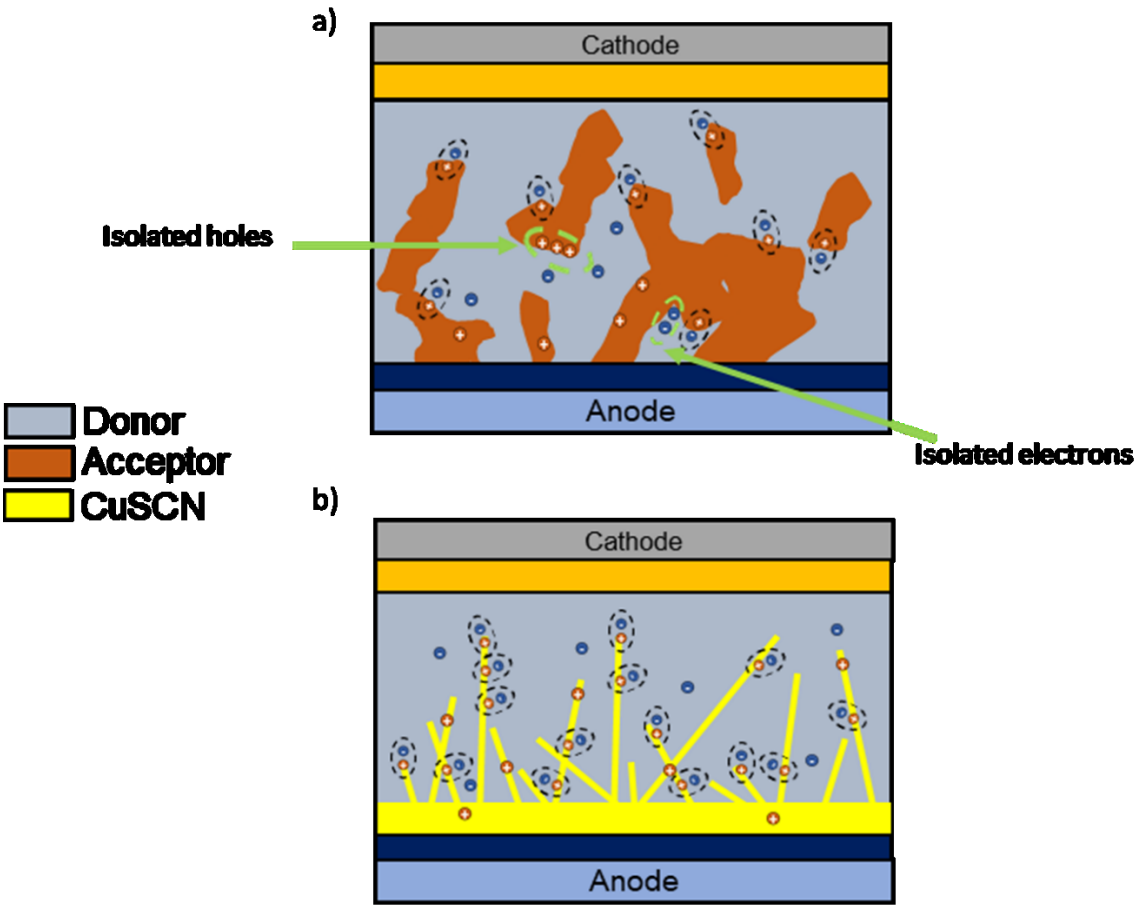

Figure 4.24 Illustrative diagrams show the charge carrier separation in a) Bulk heterojunction and b) CuSCN NWs structure.

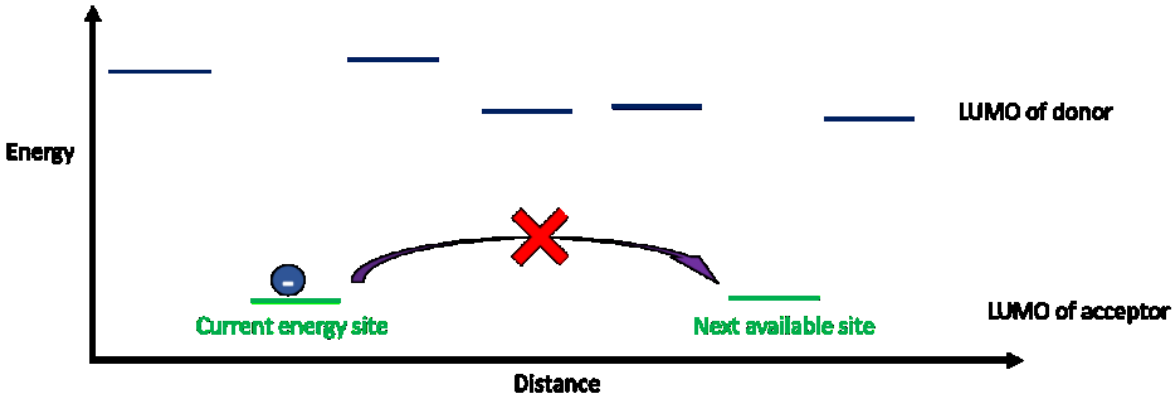

Figure 4.25 Energy distance diagram that shows an isolated electron is surrounded by LUMO energy states of donor, which has a higher energy level. As a result, this electron is trapped and could not be transported to the cathode.

4.5 Density functional theory calculation of CuSCN/C60 interface

To understand the energetics inside the CuSCN:$PC_{70}BM$ device. Our collaborators used density functional theory (DFT) calculation to model the interface between β-CuSCN and C_{60} crystals by the DFT-Heyd-Scuseria-Erzerhof level (HSE). Since $PC_{70}BM$ is asymmetric and the orientation of the molecule is difficult to involve in the calculation, the assumption that the functional groups in $PC_{60}BM$ and $PC_{70}BM$ only affect the solubility and there is no or insignificant impact on the electronic properties are made. They have found that the non-polar $(11\bar{2}0)$ of β-CuSCN has small formation energy.[48] The results are found to be similar when C_{60} and C_{70} are used in the model. The adsorption energies over the sulfur atom, copper atom, and C-N bonds are found to be very similar. Figure 4.26 shows the optimized atomistic structure when a C_{60} molecule is adsorbed on C-N bond.

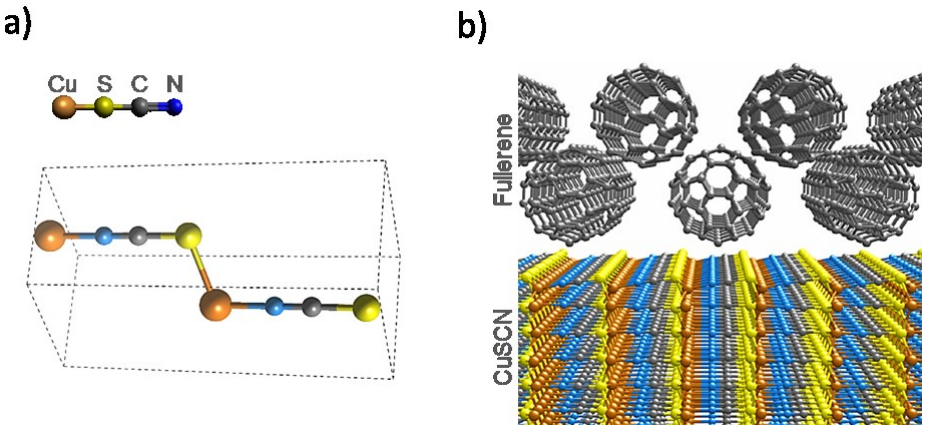

Figure 4.26 a) A unit cell of β-CuSCN and b) Atomistic model showing the interface between $(11\bar{2}0)$ surface β-CuSCN and C_{60}, where C_{60} is lying on top of C-N bond. This figure was drawn by Dr. George Volonakis and it is adapted via Creative Commons Attribution License from reference 49. [49]

Our collaborators have also analysed the band structure of CuSCN/C_{60} interface. They have concluded that the hole extraction from C_{60} is favored, because the

valence band top (VBT) of CuSCN is 0.5 eV higher than the VBT of C_{60} (Figure 4.27). On the other hand, the conduction band bottom (CBB) of CuSCN is 1.6 eV higher than C_{60} therefore CuSCN acts as an electron blocking layer. The maximum theoretical V_{oc} can be achieved by CuSCN and C_{60} is found to be 1.7 V. Finally, the effective charge carrier masses for CuSCN and C_{60} are determined using the HSE hybrid functional. For CuSCN, electron effective mass and hole effective mass are $0.3m_e$ and $0.8m_e$ along the central axis of β-CuSCN, respectively, where m_e is the mass of an electron. In the plane perpendicular to the central axis, the effective mass of electron is $0.5m_e$. Light holes and heavy holes are also found to have $0.5m_e$ and $1.5m_e$. On the other hand, considering the C_{60} solid. The effective masses of hole are isotropic, with an effective mass ranging from $0.6m_e$ to $0.8\ m_e$. The effective mass of electron is $0.7m_e$ along the direction that connects to the next C_{60} in a face-center cubic arrangement. The similarity in both hole and electron effective masses suggests that the hole and electron mobilities are similar, which confirm the validity of our result from FET measurements.

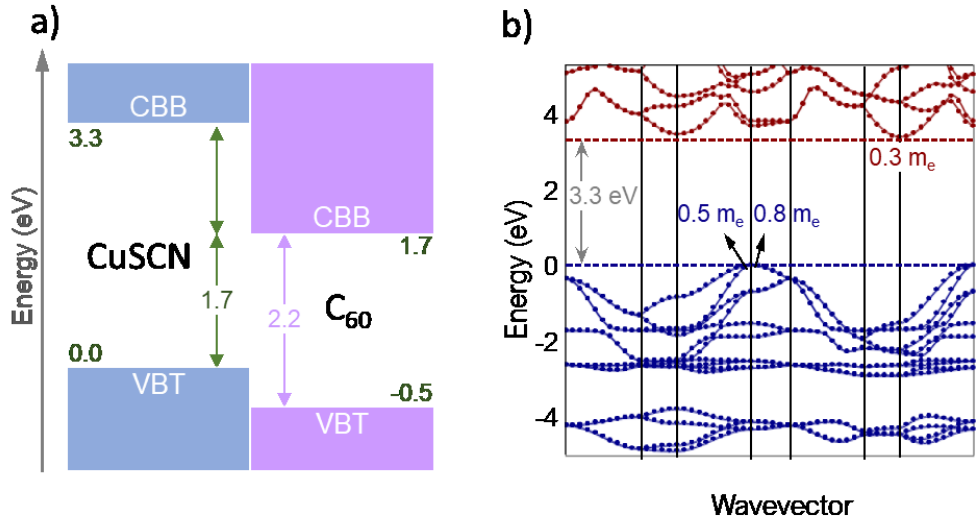

Figure 4.27 a) Band energy alignment diagram of CuSCN/C_{60} interface. b) DFT-HSE electron band structure of β-CuSCN. This figure was drawn by Dr. George Volonakis and it is adapted via Creative Commons Attribution License from reference 49. [49]

4.6 Photogeneration and recombination in CuSCN/$PC_{70}BM$ device

Another group of collaborator at King Abdullah University of Science and Technology (KAUST) also studied the carrier generation and recombination of the CuSCN:$PC_{70}BM$ device.[50] The effectiveness of electron blocking ability of CuSCN is further confirmed in Figure 4.28. In a CuSCN/$PC_{70}BM$ device, when molybdenum trioxide MoO_3, PEDOT:PSS, and CuSCN were used as the hole transporting layers, very low J_{sc} (<0.1 mA/cm^2) was achieved if the hole transporting layers are either PEDOT:PSS or MoO_3 . Secondly, they have found that the charge generation efficiency and collection efficiency have improved by 50% if a mixed CuSCN:$PC_{70}BM$ over planar CuSCN/$PC_{70}BM$ device. Such improvement is originated from the reduction in both geminate and non-geminate recombination.

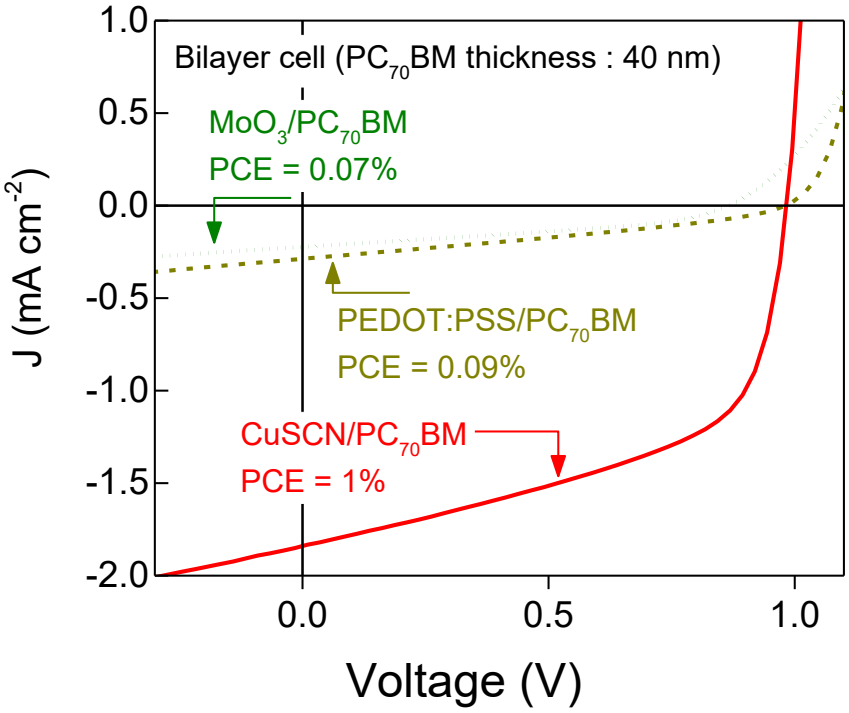

Figure 4.28 J-V characteristics of planar $PC_{70}BM$ device using MoO_3, PEDOT:PSS, CuSCN as the hole injection layer. The Figure was created by Dr. Yuliar Firdaus and was adapted via John Wiley and Sons (Licence number 4704371468166) from reference 50.[50]

4.7 Conclusion and future work

We have found that in CuSCN NWs can be formed when it is deposited in a mixed CuSCN:PC70BM solution on top of CuSCN compact layer. Such structure is proven to be unique and promising, as we measured from the photovoltaic device. High open-circuit voltage of 0.98 V was measured. We believe that the limitation of our current CuSCN:$PC_{70}BM$ device is mainly from the short-circuit current, because the light absorption of $PC_{70}BM$ is still low compared to existing organic or inorganic semiconductors, resulting low photogeneration inside the photoactive layer and therefore the amount of collected free carriers. To date, CuSCN:$PC_{70}BM$ is the only

system we could observe CuSCN-NWs. In the future, the origin of formation of CuSCN NW should be studied by either testing different light absorbing electron donor mixed with CuSCN or to understand the CuSCN:$PC_{70}BM$ interface fundamentally.

References:

[1] C.Jiang, L.Jing, X.Huang, M.Liu, C.Du, T.Liu, X.Pu, W.Hu, Z. L.Wang, *ACS Nano* **2017**, *11*, 9405.

[2] M.Knudsen, *Prog. Photovoltaics Res. Appl.* **1934**, *17*, 183.

[3] C. D.Bailie, M. G.Christoforo, J. P.Mailoa, A. R.Bowring, E. L.Unger, W. H.Nguyen, J.Burschka, N.Pellet, J. Z.Lee, M.Grätzel, R.Noufi, T.Buonassisi, A.Salleo, M. D.McGehee, *Energy Environ. Sci.* **2015**, *8*, 956.

[4] M.Wright, A.Uddin, *Sol. Energy Mater. Sol. Cells* **2012**, *107*, 87.

[5] https://www.nrel.gov/pv/cell-efficiency.html.

[6] P.Pattanasattayavong, G. O. N.Ndjawa, K.Zhao, K. W.Chou, N.Yaacobi-Gross, B. C.O'Regan, A.Amassian, T. D.Anthopoulos, *Chem. Commun.* **2013**, *49*, 4154.

[7] N.Yaacobi-Gross, N. D.Treat, P.Pattanasattayavong, H.Faber, A. K.Perumal, N.Stingelin, D. D. C.Bradley, P. N.Stavrinou, M.Heeney, T. D.Anthopoulos, *Adv. Energy Mater.* **2015**, *5*, 1401529.

[8] P.Pattanasattayavong, N.Yaacobi-Gross, K.Zhao, G. O. N.Ndjawa, J.Li, F.Yan, B. C.O'Regan, A.Amassian, T. D.Anthopoulos, *Adv. Mater.* **2013**, *25*, 1504.

[9] N.Wijeyasinghe, A.Regoutz, F.Eisner, T.Du, L.Tsetseris, Y. H.Lin, H.Faber, P.Pattanasattayavong, J.Li, F.Yan, M. A.McLachlan, D. J.Payne, M.Heeney, T. D.Anthopoulos, *Adv. Funct. Mater.* **2017**, *27*, 35

[10] A.Montgomery, L.Guo, C.Grice, R. A.Awni, S.Saurav, L.Li, Y.Yan, F.Yan, *Prog. Photovoltaics Res. Appl.* **2019**, 665.

[11] C.Lévy-Clément, R.Tena-Zaera, M. A.Ryan, A.Katty, G.Hodes, *Adv. Mater.* **2005**, *17*, 1512.

[12] G. R. R. A.Kumara, A.Konno, G. K. R.Senadeera, P. V. V.Jayaweera, D. B. R. A.DeSilva, K.Tennakone, *Sol. Energy Mater. Sol. Cells* **2001**, *69*, 195.

[13] G. A.Sepalage, S.Meyer, A. R.Pascoe, A. D.Scully, U.Bach, Y. B.Cheng, L.Spiccia, *Nano Energy* **2017**, *32*, 310.

[14] M. P.DeJong, L. J.VanIjzendoorn, M. J. A.DeVoigt, *Appl. Phys. Lett.* **2000**, *77*, 2255.

[15] J. W.Jung, C. C.Chueh, A. K. Y.Jen, *Adv. Energy Mater.* **2015**, *5*, 1.

[16] A.Casey, J. P.Green, P.Shakya Tuladhar, M.Kirkus, Y.Han, T. D.Anthopoulos, M.Heeney, *J. Mater. Chem. A* **2017**, *5*, 6465.

[17] B.O'Regan, F.Lenzmann, R.Muis, J.Wienke, *Chem. Mater.* **2002**, *14*, 5023.

[18] N.Wijeyasinghe, T. D.Anthopoulos, *Semicond. Sci. Technol.* **2015**, *30*, 104002.

[19] X.Wu, L.Xie, K.Lin, J.Lu, K.Wang, W.Feng, B.Fan, P.Yin, Z.Wei, *J. Mater. Chem. A* **2019**, *7*, 12236.

[20] I. S.Yang, S.Lee, J.Choi, M. T.Jung, J.Kim, W. I.Lee, *J. Mater. Chem. A* **2019**, *7*, 6028.

[21] L.Petti, P.Pattanasattayavong, Y. H.Lin, N.Münzenrieder, G.Cantarella, N.Yaacobi-Gross, F.Yan, G.Tröster, T. D.Anthopoulos, *Appl. Phys. Lett.* **2017**, *110*

[22] Y.Ji, H. J.Lee, S.Lee, K. G.Cho, K. H.Lee, K.Hong, *Adv. Mater. Interfaces* **2019**, *1900883*, 1900883.

[23] G.Wyatt-Moon, D. G.Georgiadou, J.Semple, T. D.Anthopoulos, *ACS Appl. Mater. Interfaces* **2017**, *9*, 41965.

[24] Z.Yang, M.Wang, J.Ding, Z.Sun, L.Li, J.Huang, J.Liu, J.Shao, *ACS Appl.*

Mater. Interfaces **2015**, *7*, 21235.

[25] J.Garnier, R.Parize, E.Appert, O.Chaix-Pluchery, A.Kaminski-Cachopo, V.Consonni, *ACS Appl. Mater. Interfaces* **2015**, *7*, 5820.

[26] Y.Zhu, H.Hu, J.Lin, F.Li, T.Guo, *SID Symp. Dig. Tech. Pap.* **2019**, *50*, 1693.

[27] L.Xu, Y.Li, L.Chen, J.Wang, C.Zheng, Y.Qi, R.Chen, W.Huang, *ACS Sustain. Chem. Eng.* **2018**, *6*, 17178.

[28] L. J.Xu, J. Y.Wang, X. F.Zhu, X. C.Zeng, Z. N.Chen, *Adv. Funct. Mater.* **2015**, *25*, 3033.

[29] A.Perumal, H.Faber, N.Yaacobi-Gross, P.Pattanasattayavong, C.Burgess, S.Jha, M. A.McLachlan, P. N.Stavrinou, T. D.Anthopoulos, D. D. C.Bradley, *Adv. Mater.* **2015**, *27*, 93.

[30] S. D.Chavhan, T. H.Ou, M. R.Jiang, C. W.Wang, J. H.Jou, *J. Phys. Chem. C* **2018**, *122*, 18836.

[31] K.Itaka, M.Yamashiro, J.Yamaguchi, M.Haemori, S.Yaginuma, Y.Matsumoto, M.Kondo, H.Koinuma, *Adv. Mater.* **2006**, *18*, 1713.

[32] R. C.Haddon, *J. Am. Chem. Soc.* **1996**, *118*, 3041.

[33] A.Diaz De Zerio Mendaza, J.Bergqvist, O.Bäcke, C.Lindqvist, R.Kroon, F.Gao, M. R.Andersson, E.Olsson, O.Inganäs, C.Müller, *J. Mater. Chem. A* **2014**, *2*, 14354.

[34] H. S.Lin, I.Jeon, R.Xiang, S.Seo, J. W.Lee, C.Li, A.Pal, S.Manzhos, M. S.Goorsky, Y.Yang, S.Maruyama, Y.Matsuo, *ACS Appl. Mater. Interfaces* **2018**, *10*, 39590.

[35] M. M.Wienk, J. M.Kroon, W. J. H.Verhees, J.Knol, J. C.Hummelen, P. A.VanHal, R. A. J.Janssen, *Angew. Chemie - Int. Ed.* **2003**, *42*, 3371.

[36] J. C.Hummelen, B. W.Knight, F.Lepeq, F.Wudl, J.Yao, C. L.Wilkins, *J. Org. Chem.* **1995**, *60*, 532.

[37] P. H.Wöbkenberg, D. D. C.Bradley, D.Kronholm, J. C.Hummelen, D. M.deLeeuw, M.Cölle, T. D.Anthopoulos, *Synth. Met.* **2008**, *158*, 468.

[38] T. D.Anthopoulos, C.Tanase, S.Setayesh, E. J.Meijer, J. C.Hummelen, P. W. M.Blom, D. M.DeLeeuw, *Adv. Mater.* **2004**, *16*, 2174.

[39] A. K. K.Kyaw, D. H.Wang, H. R.Tseng, J.Zhang, G. C.Bazan, A. J.Heeger, *Appl. Phys. Lett.* **2013**, *102*, 4802922.

[40] C. H. Y.Ho, S. H.Cheung, H. W.Li, K. L.Chiu, Y.Cheng, H.Yin, M. H.Chan, F.So, S. W.Tsang, S. K.So, *Adv. Energy Mater.* **2017**, *7*, 1602360.

[41] B.Yang, F.Guo, Y.Yuan, Z.Xiao, Y.Lu, Q.Dong, J.Huang, *Adv. Mater.* **2013**, *25*, 572.

[42] C.Chappaz-Gillot, R.Salazar, S.Berson, V.Ivanova, *Electrochem. commun.* **2012**, *24*, 021107.

[43] H.Hoppe, N. S.Sariciftci, *J. Mater. Chem.* **2006**, *16*, 45.

[44] J. S.Moon, J. K.Lee, S.Cho, J.Byun, A. J.Heeger, *Nano Lett.* **2009**, *9*, 230.

[45] C. M.Liu, M. S.Su, J. M.Jiang, Y. W.Su, C. J.Su, C. Y.Chen, C. S.Tsao, K. H.Wei, *ACS Appl. Mater. Interfaces* **2013**, *5*, 5413.

[46] J. G.Labram, E. B.Domingo, N.Stingelin, D. D. C.Bradley, T. D.Anthopoulos, *Adv. Funct. Mater.* **2011**, *21*, 356.

[47] T.Agostinelli, S.Lilliu, J. G.Labram, M.Campoy-Quiles, M.Hampton, E.Pires, J.Rawle, O.Bikondoa, D. D. C.Bradley, T. D.Anthopoulos, J.Nelson, J. E.MacDonald, *Adv. Funct. Mater.* **2011**, *21*, 1701.

[48] L.Tsetseris, *J. Phys. Condens. Matter* **2016**, *28*, 295801.

[49] W. Y.Sit, F. D.Eisner, Y. H.Lin, Y.Firdaus, A.Seitkhan, A. H.Balawi, F.Laquai, C. H.Burgess, M. A.McLachlan, G.Volonakis, F.Giustino, T. D.Anthopoulos, *Adv. Sci.* **2018**, *5*, 1700980

[50] Y.Firdaus, A.Seitkhan, F.Eisner, W.-Y.Sit, Z.Kan, N.Wehbe, A. H.Balawi, E.Yengel, S.Karuthedath, F.Laquai, T. D.Anthopoulos, *Sol. RRL* **2018**, *2*, 1800095.

Chapter 5. Improving the power conversion efficiency of CuSCN:$PC_{70}BM$ photovoltaic device

In the previous chapter, we have found that the formation of CuSCN NWs is crucial to improve the CuSCN:$PC_{70}BM$ solar cell device, due to the improved charge generation and reduced geminate and non-geminate recombination of the device compared to a planar heterojunction. It is worth noting that the performance of NW based solar cells was found to be sensitive to fabrication conditions, and in particular the temperature of the casting solution, the temperature of the substrate and the concentration of each material in solution. Although we do not understand the formation mechanism of such NWs, we believe that each of these changes in processing conditions changes the morphology of the NW matrix, and believe that that further manipulation of the formation of NWs could improve the device performance. In this chapter, we will discuss our efforts to optimize the CuSCN:$PC_{70}BM$ device through the following approaches: 1) Changing the CuSCN-NWs formation conditions 2) Attempts to increase the density of NWs. 3) Adding metal nanoparticles to create plasmonic effect to improve light absorption in CuSCN:$PC_{70}BM$ layer. Importantly, although the device performance is highly depended on the processing condition, our device can still be compared within the same batch of device as the fabrication conditions are identical. The variance of the device performance are also outlined in this chapter.

5.1 Changing the formation conditions of CuSCN nanowires

We believe that CuSCN NWs are formed when mixed CuSCN:$PC_{70}BM$ solution is spun onto the compact CuSCN layer, and that this step is crucial in determining the morphology of the NWs. Therefore, we systematically control and the change the spin-

coating conditions for CuSCN:$PC_{70}BM$ nanowires, in order to improve performance. In our control device (structure shown in Figure 5.1a), after depositing the compact CuSCN layer, the substrate was held on a hot plate at a 100ºC, before being quickly transferred to the spin-coater chuck and a CuSCN:$PC_{70}BM$ solution was deposited onto the substrate, followed by initiating spin-coating at 2000 rpm. The ratio between CuSCN and $PC_{70}BM$ in the precursor solution is 1:3, with the concentration of CuSCN and $PC_{70}BM$ of 25mg/ml, and 30mg/ml, respectively. After the spin-coating process, the substrate is then put back onto the 100ºC hotplate to be annealed for another 15 minutes. The procedure to control the temperature of the substrate is as follows: The time to transfer the substrate to the chuck of the spin coater and prepare the CuSCN:$PC_{70}BM$ solution would normally take about 20-25seconds. During this time interval, there will be heat loss of the substrate to the surrounding. Therefore, we used an infrared thermometer to measure the temperature substrate, which in the control device is at about 95ºC just before spin coating. The temperature of the substrate depends on the ambient temperature and it is difficult to control. To tackle this problem, we also attempted to heat the spin coater chuck on the hotplate to avoid significant heat loss from the substrates when the substrate was transferred to the chuck, which allows us to have a greater repeatability between different batches. We then performed a series of experiments with different substrate temperatures. Figure 5.1b shows the *J-V* characteristics of the CuSCN:$PC_{70}BM$ solar cells with different substrate temperature. The device performance of CuSCN:PCBM NW devices where the substrate temperature just before spin coating is varied is summarized in Table 5.1. The variation of V_{oc}, J_{sc}, *FF*, and *PCE* as a function of substrate temperature is shown in Figure 5.2. When the substrate is spin-coated when the temperature is the lowest temperature (48ºC), a lower short-circuit current density

(~6mA/cm^2) was measured compared to the control device, in which the substrate temperature was 95 ºC. Interestingly, the V_{oc} is higher for the lower temperature device, and is a similar value to that of the planar heterojunction (0.98V). This might suggest that nanowire formation is less pronounced in these lower temperature devices. Increasing substrate temperature increases the collected short-circuit current density to a maximum value of 11mA/cm^2 when the substrate temperature is at 115ºC. However, the V_{oc} shows a decreasing trend when the substrate temperature increases and therefore, there is a tradeoff between J_{sc} and V_{oc} to achieve maximum efficiency, although there appears to be a relatively large temperature window (95ºC to 150ºC) around the maximum power conversion efficiency. The FF appears to be the variable that is most difficult to control, with no clear trend with temperature. This suggests that charge transport through the NW matrix may be very sensitive to the NW morphology obtained.

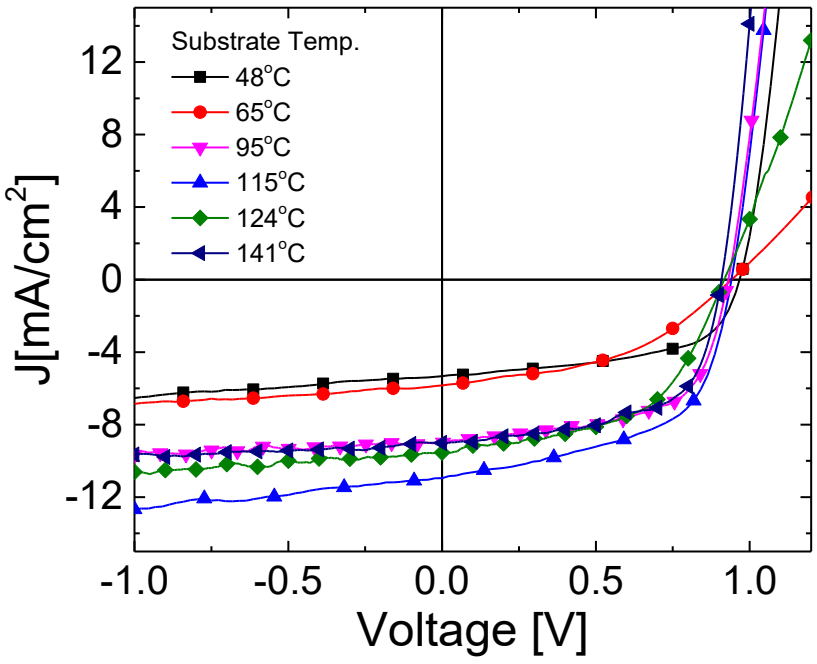

Figure 5.1 a) Device structure of CuSCN:PC$_{70}$BM device. b) J-V characteristics of CuSCN:PC$_{70}$BM device at different substrate temperature before spin-coating process.

Substrate temperature	Jsc [mA/cm²]	Voc [V]	FF [%]	PCE [%]
65 °C	5.5±0.4 (5.9)	0.94±0.02 (0.95)	42±2 (44)	2.5±0.1 (2.5)
115 °C	10.5±0.6 (11)	0.94±0.02 (0.93)	55±4 (56)	4.9±1.1 (5.8)
141 °C	8±1.2 (9)	0.91±0.05 (0.91)	62±2 (61)	4.8±0.2 (5.0)

Table 5.1 Summary table of CuSCN:$PC_{70}BM$ device for different substrate temperatures before spin coating. Averaged values (average of 16 devices, outlier devise are excluded) are shown in the table and the best device is shown in the bracket.

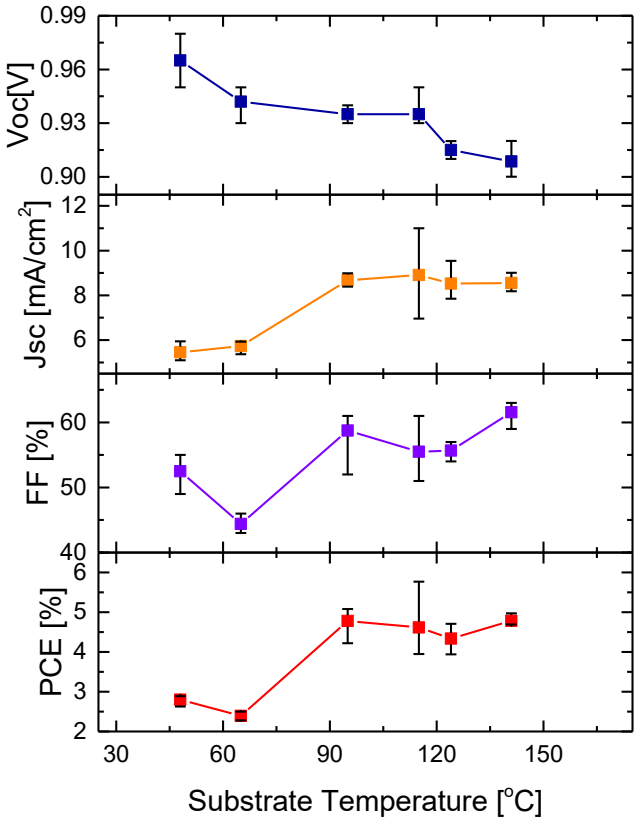

Figure 5.2 Open-circuit voltage, short circuit current, fill factor, and power conversion efficiency of CuSCN:$PC_{70}BM$ device at different substrate temperature before spin-coating. The error bars are obtained by 8 devices in the same substrate.

Next, we attempted to change the composition ratio between CuSCN and $PC_{70}BM$. In our control device, we used the volume ratio 25μL to 75μL (1:3) of CuSCN to $PC_{70}BM$. Figure 5.3 shows the J-V characteristics of CuSCN:$PC_{70}BM$ device at different volume ratio between CuSCN and $PC_{70}BM$, with Table 5.2 showing the parameters of the best device. The values in the brackets show the average values. Interestingly, it appears that the volume ratio of CuSCN to PCBM appears to affect the device performance only weakly within the volume ratios tested, with most of the device parameters changing in consistent manner in relation to the volume ratio. Only the J_{sc} appears to depend weakly on the volume, with ratios of 1:3 and 1:4 giving maximum J_{sc}, and also best device performances, with lower or higher ratios appears to decrease the photocurrent slightly.

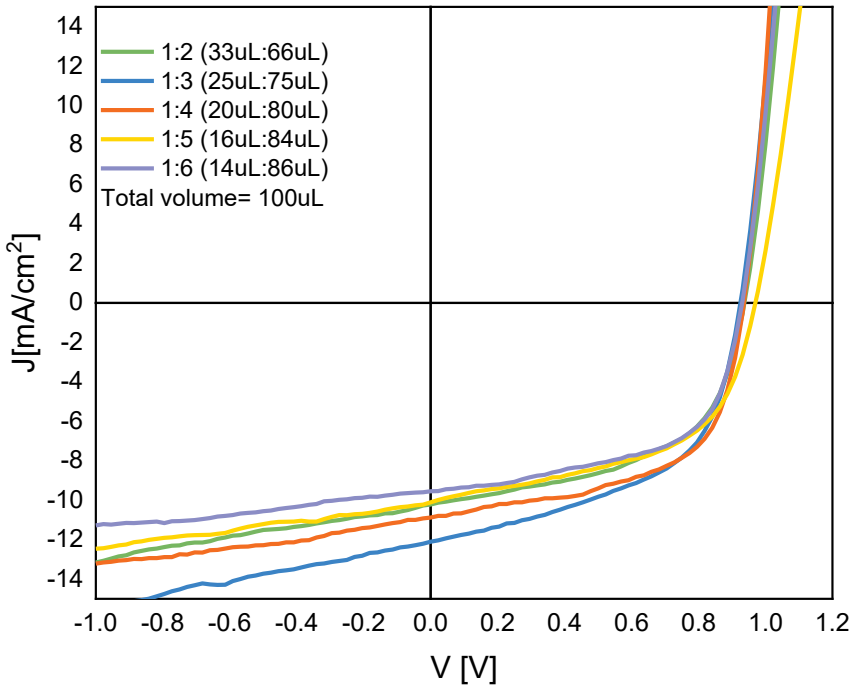

Figure 5.3 *J-V* characteristics of CuSCN:$PC_{70}BM$ at different volume ratio.

CuSCN:$PC_{70}BM$ Volume ratio	J_{sc} [mA/cm²]	V_{oc} [V]	FF [%]	PCE [%]
1:3	11.1±1.1 (12.1)	0.94±0.3 (0.93)	49±4 (52)	5.1±0.8 (5.9)
1:5	9.1±1.3 (10.1)	0.97±0.3 (0.98)	51±4 (53)	4.5±0.7 (5.2)

Table 5.2 Summary table of CuSCN:$PC_{70}BM$ device at different volume ratio. Values are the average of 16 devices. The numbers in the bracket are the value obtained from the best device.

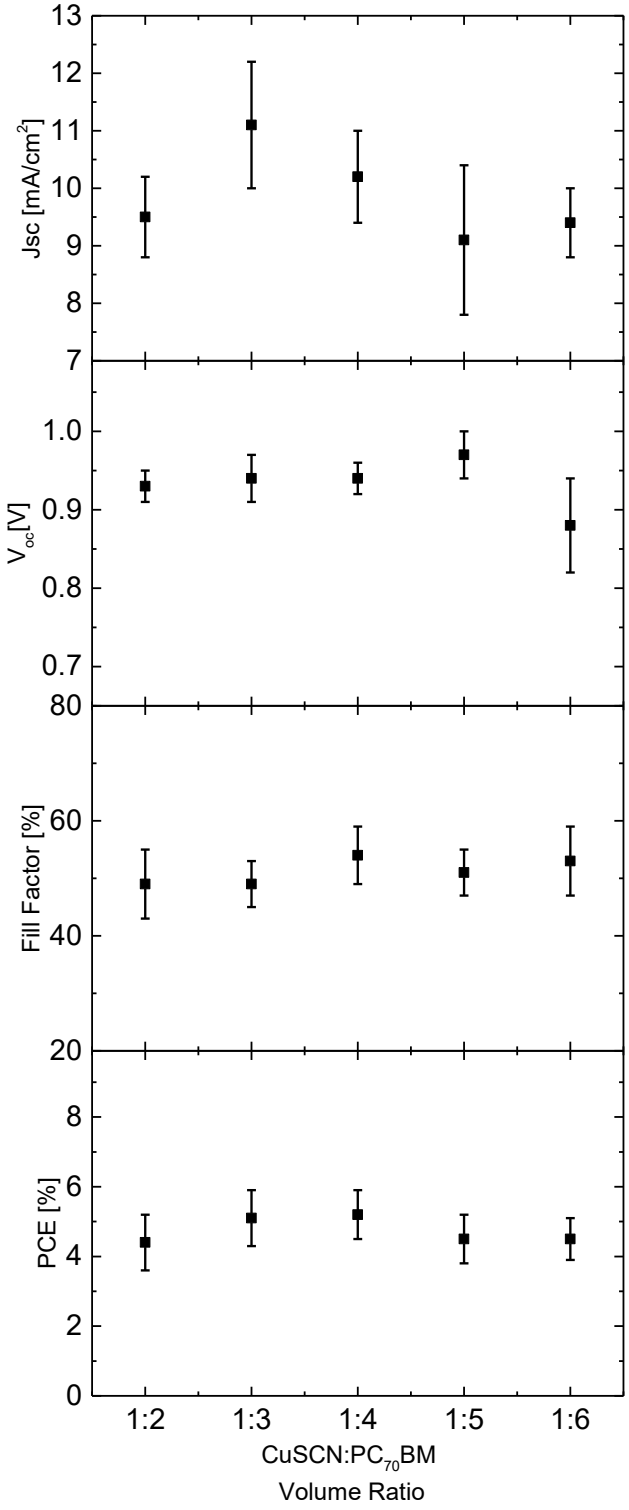

Figure 5.4 *Jsc, Voc, FF,* and *PCE* of CuSCN:PC_{70}BM device at different volume ratio between CuSCN and PC_{70}BM.

The maximum efficiency obtained from these devices was a high 5.9%. Unfortunately, such high device performance appeared to be only possible with a certain batch of $PC_{70}BM$, with others giving lower performance. Figure 5.5 shows a photograph of different batches of $PC_{70}BM$ purchased from SolenneBV, and synthesized at different times. These $PC_{70}BM$ samples were used to fabricate CuSCN:$PC_{70}BM$ devices under the same conditions to evaluate the effect of variations in $PC_{70}BM$ composition on device performance, and the effect of $PC_{70}BM$ degradation on device performance. Figure 5.6 shows the *J-V* characteristics of different batches of $PC_{70}BM$. The oldest batch that was synthesized in 2010 shows only 1% of PCE. The older the $PC_{70}BM$, the more the fill factor and short-circuit current density decrease, showing that the degradation, probably by oxidation, of $PC_{70}BM$ has a severe impact on the CuSCN:$PC_{70}BM$ device (Figure 5.7). Notably, even $PC_{70}BM$ batches synthesized in the same year (2016) showed differences in performance, suggesting that small variations in $PC_{70}BM$ purity could affect NW morphology. These results not only show that the reproducibility of CuSCN:$PC_{70}BM$ device is difficult, but also shows that using low-quality $PC_{70}BM$ affects the device performance significantly.

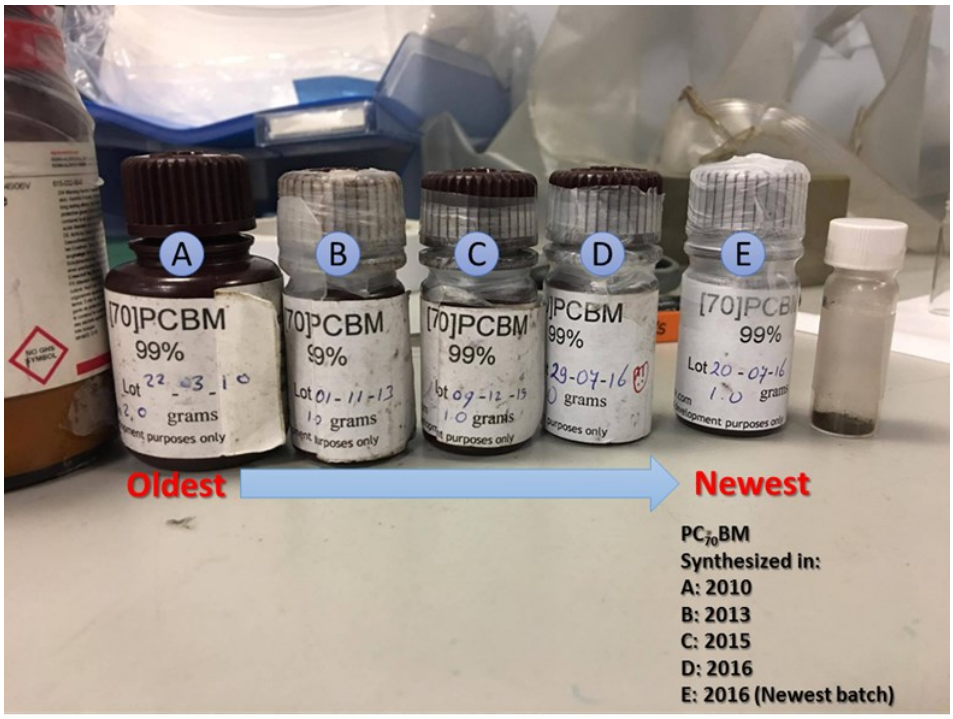

Figure 5.5 Image of $PC_{70}BM$ that was synthesized from A) 2010, B) 2013, C) 2015, D) 2016, E) 2016

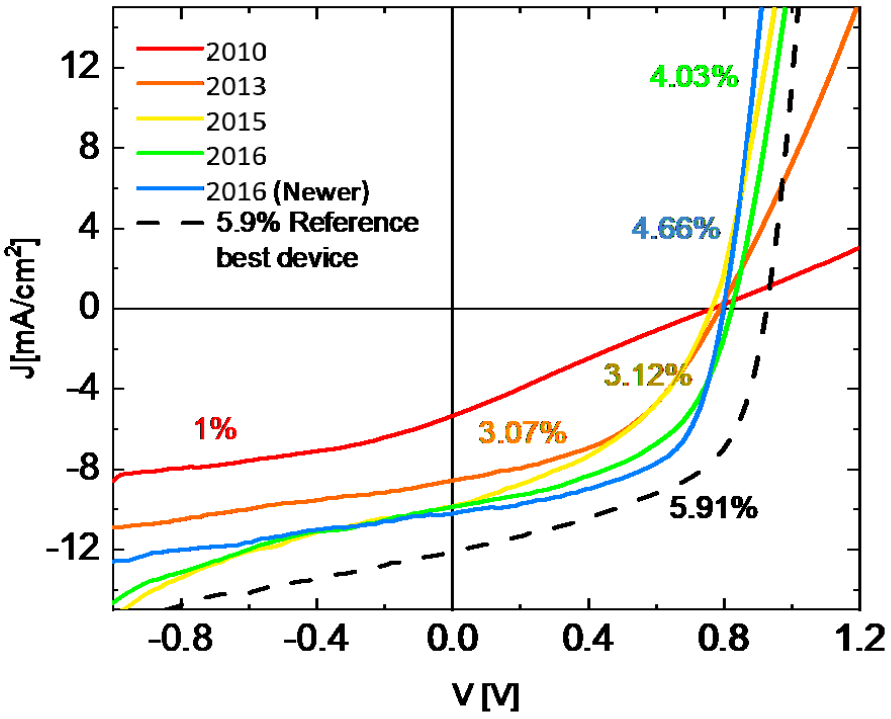

Figure 5.6 *J-V* characteristics of CuSCN:$PC_{70}BM$ devices made from different age of $PC_{70}BM$. The number beside each curve indicate the power conversion efficiency of that device. The 5.9% reference device was also fabricated in 2016.

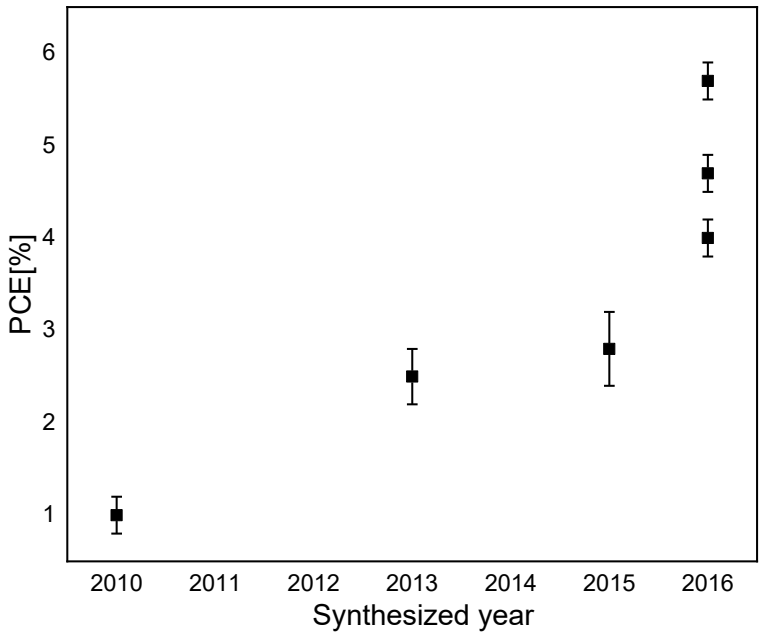

Figure 5.7 Power conversion efficiency of CuSCN:$PC_{70}BM$ device as a function of the year of synthesis of $PC_{70}BM$.

5.2 Depositing interlayer in CuSCN:$PC_{70}BM$ device

After achieving 5.9% power conversion efficiency of the CuSCN:$PC_{70}BM$ device, we then focus on optimizing the formation of CuSCN nanowires, ideally to increase the density of nanowires. Figure 5.8 shows the TEM image of CuSCN:$PC_{70}BM$ device, we have found that the length of CuSCN-NWs has a range from 30nm to 100nm and the nanowires are randomly oriented. Also, CuSCN NWs are formed in the mixed CuSCN:$PC_{70}BM$ layer when the precursor solution is spun on the compact CuSCN layer, and only when this is the case; NWs do not form, for example, if the solution is spin cast on a PEDOT:PSS layer. This suggest that the underlying CuSCN layer is necessary for inducing NW growth, and that its properties might also determine the precise

morphology of the obtained NWs Thus, in this section, we aim to increase the density of CuSCN NWs by using interlayers on top of the CuSCN to induce variations in NW growth

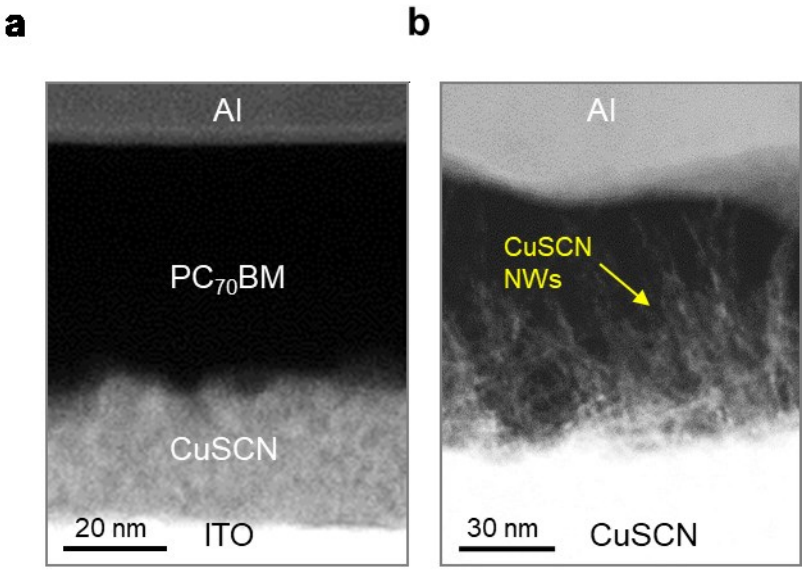

Figure 5.8TEM images of a) planar CuSCN/$PC_{70}BM$ device and b) mixed CuSCN:$PC_{70}BM$ device. (Images taken by Dr. Claire Burgess)

We tried to deposit three different interlayers between the compact CuSCN layer and the CuSCN:$PC_{70}BM$ layer. 1) An additional interlayer of pristine CuSCN is deposited between the compact CuSCN layer and CuSCN:$PC_{70}BM$ layer. 2) An extra layer of CuSCN:$PC_{70}BM$ layer. In this layer, the volume ratio of 9:1 between CuSCN:$PC_{70}BM$ was used. 3) An extra layer of CuSCN:$PC_{70}BM$ layer with the volume ratio of 4:1. The device structure and the *J-V* characteristics of the devices are shown in Figure 5.9 and Figure 5.10, respectively. Although the power conversion efficiency is slightly lower than the previous control device in Chapter 4, the trend indicates that depositing any CuSCN interlayer between improves the device performance. As mentioned before, we could compare the device performance within the same batch of

device. The result shows that we could observe an overall increase of J_{sc} from 7.8 mA/cm^2 to 9.1 mA/cm^2 and a significant increase in power conversion efficiency as shown in Table 5.3. Such improvement suggests that interlayers could possibly change the microstructure of CuSCN:$PC_{70}BM$ NWs, causing the improvement of J_{sc}. Before discussing the change in the nanostructure, we will discuss further improvement of CuSCN:$PC_{70}BM$ device by depositing similar layers using different processing methods.

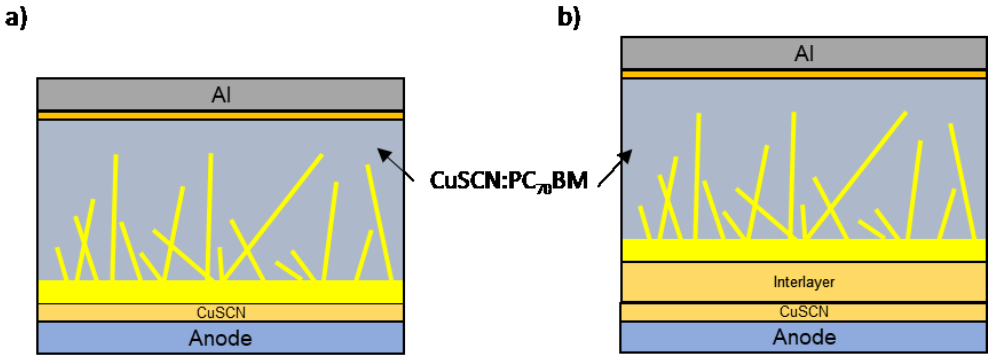

Figure 5.9 Device structure of CuSCN:$PC_{70}BM$ a) without and b) with interlayer.

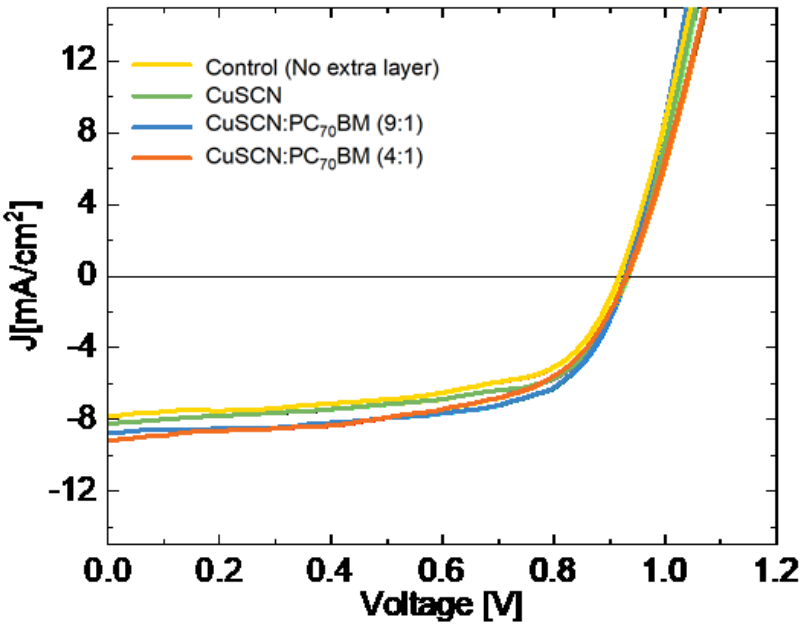

Figure 5.10 *J-V* characteristics of CuSCN:$PC_{70}BM$ with different composition of extra layer.

interlayer	J_{sc} [mA/cm²]	V_{oc} [V]	FF [%]	PCE [%]
CuSCN	8.2±0.2 (8.2)	0.93±0.03 (0.93)	61±3 (62)	4.6±0.1 (4.7)
CuSCN:$PC_{70}BM$ (4:1)	8.9±0.2 (9.1)	0.93±0.02 (0.93)	56±5 (56)	4.6±0.2 (4.8)

Table 5.3 Summary table of CuSCN:$PC_{70}BM$ with different extra layer. Average values of 16 devices are shown in the table. The performance of best device is shown in the bracket.

Depositing a CuSCN-rich interlayer was shown to improve the short-circuit current density in the last section. We then utilized this result to further optimize the device performance. An interlayer of CuSCN:$PC_{70}BM$ with volume ratio of 9:1 was then used, in order to encourage a different NW growth. We investigated the effect of depositing one of these layers at similar at different processing conditions and the result is shown in Figure 5.11. Firstly, spin casting this layer at either 2000 rpm appears to increase the performance of the cell compared to the control with no such interlayer. The average short circuit current increases from 8.3 mA/cm^2 to 9.5-9.7 mA/cm^2, whilst both open-circuit voltage and fill factor show no significant improvement. The power conversion efficiency is improved from 4.23% to more than 4.8%. Secondly, if the interlayer is first cast on the compact CuSCN layer and then there is a delay for 1 minute before the spin coating process (marked as "soak" in Figure 5.11), the effect is still similar, and that the power conversion efficiency is still 4.8%. It shows that the longer contact time between the interlayer and the compact CuSCN layer does not significantly affect the formation of CuSCN-NWs and the device performance. Interestingly, if the interlayer was spun while the substrate is already under rotational motion (dynamic spin-coating), the average short circuit current density increased to 10.4mA/cm^2. In particular, the best device in this batch shows more than 12 mA/cm^2, yielding the power conversion efficiency to be 5.72%. The best device in this sample has a PCE of 6.79%. We also tried to deposit double interlayers. The average J_{sc} further increased to 9.9 mA/cm^2. It therefore appears that it is possible to change the nature of NW growth using the interlayer. It is worth noting that the reproducibility of the device is very poor due to multiple reasons. 1) The formation of CuSCN nanowires inside PCBM layer is hugely affected by substrate temperature. Ambient temperature and the time to transfer samples

from hotplate to spin-coater chuck may vary and cause uncertainty in substrate temperature, which causes inconsistency of the formation of CuSCN NWs. 2) The orientation and the length of CuSCN NWs are believed to be random. Ideally, NWs oriented perpendicular to the substrates and the length should cover the $PC_{70}BM$ bulk layer to achieve maximum charge dissociation efficiency. In practice, it is still unclear how to control the orientation and the length of such CuSCN NWs, which may cause batch-to-batch variation.

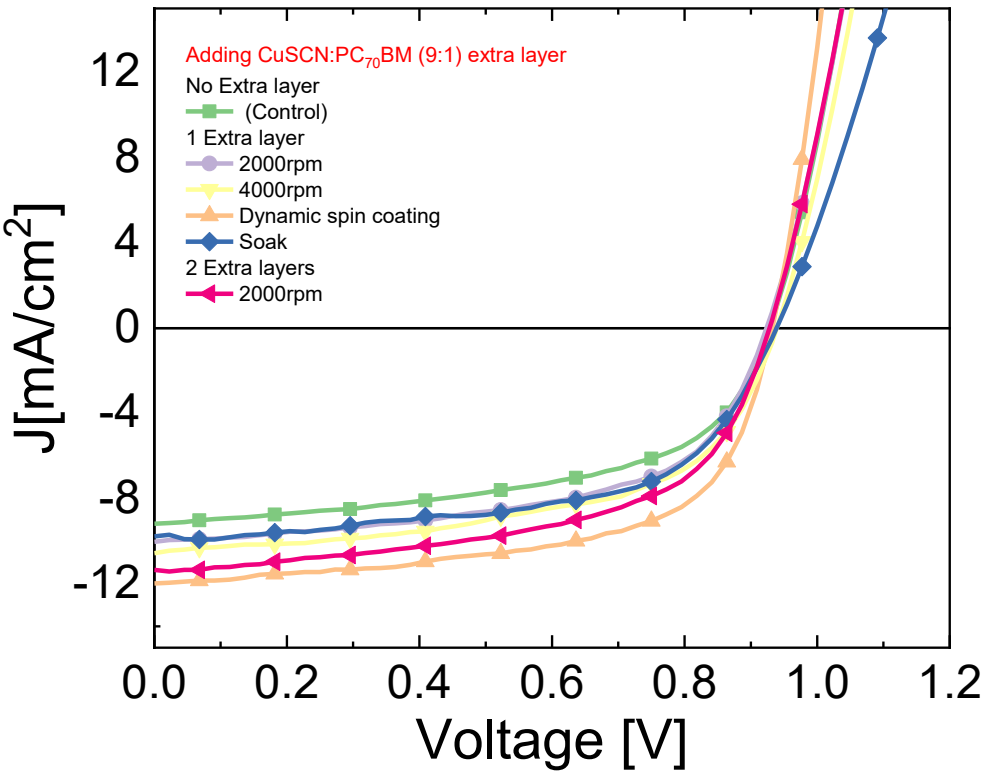

Figure 5.11 J-V characteristics of CuSCN:$PC_{70}BM$ device with 9:1 volume ratio of CuSCN:$PC_{70}BM$ as interlayer, processed under different conditions.

Interlayer	Jsc [mA/cm²]	Voc [V]	FF[%]	PCE [%]
Control				
1 layer (2000rpm)	9.0±0.5 (9.5)	0.93±0.1 (0.92)	53±2 (56)	4.5±0.4 (4.9)
1 layer (4000rpm)				
1 layer (Soak)	9.1±0.3 (9.3)	0.92±0.1 (0.93)	54±3 (57)	4.2±0.2 (4.9)
1 layer (Dynamic)				
2 layers (2000rpm)	9.4±0.5 (9.9)	0.92±0.1 (0.93)	55±5 (59)	4.7±0.7 (5.4)

Table 5.4 Summary table of CuSCN:$PC_{70}BM$ device with 9:1 volume ratio of CuSCN:$PC_{70}BM$ as interlayer, processed under different conditions. Average values are shown in the table from 16 devices. The best device is shown in the bracket.

5.3 Microstructure analysis of CuSCN:$PC_{70}BM$ device.

To understand the origin of the effect of interlayers (seed layer) between compact CuSCN layer and the CuSCN:$PC_{70}BM$ layer, we have done atomic force microscope analysis (AFM), scanning electron microscope (SEM), and high-resolution transmission electron microscopy (TEM) images with the 6.79% best device. Figure 5.12a and Figure 5.12b show the SEM image of the CuSCN:$PC_{70}BM$ device taken from the aluminium electrode with and without the CuSCN:$PC_{70}BM$ in 9:1 ratio. Compared to the device without any seed layer, multiple oval-shaped defects are observed from its surface. These defects have a radius of ~100nm. On the other hand, on the aluminium electrode surface, pinhole-like defects of similar size to the oval defects are observed. The density of pinholes is similar to the oval defects observed in the $PC_{70}BM$ layer. This suggests that the oval-shaped defects caused inhomogeneous electrode surface. We then took another set of SEM images on top of CuSCN:$PC_{70}BM$ layer Figure 5.12c and 5.12d. Similar

oval-shaped defects are observed on CuSCN:$PC_{70}BM$ surface with seed layer. A homogeneous film was observed with the device without seed layer, which confirms that the defects are formed inside the CuSCN:$PC_{70}BM$ layer. The radius of the defect is around 100nm, which is similar to the defect we observed on the aluminium surface using AFM. The separation between defects is around 500nm to 1000nm and the defects are hollow. Furthermore, we also scanned the surface of the electrode of double seed layers and compared them with single seed layer as shown in Figure 5.13. Interestingly, the number of defects in 14×14 μm area for one single seed layer and double seed layers are found to be 188 and 193, respectively. This result suggests that defects are formed when the first seed layer is deposited. Spin coating more seed layers do not increase the number of defects significantly.

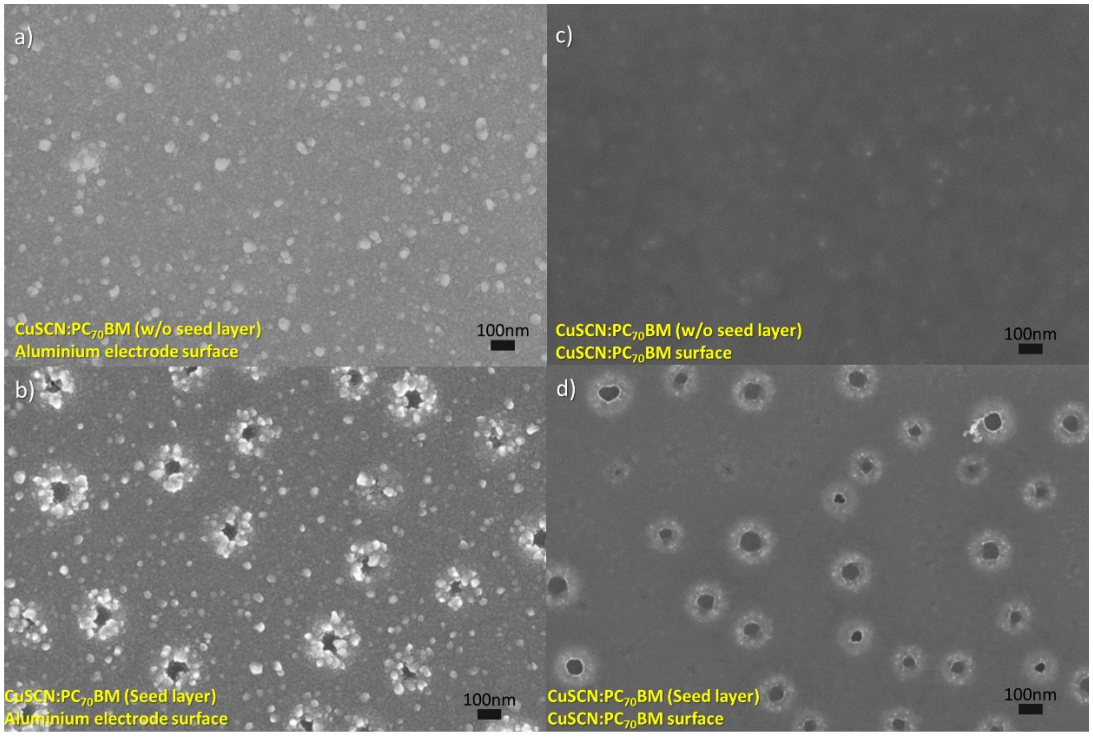

Figure 5.12 SEM images of CuSCN:$PC_{70}BM$ device with or without CuSCN:$PC_{70}BM$ 9:1 volume ratio seed layer. a) Without the seed layer and SEM was scanned on the aluminium electrode. b) With the seed layer when the SEM was scanned on the aluminium electrode.

Radius of ~100nm size of defects is observed. c) Without the seed layer and SEM was scanned on the CuSCN:$PC_{70}BM$ layer. d) With the seed layer when the SEM was scanned on the CuSCN:$PC_{70}BM$ layer. Similar defects are observed in this scan, suggesting the pin-hole defects were formed in the CuSCN:$PC_{70}BM$ layer. (Images taken by Dr. Claire Burgess)

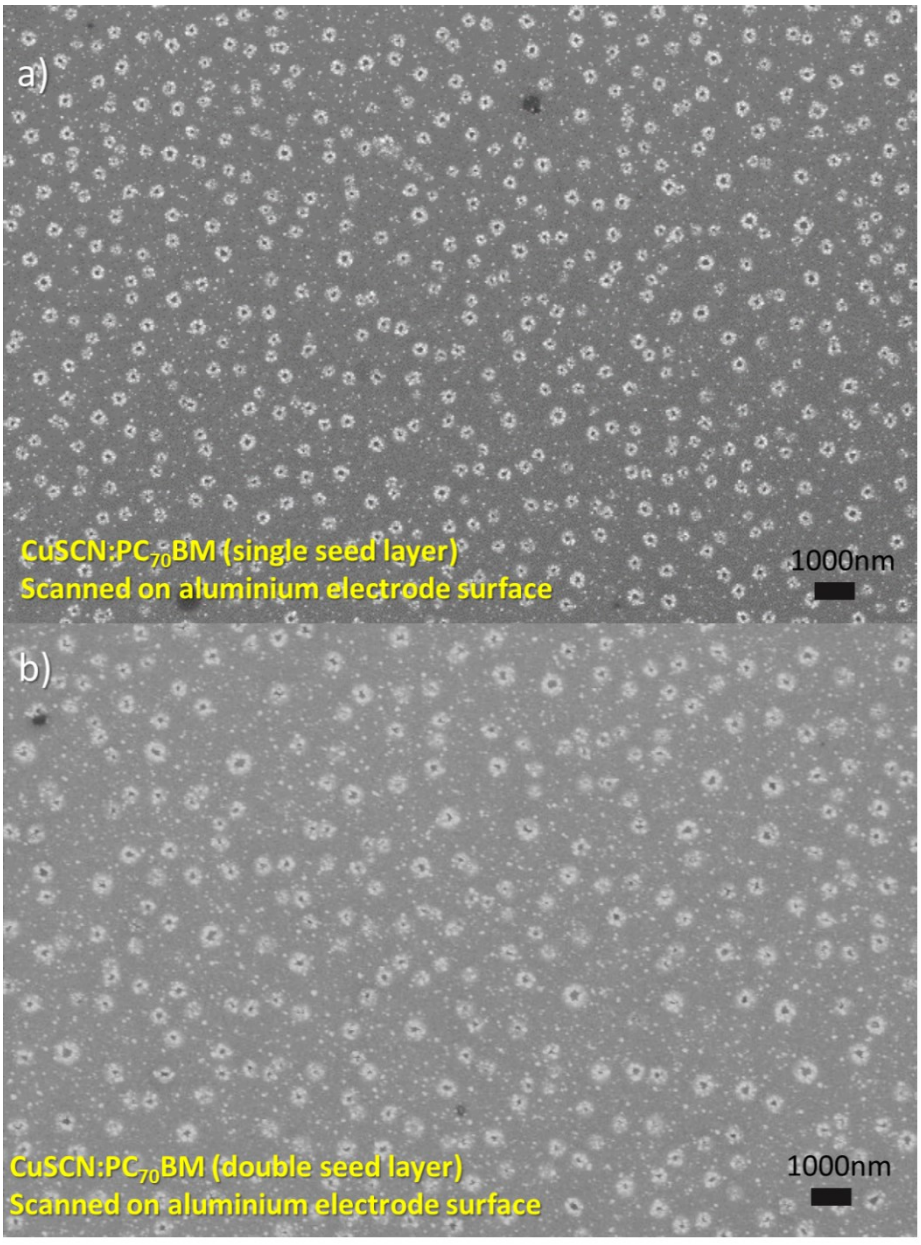

Figure 5.13 SEM images of aluminium electrode of CuSCN:$PC_{70}BM$ device with 1 or 2 seed layers of CuSCN:$PC_{70}BM$. a) One CuSCN:$PC_{70}BM$ seed layer was spun b) two CuSCN:$PC_{70}BM$ seed layer was spun (Images taken by Dr. Claire Burgess)

To further confirm the nature of oval-shaped defects inside the $PC_{70}BM$ layer, we

took cross-section TEM images of the CuSCN:$PC_{70}BM$ device as shown in Figure 5.14. When the seed layer is deposited on the pristine CuSCN layer, the CuSCN film becomes non-uniform. We observed two craters in the CuSCN:$PC_{70}BM$ layer, which are marked A and B in Figure 5.13. Crater A is shallower compared to crater B, but the size of B is bigger. In crater B, the compact CuSCN layer is nearly being dissolved completely, which may cause a direct contact of CuSCN:$PC_{70}BM$ to the anode. In region C, the CuSCN thickness is higher than other regions in Figure 5.13. It is possible that region C is at the edge of a crater, which pushes CuSCN outwards from the crater center, causing an increased CuSCN thickness.

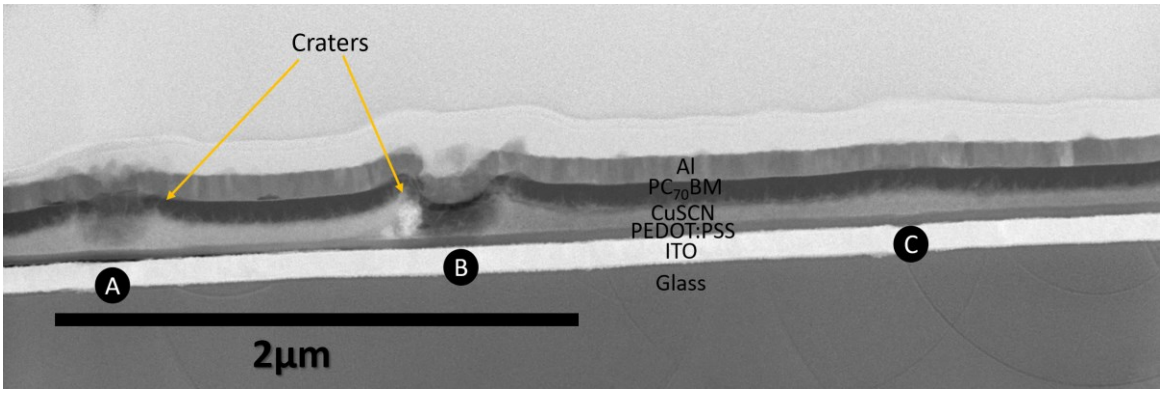

Figure 5.14 Cross-sectional TEM image of CuSCN:$PC_{70}BM$ layer with one layer of CuSCN:$PC_{70}BM$ seed layer is deposited. (Images taken by Dr. Claire Burgess)

To understand the composition of the craters, we also performed EDX elemental mapping on the crater. Figure 5.15 shows the cross-section image of a 200nm diameter size crater on a single seed-layer sample. These images clearly show the aluminium from the electrode and indium from ITO. The carbon mapping image shows that carbon atoms exist in both $PC_{70}BM$ and CuSCN layer. The density of carbon is significantly higher in $PC_{70}BM$ layer than CuSCN layer. Inside the crater, we can see both carbon and sulfur atoms. That means CuSCN, and possibly CuSCN NWs are present inside the crater. By taking an enlarged image at the crater as shown in Figure 5.16. We can see that there are

long CuSCN NWs emerging from inside. Both the density and length of the NWs inside the crater is much higher than other regions, suggesting that such crater an act as a charge-generating site where photogenerated charges can be generated and extracted effectively, leading to higher J_{sc} from the device. We also observed other craters and found that not all craters are filled with high density of CuSCN-NWs. The image in Figure 5.17 is another EDX measurement of a crater but with lower CuSCN:$PC_{70}BM$ NW density. The content of sulphur inside the crater is clearly lower compared to the CuSCN-NW rich crater in Figure 5.15. This result suggests that this crater could be a region dominated by with $PC_{70}BM$ instead of a high-density CuSCN-NW region.

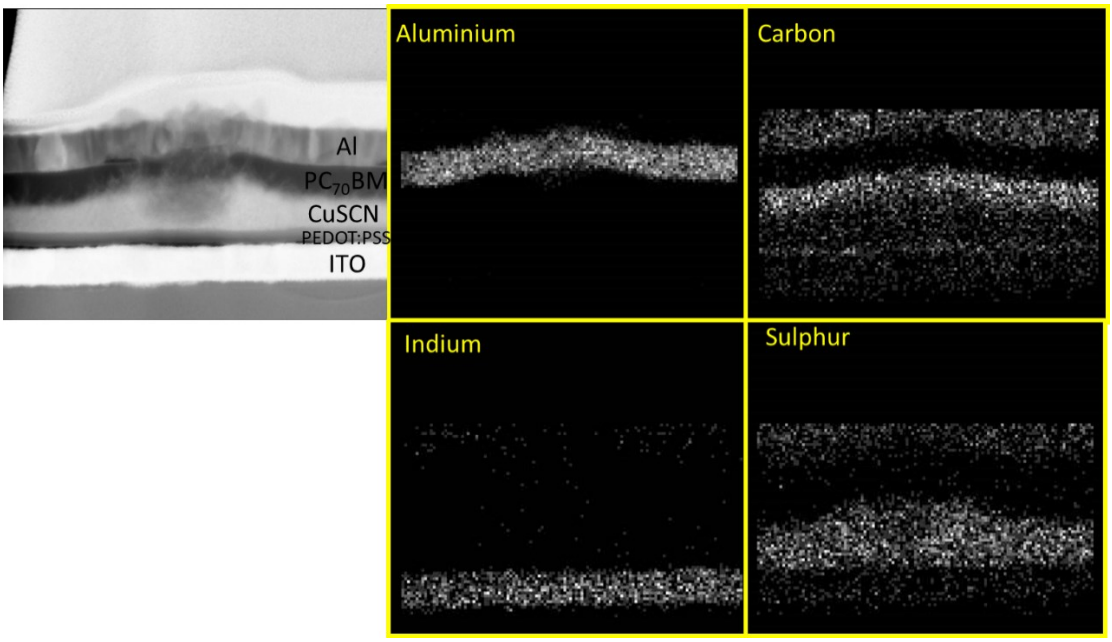

Figure 5.15 Cross-sectional TEM image (top left) and EDX measurement of CuSCN:$PC_{70}BM$ device with the seed layer (right). Brightness shows the concentration of each certain element. Elemental mapping of at the same region of aluminium, carbon, indium, and sulphur are shown. It shows that sulphur is found inside the crater, suggesting there is CuSCN. (Images taken by Dr. Claire Burgess)

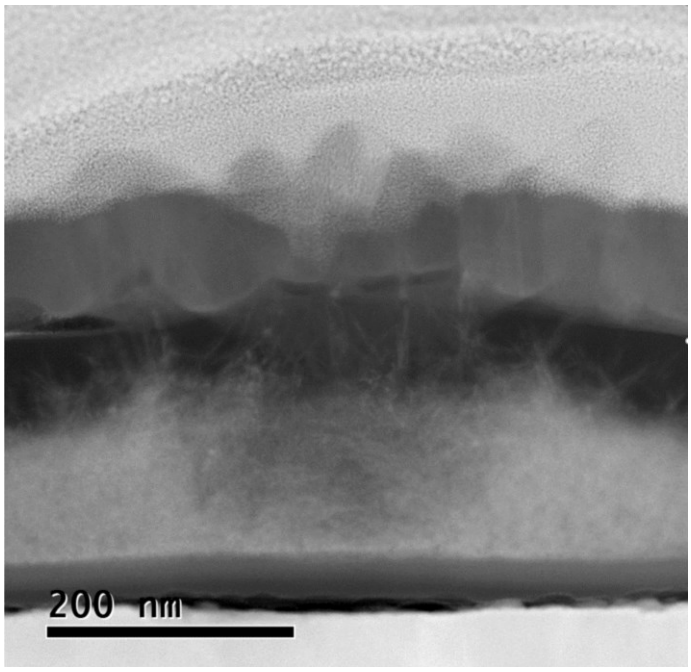

Figure 5.16 Enlarged image of CuSCN:$PC_{70}BM$ with seed layer. High density of CuSCN NWs can clearly be seen. (Images taken by Dr. Claire Burgess)

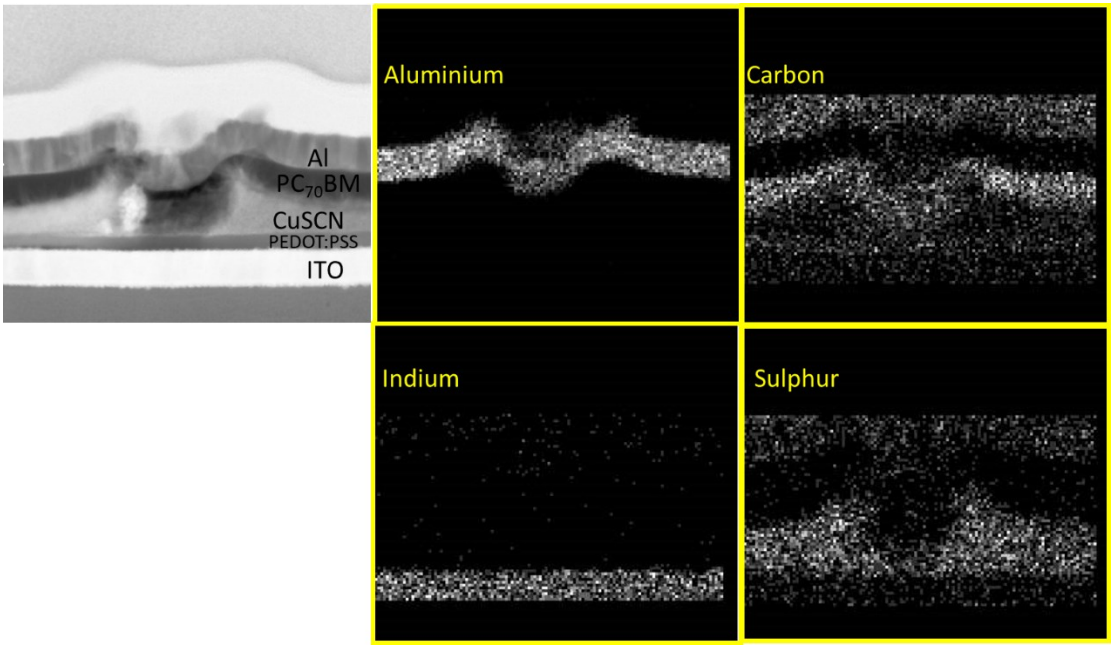

Figure 5.17 Cross-sectional TEM image (top left) and EDX measurement of CuSCN:$PC_{70}BM$ device with the seed layer. Elemental mapping of aluminium, carbon, indium, and Sulphur are shown. This time the crater contains relatively lower CuSCN NW density, than in Figure 5.15, suggesting that craters do not always have high density

CuSCN-NWs. (Images taken by Dr. Claire Burgess)

Also, we have investigated the effect of spin-coating multiple seed layers. As shown in Figure 5.13, having more seed layers does not increase the number of craters significantly, which matches our result in Figure 5.11 that doubling the seed layer does not improve the device performance. To investigate the formation of CuSCN NWs in single and double seed layers, another set of cross-sectional TEM images is taken and shown in Figure 5.18. One may expect that the thickness would increase if two seed layers were deposited. However, the image shows a similar thickness in both devices. No significant difference between one seed layer and two seed layers are found.

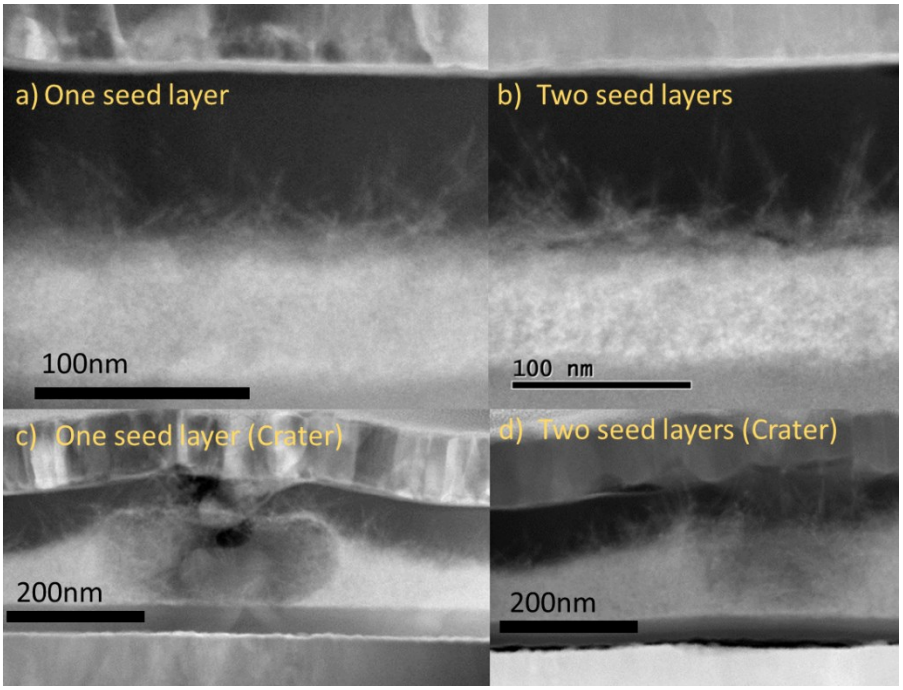

Figure 5.18 Cross-sectional TEM image of CuSCN:$PC_{70}BM$ layer. a) Image taken in a single seed layer device. b) Image taken in a double seed layer device. c)Image of a crater with single seed layer. d) Image of a crater with double seed layers. (Images taken by Dr. Claire Burgess)

To conclude, we have found that spin-coating a seed layer of 9:1

CuSCN:$PC_{70}BM$ on top of pristine CuSCN layer causes the formation of CuSCN NW filled craters. Such craters may re-dissolve the underneath compact CuSCN layer. The density of CuSCN NWs inside these craters could vary. The formation mechanism of the craters and the density of CuSCN NWs inside it is still unclear. We believe that such craters could improve that charge extraction efficiency due to the high density of CuSCN NW. However, due to the size of the crater (~100nm in diameter), similar size of pinholes are found on the aluminum electrode. The best device we have fabricated has a power conversion efficiency of 6.79% but the average performance on the same substrate is 5.72%. The poor reproducibility of such device makes it difficult to perform a more systematic analysis.

5.4 Adding aluminum, gold, and silver nanoparticles into CuSCN:$PC_{70}BM$ layer

In our CuSCN:$PC_{70}BM$ device, the limitation to device performance is primarily due to the low absorption coefficient and high band gap of $PC_{70}BM$, which limits the maximum achievable *Jsc*. In order to improve photon absorption inside the photoactive layer, increasing film thickness is the most straightforward way as suggested by the Beer-Lambert law. This, however, tends to negatively impact on charge-extraction within the device, leading to decreased FFs, and is also challenging in practice due to difficulties in obtaining more concentrated PCBM solutions that already used. A way to circumvent this problem, therefore, is to use metallic nanoparticles, which have been found to be an alternative way to improve light absorption by utilizing the localized surface plasmonic resonance effect to induce light trapping.[1–7]

There are generally three different approaches for metallic NPs to create light

trapping effect to improve the light-absorbing property of the photoactive layer. First, when metallic particles at the surface of the photoactive layer, the incoming photons are scattered and are trapped inside it due to the large scattering angle.[8–11] It is also found that such scattering effect is very sensitive to shapes and sizes.[12] Secondly, metallic particles inside the semiconductor could cause excitation of localized surface plasmon in the nanoparticles. Such excited particles could also lead to enhanced electron-hole pair generation in the semiconductor because the light absorption of the semiconductor surrounding the NPs is improved.[13–20] Finally, if metallic nanoparticles are formed at the interface between the electrode and the photoactive layer, it could couple sunlight and cause a surface plasmon polariton (SPP) to propagate in the plane of the device. The lateral distance is significantly higher than the film thickness so that the optical path of light could increase.[21–24]

In this section, we focus on aluminum and silver nanoparticles of size 10nm. These nanoparticles were mixed with the CuSCN:$PC_{70}BM$ solution before spin coating at different volume ratios. Figure 5.19 and Figure 5.20 show the absorption coefficient of the CuSCN:$PC_{70}BM$ with the effect of aluminium and silver nanoparticles, respectively. In the measurement we have assumed there is no light reflection from the surface of the film. The results show that the absorption coefficient increases when aluminium nanoparticles are added to the CuSCN:$PC_{70}BM$ solution. Such light absorption improvement is maximum when the volume ratio of aluminium nanoparticles at 10%. On the other hand, the improvement of light absorption with silver nanoparticles is not as significant as with aluminium.

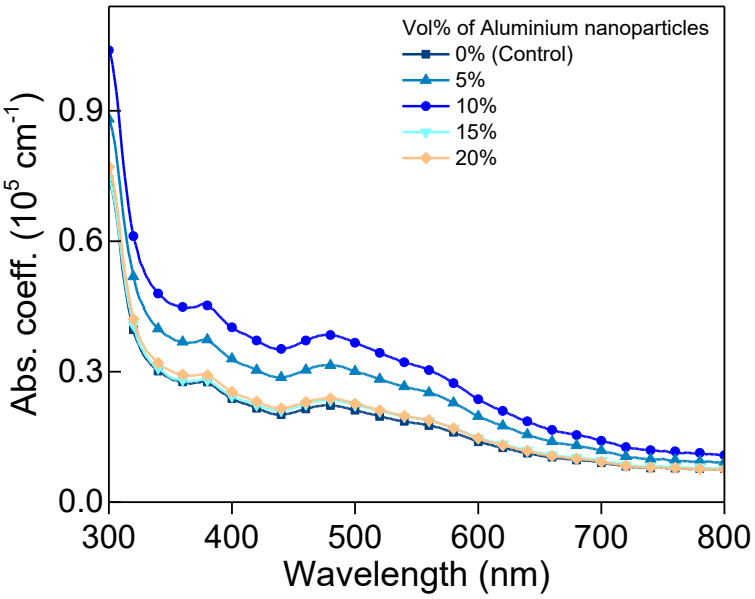

Figure 5.19 Absorption coefficient of CuSCN:$PC_{70}BM$ layer at different aluminium nanoparticles volume ratio.

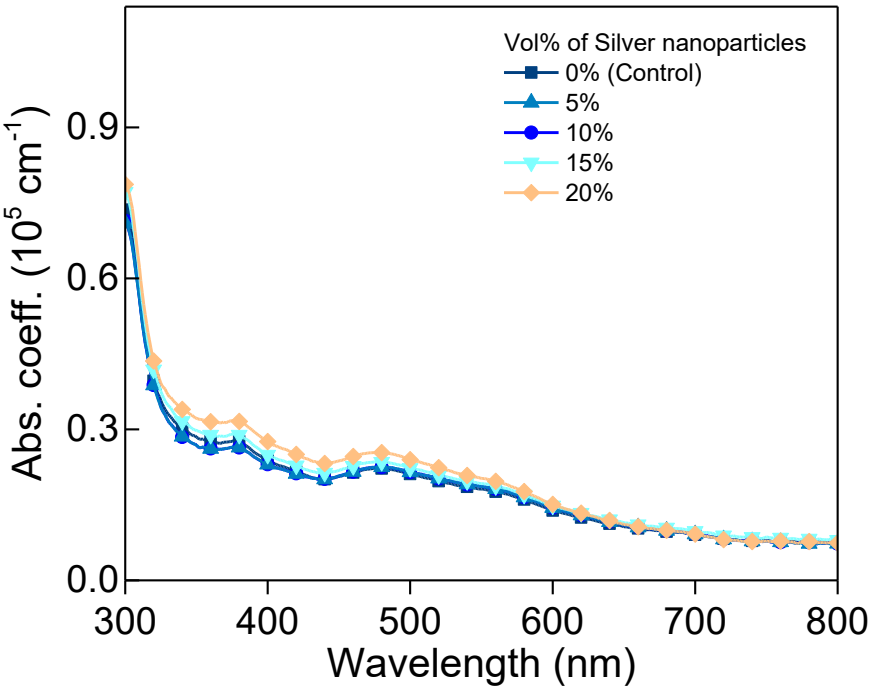

Figure 5.20 Absorption coefficient of CuSCN:$PC_{70}BM$ layer at different silver nanoparticles volume ratio.

Figure 5.21 shows the J-V characteristics of CuSCN:$PC_{70}BM$ device with different volume ratios of aluminum nanoparticles were mixed in the CuSCN:$PC_{70}BM$ solution. The average device performance is shown in Table 5.5. The result shows that the average short circuit current increased from 7.7mA/cm^2 to 9mA/cm^2 when the doping concentration is at 10%. The average open-circuit voltage and fill factor lie around 0.9V and 60%, which are similar to our previous results. Although the device performance is not as high as previous devices due to poor reproducibility, the improvement from a maximum of 4.4% to 5.4% of PCE is promising. On the other hand, the result for silver nanoparticles shows that it does not improve the device performance as shown in Figure 5.22 and Table 5.6. This is probably because the absorption coefficient does not improve the absorption coefficient. Also, adding excess nanoparticles will change the composition of the CuSCN:$PC_{70}BM$ layer, leading to changes in the NW microstructure, which may negatively impact charge generation or extraction

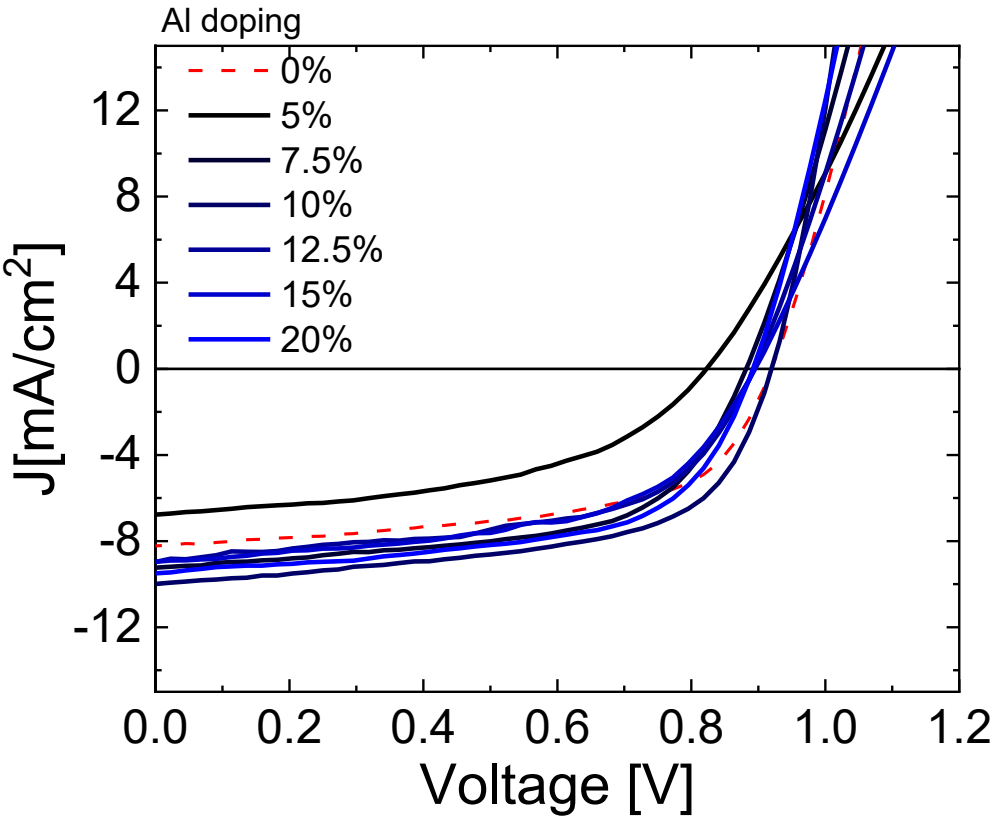

Figure 5.21 J-V characteristics of CuSCN:$PC_{70}BM$ layer with different volume ratio of aluminium nanoparticles.

Aluminium	J_{sc} [mA/cm²]	V_{oc} [V]	FF [%]	PCE [%]
5%	6.3±0.2 (6.5)	0.81±0.02 (0.83)	45±2 (47)	2.2±0.4 (2.6)
10%	8.5±0.5 (9.0)	0.91±0.01 (0.92)	57±3 (60)	5.0±0.4 (5.4)
15%	8.0±0.4 (8.4)	0.84±0.05 (0.89)	54±1 (54)	3.5±0.6 (4.1)

Table 5.5 Summary table of CuSCN:$PC_{70}BM$ device with aluminium nanoparticles in CuSCN:$PC_{70}BM$ device. Average values are shown in the table from 16 devices. The best device performance is shown in bracket

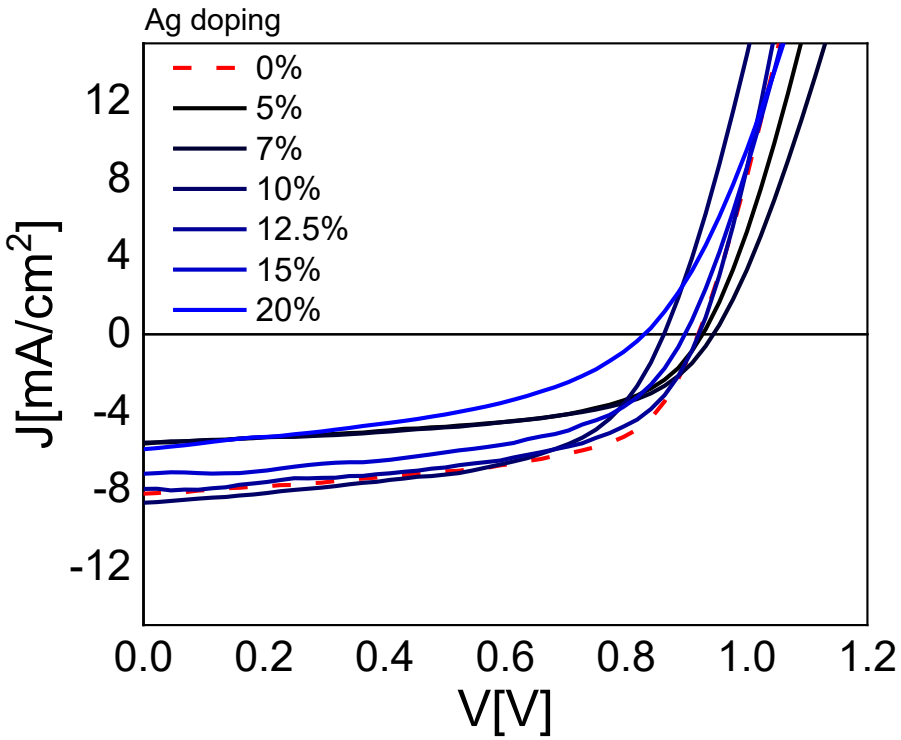

Figure 5.22 *J-V* characteristics of CuSCN:$PC_{70}BM$ layer with different volume ratio of silver nanoparticles.

Aluminium	J_{sc} [mA/cm²]	V_{oc} [V]	FF [%]	PCE [%]
5%	5.5±0.2 (5.6)	0.90±0.05 (0.93)	54±2 (55)	2.4±0.4 (2.8)
10%	7.7±0.5 (7.9)	0.82±0.06 (0.85)	54±3 (54)	3.2±0.4 (3.6)
15%	7.0±0.3 (7.2)	0.84±0.05 (0.89)	51±1 (51)	2.7±0.6 (3.3)

Table 5.6 Summary table of CuSCN:$PC_{70}BM$ device with silver nanoparticles in CuSCN:$PC_{70}BM$ device.

5.5 Conclusion

By optimizing the formation of CuSCN:$PC_{70}BM$ layer, we have found that the CuSCN:$PC_{70}BM$ device works best when the substrate is heated to 115ºC right before spin-coating. The processing condition is highly sensitive as the device has high variation even within the same batch of devices. The change in substrate temperature causes the increase of short-circuit of the device, which we believe that is originated from the formation of CuSCN NWs. The performance of CuSCN:$PC_{70}BM$ device depends strongly on the purity of $PC_{70}BM$. Degradation of $PC_{70}BM$ causes the device to perform poorly.

We then spin-coated multiple CuSCN rich CuSCN:$PC_{70}BM$ layer to help the growth of CuSCN NWs. Craters were formed when CuSCN-rich CuSCN:$PC_{70}BM$ (9:1) interlayer (seed layer) is spun between compact CuSCN and the mixed CuSCN:$PC_{70}BM$ layer (1:4 volume ratio). In some craters, CuSCN-NW is observed to be denser, which acts as light absorption site, causing the improvement of the device. Finally, aluminum and silver nanoparticles were added to mixed CuSCN:$PC_{70}BM$ device (without seed layer). The device with aluminum nanoparticles has a significant improvement in short-circuit current as the absorption coefficient of CuSCN:$PC_{70}BM$ layer has increased.

Reference

[1] H. A.Atwater, A.Polman, *Nat. Publ. Gr.* **2010**, *9*, 205.

[2] L.Lu, Z.Luo, T.Xu, L.Yu, **2012**.

[3] E.Stratakis, E.Kymakis, *Mater. Today* **2013**, *16*, 133.

[4] Q.Gan, F. J.Bartoli, Z. H.Kafafi, *Adv. Mater.* **2013**, *25*, 2385.

[5] K.Kim, D. L.Carroll, *Appl. Phys. Lett.* **2005**, *87*, 083506.

[6] H.IlPark, S.Lee, J. M.Lee, S. A.Nam, T.Jeon, S. W.Han, S. O.Kim, *ACS Nano* **2014**, *8*, 10305.

[7] G. D.Spyropoulos, M.Stylianakis, E.Stratakis, E.Kymakis, *Photonics Nanostructures - Fundam. Appl.* **2011**, *9*, 184.

[8] F. J.Beck, A.Polman, K. R.Catchpole, *J. Appl. Phys.* **2009**, *105*, 1.

[9] S. H.Lim, W.Mar, P.Matheu, D.Derkacs, E. T.Yu, *J. Appl. Phys.* **2007**, *101*,2733649.

[10] S.Mokkapati, F. J.Beck, A.Polman, K. R.Catchpole, *Appl. Phys. Lett.* **2009**, *95*, 3200948.

[11] A. W.Powell, M. B.Wincott, A. A. R.Watt, H. E.Assender, J. M.Smith, *J. Appl. Phys.* **2013**, *113*, 184311

[12] A.Ciesielski, K. M.Czajkowski, D.Switlik, *Sol. Energy* **2019**, *184*, 477.

[13] R. B.Konda, R.Mundle, H.Mustafa, O.Bamiduro, A. K.Pradhan, U. N.Roy, Y.Cui, A.Burger, *Appl. Phys. Lett.* **2007**, *91*, 191111.

[14] N. C.Lindquist, W. A.Luhman, R. J.Holmes, S. H.Oh, *Conf. Proc. - Lasers Electro-Optics Soc. Annu. Meet.* **2008**, *123308*, 413.

[15] A. J.Morfa, K. L.Rowlen, T. H.Reilly, M. J.Romero, J.Van DeLagemaat, *Appl. Phys. Lett.* **2008**, *92*, 4.

[16] B. P.Rand, P.Peumans, S. R.Forrest, *J. Appl. Phys.* **2004**, *96*, 7519.

[17] M.Westphalen, U.Kreibig, J.Rostalski, H.Lüth, D.Meissner, *Sol. Energy Mater. Sol. Cells* **2000**, *61*, 97.

[18] C.Hägglund, M.Zäch, B.Kasemo, *Appl. Phys. Lett.* **2008**, *92*, 2830817.

[19] T.Kume, S.Hayashi, H.Ohkuma, K.Yamamoto, *Jpn. J. Appl. Phys.* **1995**, *34*, 6448.

[20] S. S.Kim, S. I.Na, J.Jo, D. Y.Kim, Y. C.Nah, *Appl. Phys. Lett.* **2008**, *93*, 98.

[21] J. K.Mapel, M.Singh, M. A.Baldo, K.Celebi, *Appl. Phys. Lett.* **2007**, *90*, 2005.

[22] K.Tvingstedt, N. K.Persson, O.Inganäs, A.Rahachou, I.V.Zozoulenko, *Appl. Phys. Lett.* **2007**, *91*, 8.

[23] F. J.Haug, T.Söderström, O.Cubero, V.Terrazzoni-Daudrix, C.Ballif, *J. Appl. Phys.* **2008**, *104*, 2981194.

[24] T. D.Heidel, J. K.Mapel, M.Singh, K.Celebi, M. A.Baldo, *Appl. Phys. Lett.* **2007**, *91*, 89.

Chapter 6. CuSCN:$PC_{70}BM$ thin film transistors and phototransistors

In the last chapter, I highlighted the importance of CuSCN NWs in the $PC_{70}BM$ active layer, to significantly improve the solar cell performance. In particular the fill factor of NW based devices improved drastically over the bilayer ones, which may suggest an improvement in the charge mobility through the nanowire-PCBM matrix. In this chapter, I investigate this improvement further through the fabrication and characterization of the charge transport properties of CuSCN NWs through thin-film transistors and phototransistors.

6.1 CuSCN:$PC_{70}BM$ Thin Film Transistors

Thin-film transistors were fabricated with a CuSCN:$PC_{70}BM$ active layer in the top-gate bottom contact device configuration shown in Figure 6.1. The channel length and channel width of fabricated devices were 30μm and 1000μm, respectively. In a similar manner to the way in which CuSCN NWs were grown in solar cells, in order to grow CuSCN-NWs in the conducting channel of the TFT, CuSCN is first deposited on the glass substrate over the source-drain electrodes, to act as a seed layer for the NWs. Subsequently a CuSCN:$PC_{70}BM$ mixed solution was deposited on the CuSCN layer to induce the growth of CuSCN NWs in a PCBM matrix, as shown in Figure 6.1b. Pristine CuSCN devices (Figure 6.1a) and CuSCN/$PC_{70}BM$ (Figure 6.1c) planar device were also fabricated as control devices, with all three devices fabricated using the same device configuration to enable comparisons of their performance.

Figures 6.1d-f show the transfer characteristics of the three devices. Starting with figure 6.1d, which shows the transfer characteristics of the pristine CuSCN device, this device clearly exhibits p-type conduction with a low turn-on voltage

(~10V). The extracted mobilities from the device in linear and saturation regimes are $1\times10^{-4}cm^2/Vs$, and $3\times10^{-4}cm^2/Vs$ respectively. These values are lower compared to reported values (~0.01 cm^2/Vs) because CYTOP was used as the gate dielectric layer in our experiment, rather than a more optimized dielectric.[1] In addition, it shows that with this configuration, only p-type conduction can be observed, probably because gold is used as the electrode with a work function of -5.4eV, which is too deep for electron transport.

Next, in the planar CuSCN/$PC_{70}BM$ device (Figure 6.1f), no field-effect current can be measured. We believe that such behavior occurs because charges are induced at the interface between CYTOP and pristine $PC_{70}BM$ layer. Hole carriers cannot be transported within this conducting channel because distance from the top CYTOP/$PC_{70}BM$ interface, to CuSCN/$PC_{70}BM$ interface and eventually transport to the gold electrode is too large (~150nm), as shown in Figure 6.2a. On the other hand, electrons cannot be transported to the gold electrode through compact CuSCN layer because CuSCN is an electron blocking layer, blocking the injection of electrons from the electrodes into PCBM, and due to the high work function of gold which makes electron injection into the CuSCN difficult in the first place (Figure 6.2b).

Finally, in mixed CuSCN:$PC_{70}BM$ device (Figure 6.1e), we could observe hole transport in the device, with the measured mobility for linear and saturation regimes both calculated as $1\times10^{-2}cm^2/Vs$, meaning it has improved by 100 times compared to pristine CuSCN layer. The gate-induced holes at the CYTOP/$PC_{70}BM$ interface can now be collected by the gold electrode because of the presence of CuSCN-NWs, which enable efficient transport of holes through the PCBM matrix, and since the CuSCN NWs extend through almost all of the PCBM matrix, induced

holes at the PCBM/CYTOP interface have only a short path to reach CuSCN-NW as shown in Figure 6.2c. The turn-on voltage has increased to 60V, meaning that an extra driving force is required to drive holes from $PC_{70}BM$ to CuSCN. Gate induced electrons can still not be measured because electrons are required to transport from CYTOP/CuSCN:$PC_{70}BM$ interface and overcome the energetic barrier of high conduction band CuSCN. It is also worth noting that the transfer characteristics display an s-shape, which could imply that the conducting channel is perturbed by the CuSCN NW nanostructure, causing a barrier for the charge carrier to transport through the CuSCN/$PC_{70}BM$ interface.

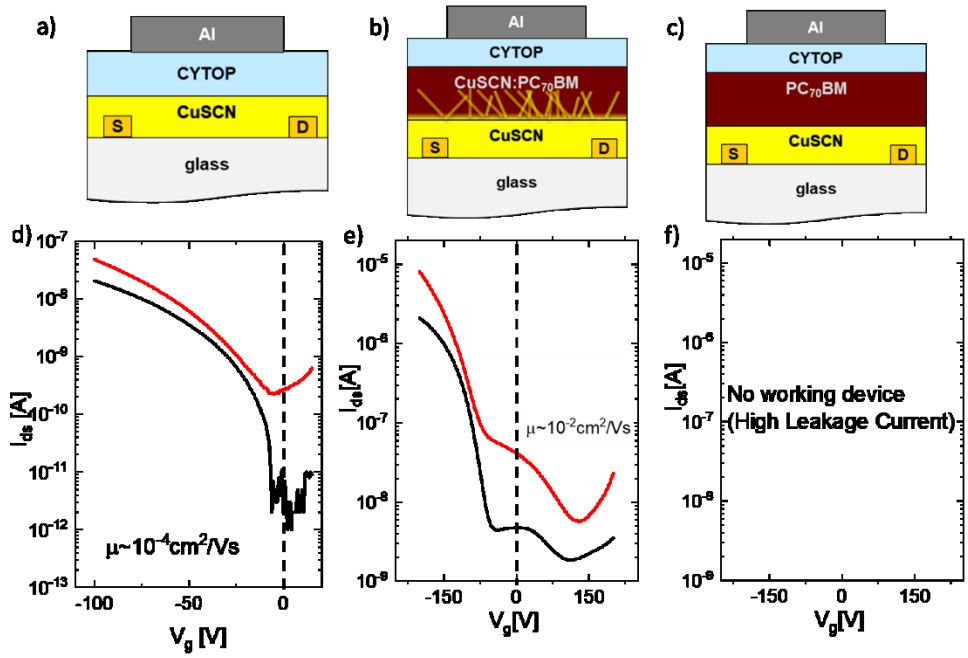

Figure 6.1 Transistor device structure for the electrical measurement of a) CuSCN b) CuSCN:$PC_{70}BM$, c) CuSCN/$PC_{70}BM$ planar devices. Transfer characteristics of d) Pristine CuSCN, e) CuSCN:$PC_{70}BM$, and f) CuSCN/$PC_{70}BM$ planar device. For the planar CuSCN/$PC_{70}BM$ device, no working devices were successfully made as the leakage current dominated in the device. The dotted line is at 0V to indicate hole (negative gate voltage) and electron (positive gate voltage) currents.

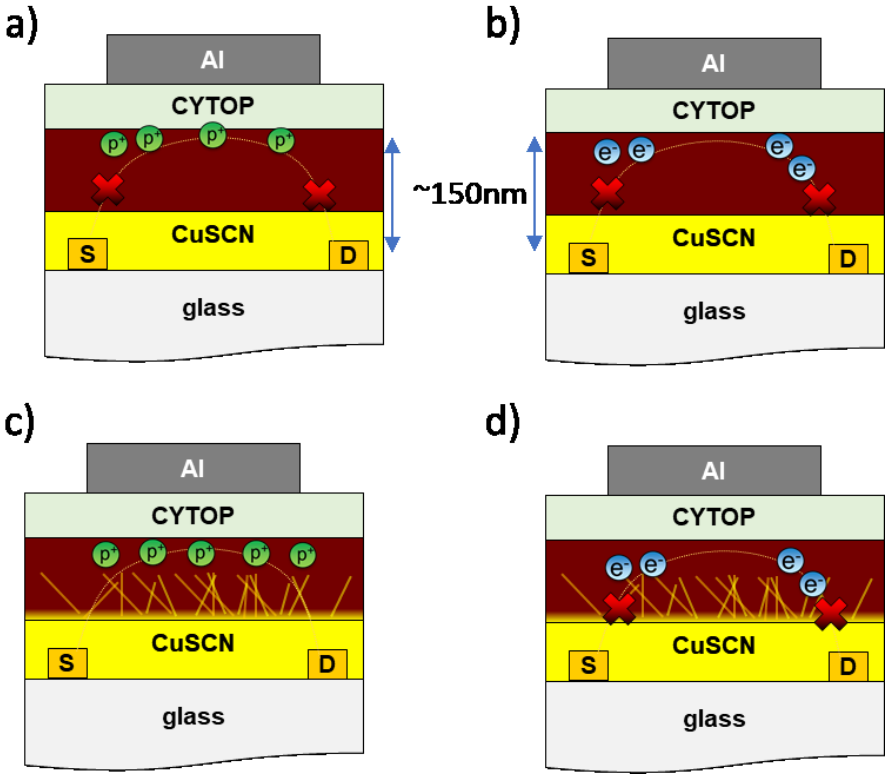

Figure 6.2 Illustrative diagram of charge transport scenario inside CuSCN based transistors. a) Holes transport in the planar CuSCN/$PC_{70}BM$ planar device is not effective because of the long transport direction from the top of CYTOP to the electrode. b) Electron transport in CuSCN/$PC_{70}BM$ is not successful because of the shallow conduction band of CuSCN and due to the long transport distance for electrons. c) Hole transport in the CuSCN:$PC_{70}BM$ device is efficient. It is because gate induced holes can be collected to the CuSCN-NWs as they are close to each other. The measured mobility is 100 times higher than the pristine CuSCN layer. d) Electron transport in the CuSCN:$PC_{70}BM$ device is inefficient as the CuSCN-NWs cannot be used to collect electrons.

Although through this measurement we have demonstrated an improvement in the hole transport in CuSCN:$PC_{70}BM$ device compared to CuSCN and PCBM-only devices, the CuSCN:PCBM layer should display also a high electron mobility in order to explain the efficient photovoltaic performance using this layer. This was not measured, possibly due to the deep work function of gold (-5.2eV) and shallow

conduction band minimum of CuSCN (-5.4eV) which makes electron injection from the electrodes to CuSCN difficult. To improve this, we therefore fabricated the device with stacked aluminium and gold electrodes, since the work function of aluminium is -4.2eV, which is more closely aligned to the CB of CuSCN. In this configuration (Figure 6.3), aluminium is first deposited on the glass substrate before gold because aluminium has better adhesion to glass than gold.

Additionally, we also fabricated another set of devices where the source/drain electrodes were deposited on top of CuSCN to see whether the electron transport is limited by the thick CuSCN compact layer (Figure 6.3b and Figure 6.3c). Another CuSCN/PCBM bilayer reference device was also fabricated using the latter electrode configuration. Figure 6.3 shows the transfer characteristics of these transistors, with the extracted parameters is summarized in Table 6.1. When Al/Au electrodes are deposited on top of glass, we could measure a clear ambipolar transport characteristics in mixed CuSCN:$PC_{70}BM$ device (Figure 6.3d). The extracted mobility values for holes and electrons in the saturation regime are found the be $6\times10^{-3}cm^2/Vs$ and $2\times10^{-3}cm^2/Vs$, respectively. The hole mobility has improved from $1\times10^{-4}cm^2/Vs$ to $2\times10^{-3}cm^2/Vs$ compared to CuSCN-only devices (Figure 6.1d), but it is still difficult to conclude that the improvement is solely originated from improved charge transport through the CuSCN-NWs. This is because $PC_{70}BM$, CuSCN, and CuSCN-NWs layers all show decent hole-transporting properties, and the measured hole mobility in this device is a net mobility combining the mobilities of all of the above layers. Nevertheless, this balanced mobility confirms that both carriers can be transported effectively in our photovoltaic device.

Additionally, in the saturation regime (V_{ds}=200V), we could measure clear

ambipolar transport characteristics, which is displayed through the evident V-shape curve. The threshold voltage obtained under this regime for electrons and holes carriers are 3V and -126V, respectively. That means under strong electric field between the source and drain electrodes carriers, especially electrons, can be transported through the conduction band barrier of CuSCN to the electrodes. However, in the linear regime (V_{ds}=60V), the threshold voltage for electron transport increases significantly from 3V to 154V, which suggests that electrons are either trapped or blocked by CuSCN from reaching aluminium electrodes and can only overcome this barrier when the gate voltage is more than 154V.

Next, for the device where aluminium and gold electrodes were deposited on top of CuSCN (Figure 6.2b) so that electrons are not required to transport through CuSCN to reach the source/drain electrodes, we observed further improved electron transport in this device, which confirms that electrons transport more effectively in this device structure. The measured electron mobility is found to be 2×10^{-2}cm^2/Vs, which is slightly higher compared to the device structure in Figure 6.3a. We could also observe hole current from such device. Unfortunately, the threshold voltage of the hole current is near -175V, which is near to the measurement limit of the source meter. As a result, reliable hole mobility cannot be measured in such a device. Lastly, in the same device configuration without the CuSCN-NW but only the bilayer, only electron current can be measured. The carrier mobility is found to be 8×10^{-2} cm^2/Vs, which is nearly 100 times higher compared to the device structure in Figure 6.3a. As a result, we could confirm that the electron current is limited by the compact CuSCN layer.

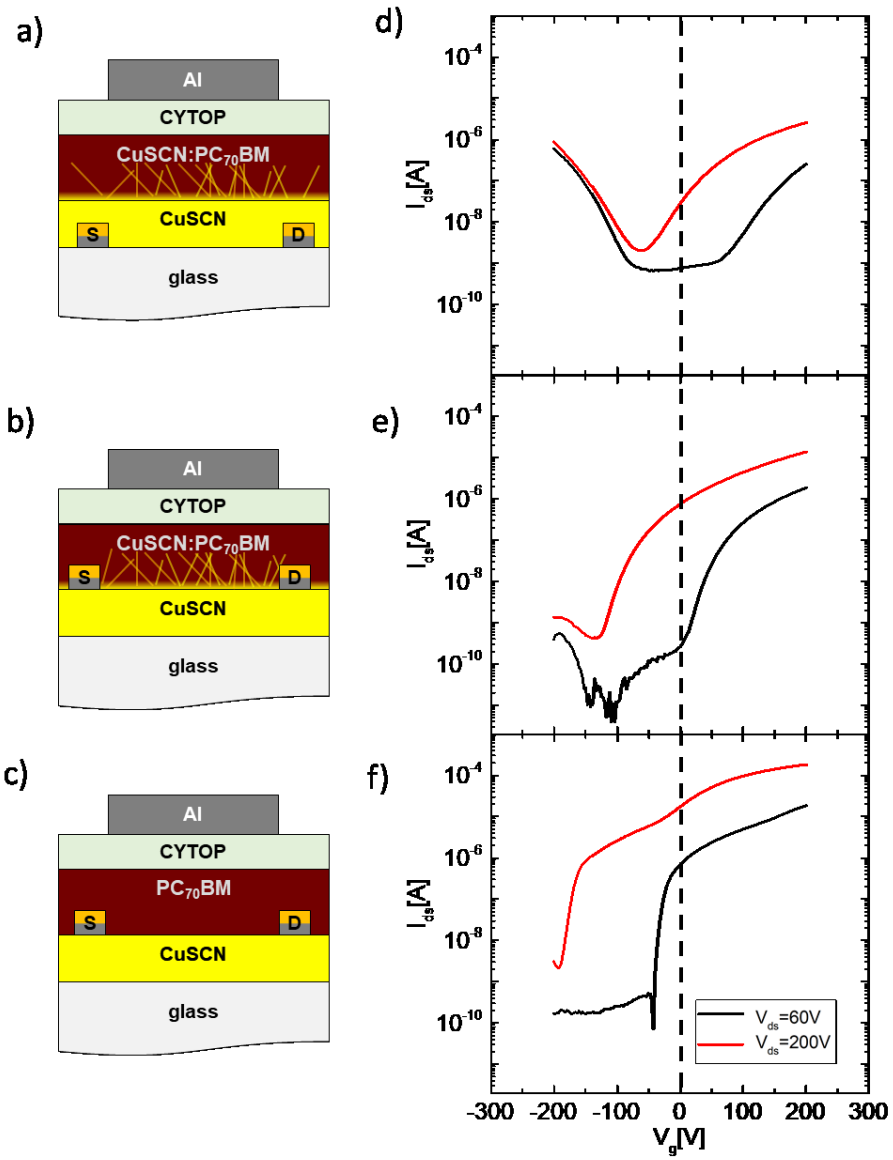

Figure 6.3 Device structure and the corresponding transfer characteristics of CuSCN:$PC_{70}BM$ device using Al/Au as the source/drain electrodes. a) CuSCN-NWs are deposited on CuSCN compact layer. b) Al/Au electrodes are deposited on the compact CuSCN layer. c) Pristine $PC_{70}BM$ and Al/Au are deposited on the compact CuSCN layer. d) Transfer characteristics of the mixed CuSCN:$PC_{70}BM$ device with electrodes inside CuSCN layer. e) Transfer characteristics of the mixed CuSCN:$PC_{70}BM$ device with electrodes on top of CuSCN layer. f) Transfer characteristics of the planar CuSCN/$PC_{70}BM$ device with electrodes on top of CuSCN layer. The dotted line shows V_g=0V, indicating no charges are induced from the gate electrode.

	Carrier	μ_{linear} [cm^2/Vs]	μ_{sat} [cm^2/Vs]	V_t (lin) [V]	V_t (sat) [V]	On Off Ratio
Pristine CuSCN						
Mixed layer	n	$2x10^{-3}$	$2x10^{-3}$	154	3	~1000
Mixed layer (S/D electrode on CuSCN)	n	$2x10^{-2}$	$1x10^{-2}$	122	-10	~10000
Bilayer (S/D electrode on CuSCN)	n	$6x10^{-2}$	$8x10^{-2}$	106	-104	~100000

Table 6.1 Summarizing table of carrier mobility, threshold voltage (V_t) and on-off ratio of CuSCN:$PC_{70}BM$ based transistors.

6.2 CuSCN:$PC_{70}BM$ Phototransistor

Having established that CuSCN:PCBM nanowire layers can be effectively used to fabricate ambipolar transistors, I proceeded to attempt to combine this with the charge photo-generating properties demonstrated by this layer in a previous chapter, to fabricate phototransistors. Photodetectors have a wide range of applications, such as in biomedical imaging, video imaging, security, and in military use.[2–6] In this section, I therefore present the results obtained when fabricating phototransistors using CuSCN:$PC_{70}BM$.

Figure 6.4 shows the light emission spectra of the three LEDs used to characterize the properties of these transistor, and the absorption spectrum of CuSCN:$PC_{70}BM$ photoactive layer, and the absorption spectra of CUSCN and CuSCN/PCBM bilayers for comparison. I then fabricated phototransistor devices using CuSCN:$PC_{70}BM$ as the photoactive layer, using the same TFT device structure as in the previous section (Figure 6.1b). Only gold was used as the source/drain

electrode. The device is then illuminated from the three different LEDs with different wavelengths from the glass side (Figure6.5). It is expected that excitons can be excited at CuSCN:$PC_{70}BM$ interfaces, which is in the CuSCN-NW rich region. In such a situation, the distance between free carrier to the source/drain electrode is greatly reduced to help the collection of both holes and electrons as shown in Figure 6.5.

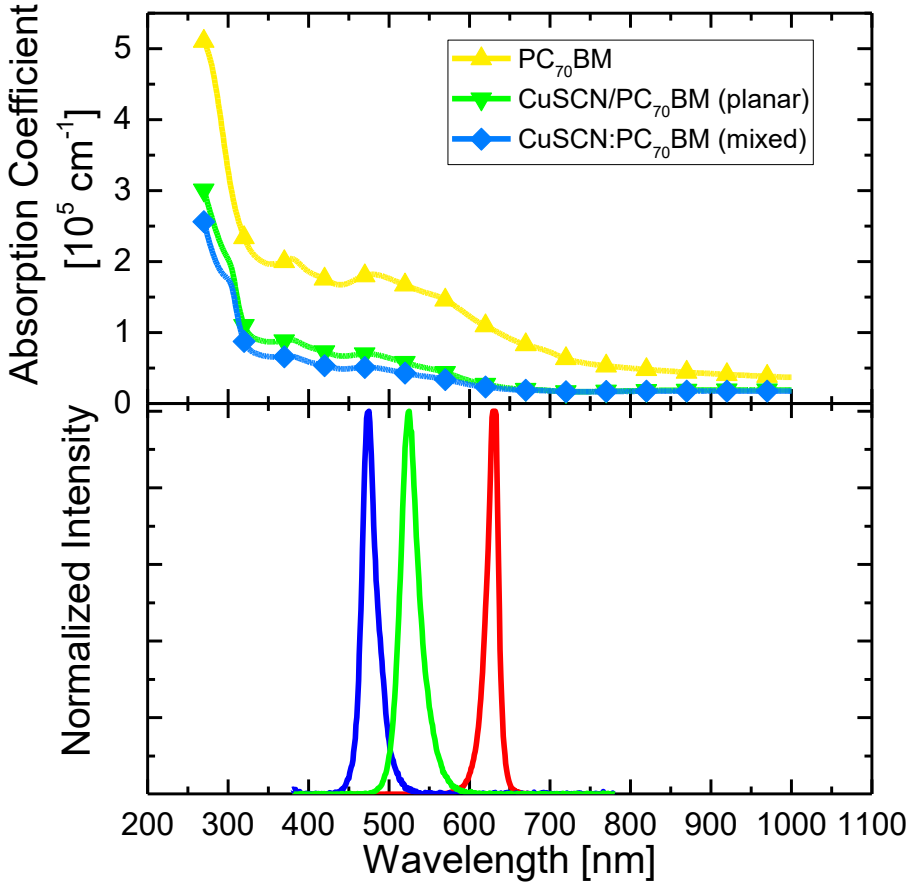

Figure 6.4 Absorption coefficient of $PC_{70}BM$, CuSCN/$PC_{70}BM$, and CuSCN:$PC_{70}BM$ film (top panel). Electroluminescence of different LEDs we used in our analysis (bottom panel).

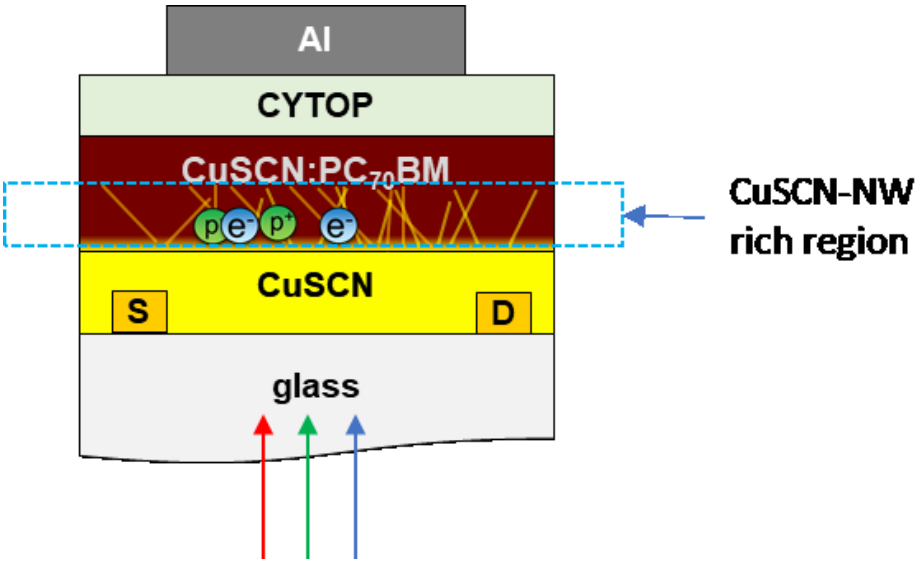

Figure 6.5 Device structure of CuSCN:$PC_{70}BM$ phototransistor. The free carriers are photoexcited to form at the bottom layer of CuSCN:$PC_{70}BM$ so that carriers can be extracted to the S/D electrode for a shorter distance.

Figure 6.6 shows the transfer characteristics of the CuSCN:$PC_{70}BM$ phototransistor illuminated with the three different LEDs. The carrier transport mechanism of the device under different conditions is illustrated in Figure 6.7. We consider first the situation when there is no applied gate voltage (V_g=0V) in the device, which means that there is no induced carrier by CYTOP at the CYTOP/CuSCN:$PC_{70}BM$ interface. When no light is illuminated, the source/drain current is measured to be 4.5nA. With the illumination of red, green, and blue light at a power density of 300mW/cm^2, the current sees an insignificant increase to 6.6nA, 7.5nA, and 9.9nA, respectively, which indicates that the induced carriers cannot be mobilized. This is because most of the photoinduced carriers are energetically trapped (Figure 6.7a and Figure 6.7b). If the gate voltage is then positively biased, which means electrons will be induced at the CYTOP/CuSCN:$PC_{70}BM$ interface, the dark current is measured to be 3nA at V_g=+200V. This suggests that even at high V_g the induced electrons at the CYTOP/CuSCN:$PC_{70}BM$ interface cannot be mobilized,

because the distance for an electron to transport to the electrodes is too long (~150nm) (Figure 6.7c). On the other hand, since the photoinduced carriers are formed at the bottom of CuSCN:$PC_{70}BM$ layer, which is closer to the conducting channel, under light illumination the measured currents are 640nA, 470nA, and 480nA for red, green and blue light, respectively, at an illumination of 300mW/cm^2.the measured current is increased by 150-200times (Figure 6.7d). When the gate voltage is negatively biased, holes can be induced at the CYTOP/CuSCN:$PC_{70}BM$ interface. However, with or without light illumination, the measured hole current has no significant increase. Dark and light currents are 200nA and 230nA respectively. It suggests that photoinduced holes are not mobilized and do not contribute to hole conduction. The reason behind this is still unclear. The photoexcited charges may be recombined due to high hole concentrations, or the density of hole traps at the bottom of CuSCN:$PC_{70}BM$ layer is exceptionally high, such that most photoexcited holes are trapped before they can be mobilized. Finally, there is a void region where the device could not be turned on. The width of such a region is denoted by ΔV_{void}, we believe that such a void region depends on the trap densities of the device. When there is no illumination, the device cannot be turned on in at any negative gate voltage. Under illumination, electron current starts to increase at V_g=+15V, suggesting that trap states are filled at such voltage, photoinduced current can now be mobilized to contribute to I_{ds}.

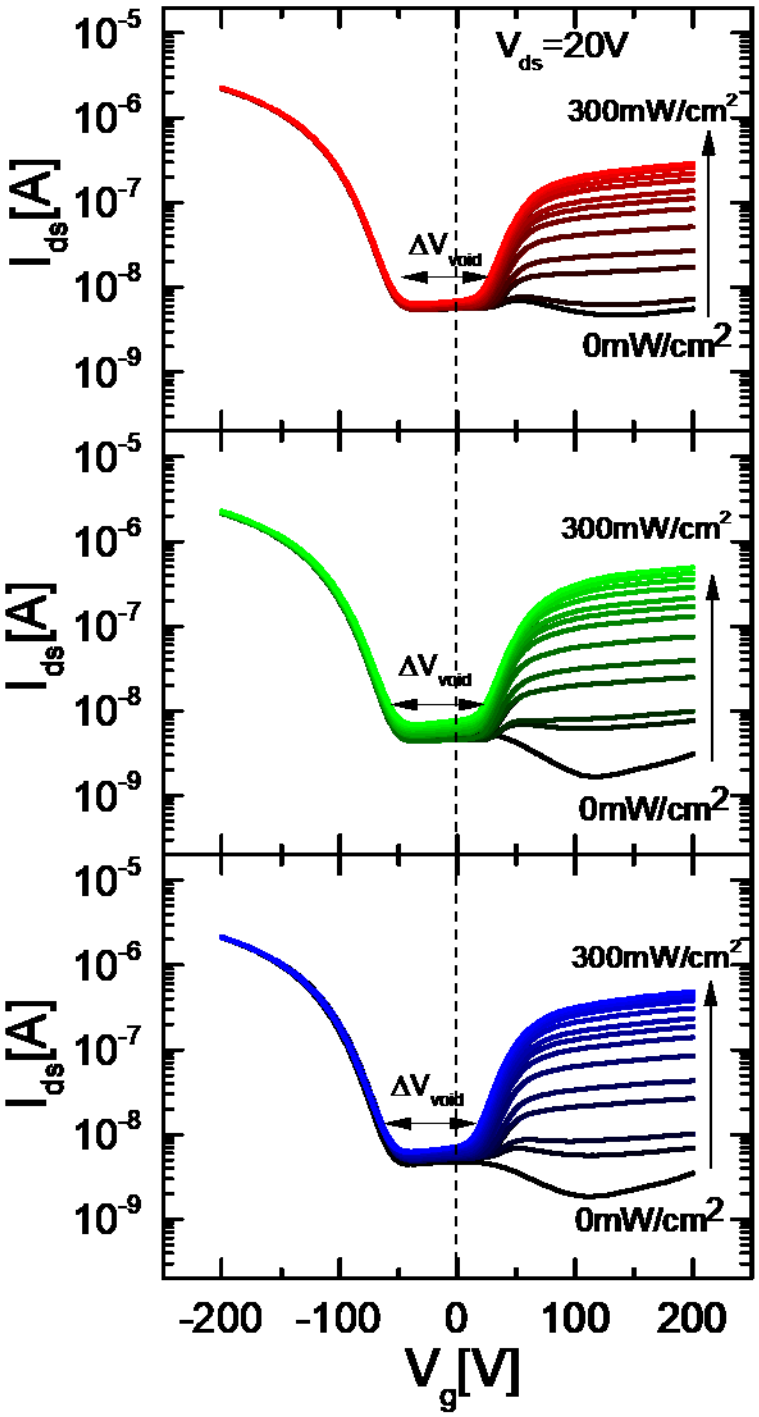

Figure 6.6 Transfer characteristics of CuSCN:$PC_{70}BM$ device when it is illuminated by red (630nm), green (530nm), and blue (480nm) light. The power density was increased from 0 to 300mW/cm^2. ΔV_{void} represents the difference of turn on voltage of holes and electrons. The dotted line shows V_g=0V, indicating no charges are induced from the gate electrode.

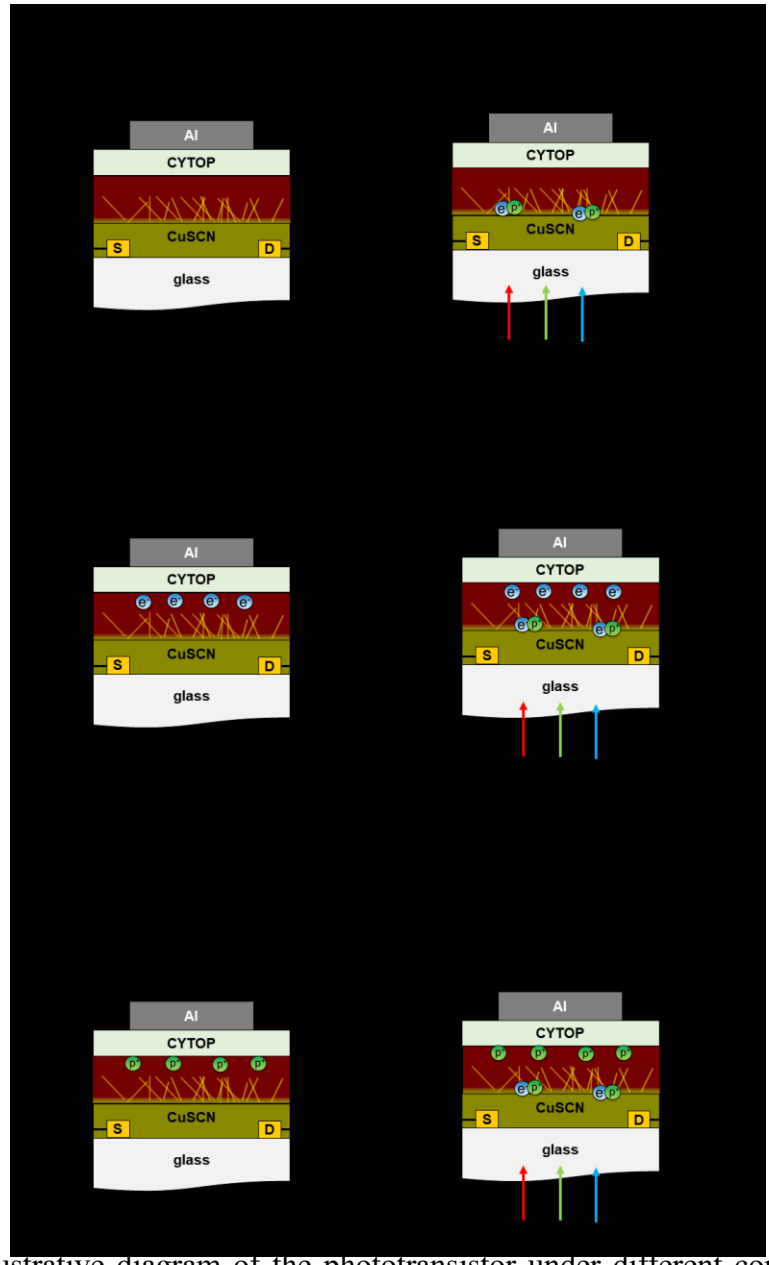

Figure 6.7 Illustrative diagram of the phototransistor under different conditions. a) No charge is induced when no gate voltage is applied, and light illuminated on the device. b) When light is illuminated on the device, free carriers are induced at to bottom of the CuSCN:$PC_{70}BM$ NW layer. These carriers are not mobilized due to trap states. c) When V_g=+200V is applied, electrons are induced at the top of the device. However, due to the long distance is required to travel from top of the CuSCN:$PC_{70}BM$ device to the electrode, no electron current is measured. d) When V_g=+200V is applied with light illuminated on the device, free carriers are excited at the bottom of the CuSCN:$PC_{70}BM$ device. High electron current is measured because the trap states are filled. e) When V_g=-200V is applied and no light is illuminated, holes are induced at the top of the CuSCN:$PC_{70}BM$ layer. Holes can be measured as CuSCN and $PC_{70}BM$ have good hole-transport property. f) When V_g=-200V is applied and light is illuminated on the device, free carriers are excited at the bottom of CuSCN:$PC_{70}BM$ layer, the measured hole current has no significant increment.

6.3 CuSCN:$PC_{70}BM$ phototransistor characterisation

As discussed from the previous section, a photo-response is observed in CuSCN:$PC_{70}BM$ device when the device is positively biased at the gate voltage. To demonstrate the potential of CuSCN:$PC_{70}BM$ layer in the application of phototransistors, photosensitivity (P), responsivity (R), and detectivity (D^*) are extracted using the transport characteristics of the CuSCN:$PC_{70}BM$ device as shown in Figure 6.8.

Photosensitivity measures the ratio between the photocurrent (I_{ph})and the dark current

$$P = \frac{I_{ph}}{I_{dark}} = \frac{I_{illum} - I_{dark}}{I_{dark}} \tag{6.1}$$

where I_{illum} is the measured drain current under illumination. The maximum photosensitivity for our phototransistors is at 128V with a value of 190. Responsivity measures the amount of photocurrent per unit power, which is given by

$$R = \frac{I_{ph}}{P_{opt}} = \frac{I_{illum} - I_{dark}}{P_{opt}} \tag{6.2}$$

where P_{opt} is the incident optical power on the device. Figure 6.8 shows the responsivity of the CuSCN:$PC_{70}BM$ device at different gate voltage for illumination at 630nm. We have also illuminated the device at different wavelength and found there is no significant difference. The maximum of responsivity is 19.1 when the gate voltage is +104V. Finally, the specific detectivity is given by

$$D^* = \frac{\sqrt{a\Delta f}}{NEP} = \frac{\sqrt{a}R}{S_{noise}} \tag{6.3}$$

where a is the device area, Δf is the bandwidth, NEP is the noise-equivalent power, S_n is the noise spectral density. Specific detectivity measures the sensitivity of the phototransistors or photodetectors. The larger the specific detectivity, the more it is suitable to detect a weak signal as there could be thermal noise in dark current, I_{dark}. Table 6.2 shows the summarizing table of the device. Comparing the result from Huang et. al. (Table 6.2), who used pristine $PC_{60}BM$ as the photoactive layer. It shows that CuSCN:$PC_{70}BM$ does not have superb performance as a phototransistor.

	P	R [A/W]	Dx10^{10} [Jones]
30V	**4**	**5.6**	**2.9**
$PC_{60}BM$ [9]	~10000	~1000	~1000

Table 6.2 Summarising table of photosensitivity, responsivity and detectivity of CuSCN:$PC_{70}BM$ phototransistor.

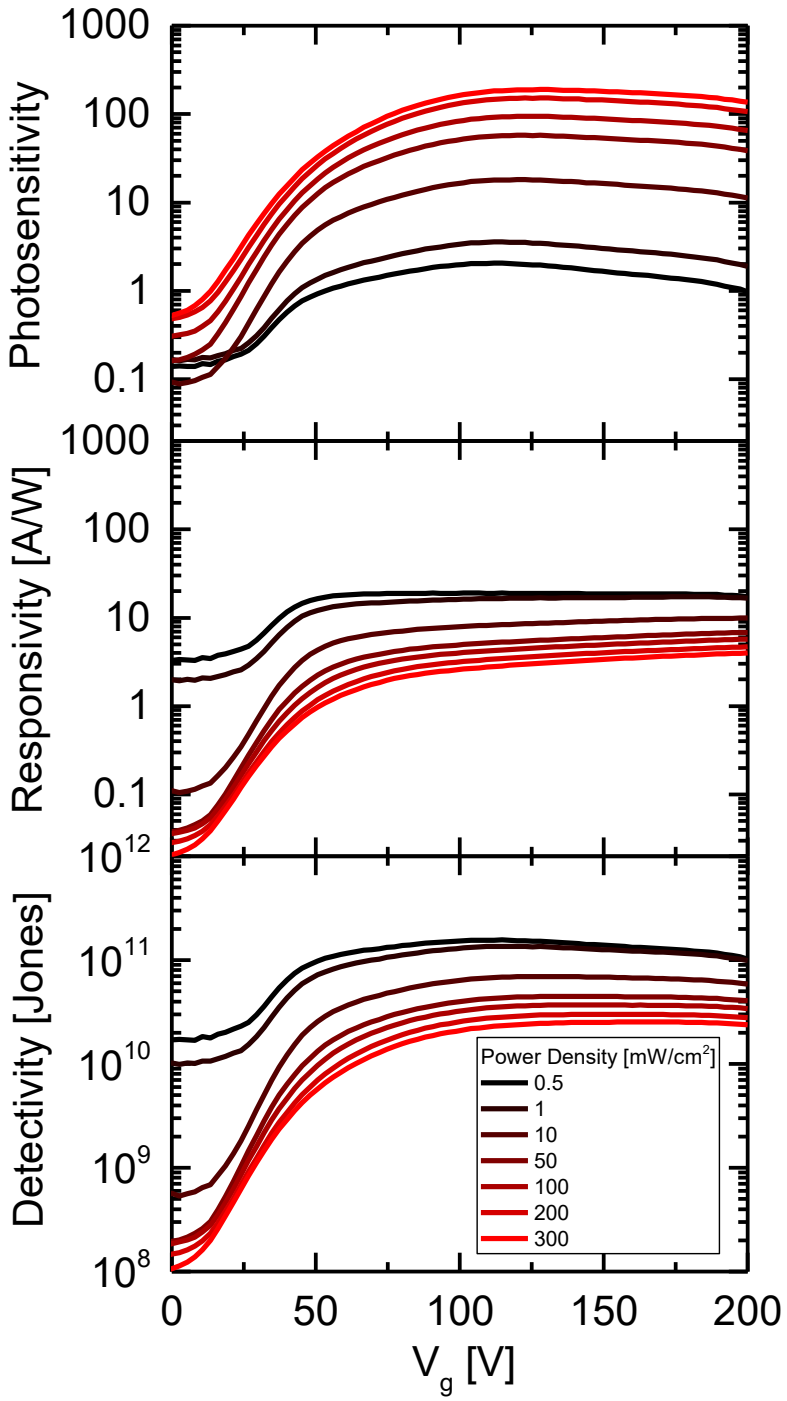

Figure 6.8 Photosensitivity, responsivity, and detectivity of CuSCN:PC70BM device at different V_g (Illuminated at 650nm wavelength)

6.4 Dynamic measurements of CuSCN:$PC_{70}BM$ phototransistor

We have also investigated the dynamic response of CuSCN:$PC_{70}BM$ phototransistor by measuring the switching behavior. The experimental setup is shown in Figure 6.9. The LED is connected to a signal generator which generates square waves pulses at different frequencies. The power from the LED (650nm) is 300mW/cm^2. The alternating on/off LED causes periodic photoinduced charge generation. The constant I_{ds} from the phototransistor is then connected to a current amplifier. The rise time and fall time of the device are measured in both V_g=+140V (electron current) and V_g=-140V (hole current). The rise time, t_R is defined as the time taken for the current to rise from 10% to 90% of the maximum current. The fall time, t_F is defined as the time taken for the current to fall from 90% to 10% of the maximum current.

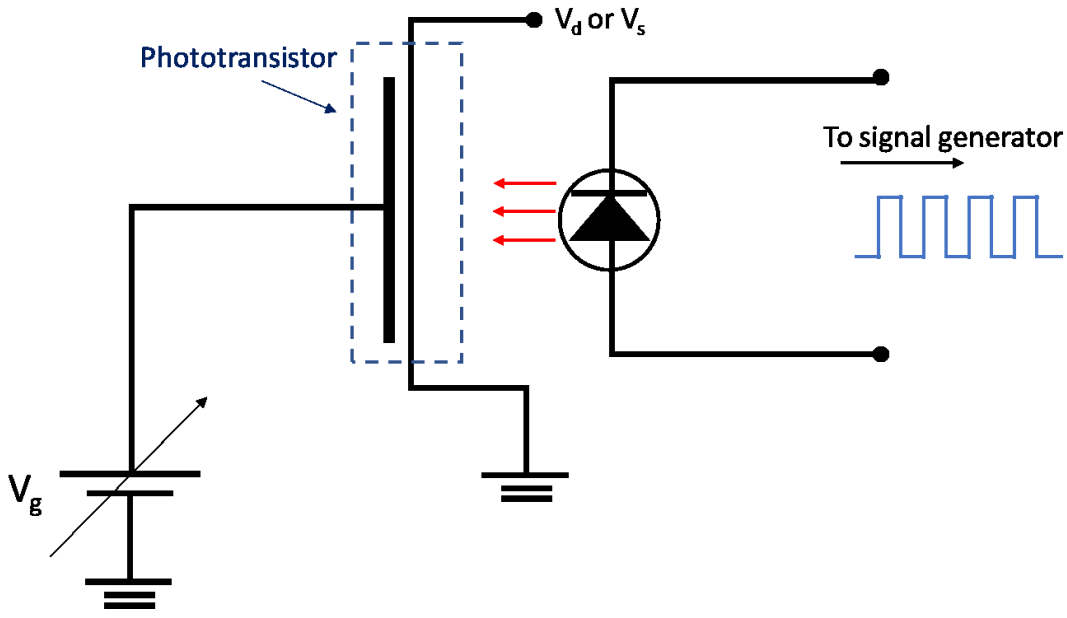

Figure 6.9 Experimental setup of dynamic measurements of CuSCN:$PC_{70}BM$ device.

Figure 6.10 shows the dynamic measurement of CuSCN:$PC_{70}BM$ when V_g positively biased (+140V, electron current). In such a configuration, we measured the rise time and fall time. The bottom panel of Figure 6.10 shows signal of one single pulse of such a device. The rise time and fall time are 3ms and 38ms, respectively. On the other hand, when V_g is negatively biased (-140V), the response from the device and the signal from a single pulse are shown in Figure 6.11. As discussed before, the hole current does not have a significant increase. A current amplifier was used in order to obtain a stable signal and to reduce the signal to noise ratio. The rise time and the fall time are 12.4ms and 2.8ms, respectively. We have also fabricated the phototransistor device using pristine $PC_{70}BM$ device for the dynamic measurements (without CuSCN-NWs) as a reference. Figure 6.12 shows such measurements when V_g=+140V (electron) and V_g=-140V (hole). The rise time and fall time are summarized in Table 6.3. It shows that with CuSCN-NWs inside the photoactive layer, the rise time and fall time are both improved. However, compared to inorganic phototransistors, or recent work on organic phototransistors, the rise time and fall time of are usually less than 1ms, which means that CuSCN:$PC_{70}BM$ device have long response time.[7–9] The device may be limited by the CuSCN film which covers the compact CuSCN layer, which causes a longer pathway for the carriers to be collected at the electrode.

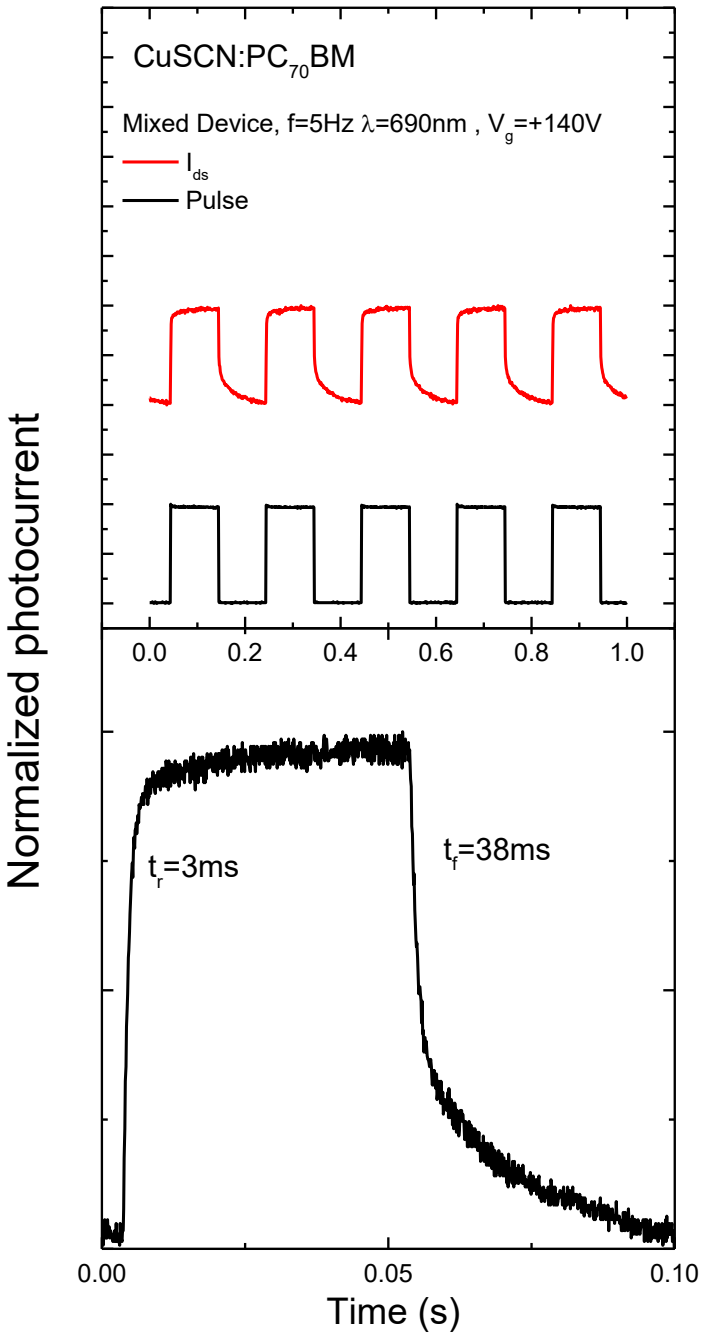

Figure 6.10 Dynamic measurements of CuSCN:$PC_{70}BM$ device when V_g=140V and V_{ds}=+140V. Electron current is measured in such a configuration. The bottom panel shows a single pulse. Rise time and fall time were then measured from this plot

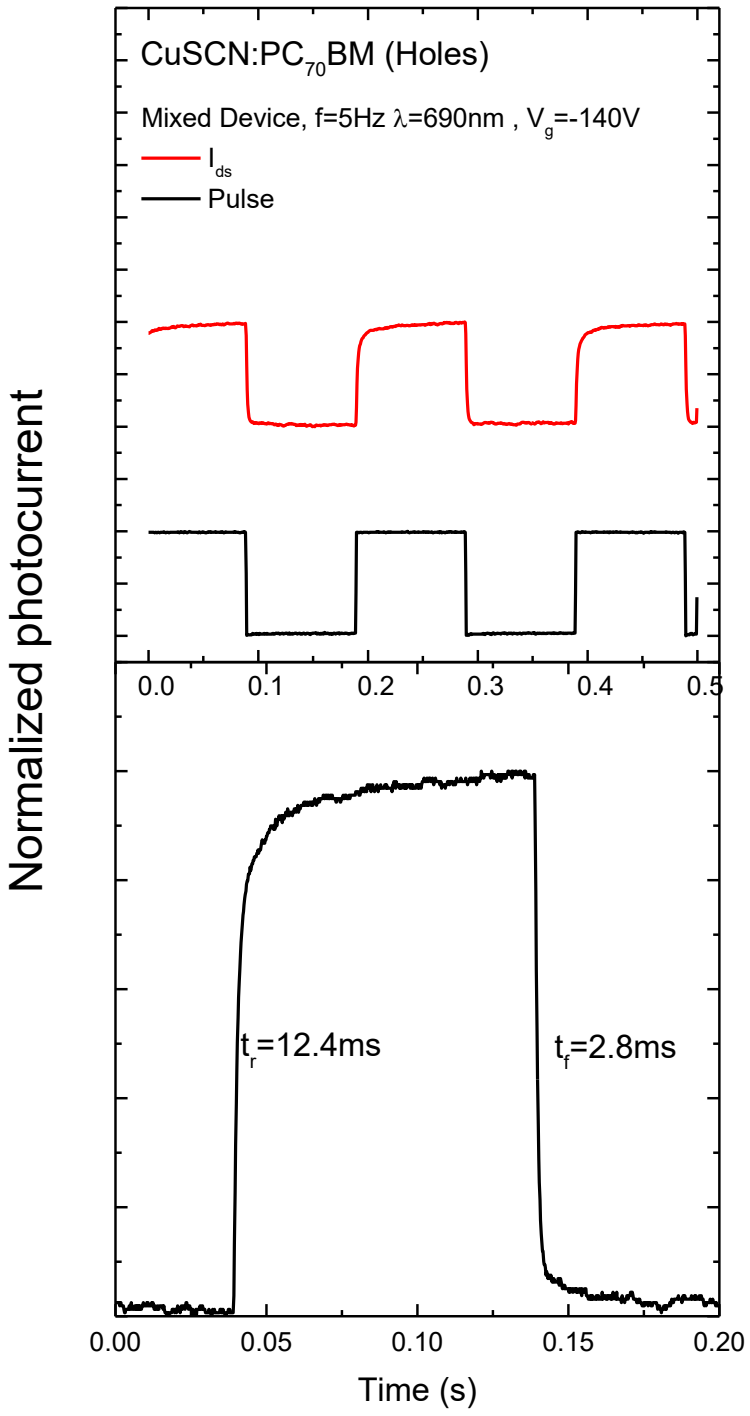

Figure 6.11 Dynamic measurements of CuSCN:$PC_{70}BM$ device when V_g=-140V and V_{ds}=-140V. Hole current is measured in such configuration. The bottom panel shows a single pulse. Rise time and fall time were then measured from this plot

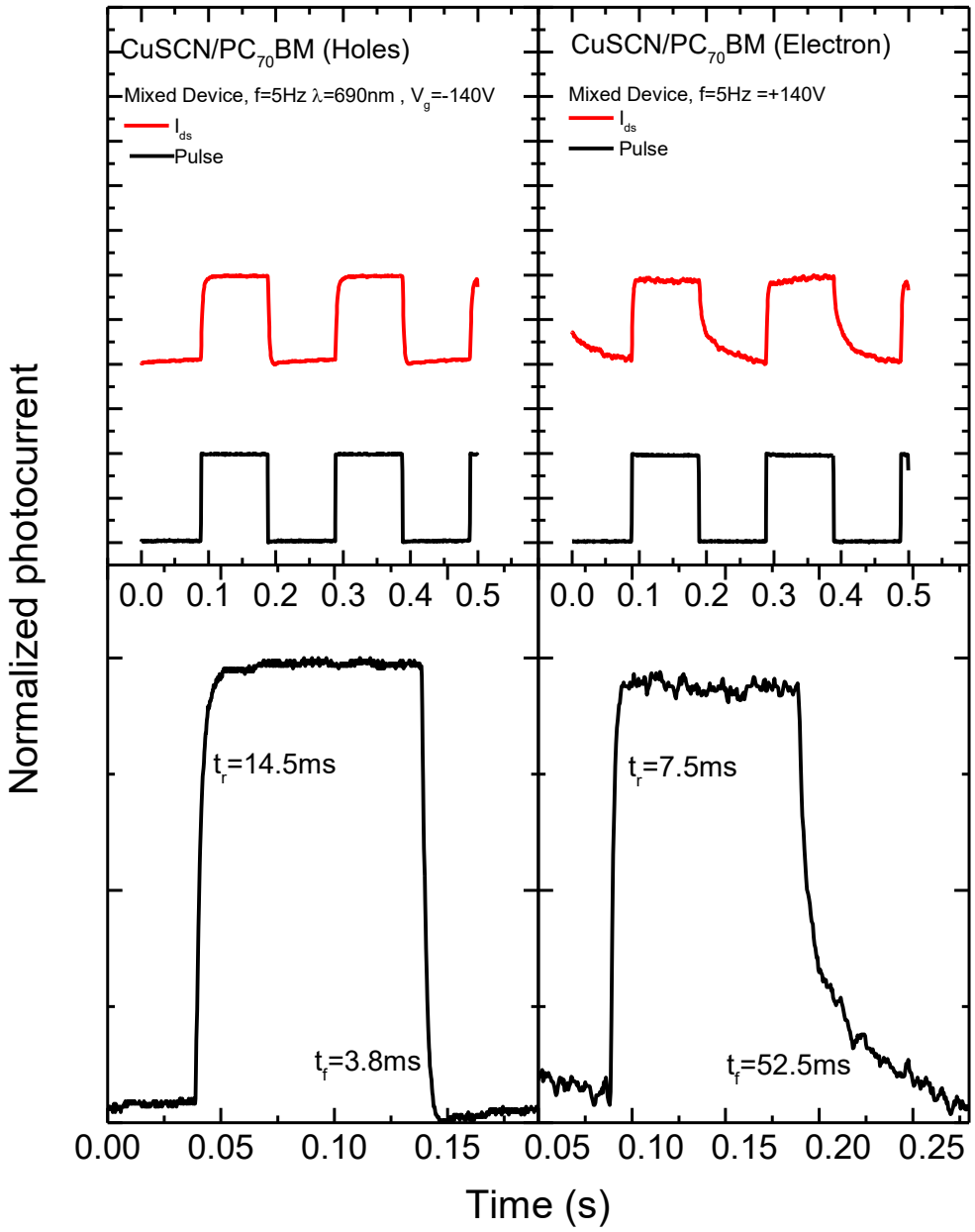

Figure 6.12 Dynamic measurements of CuSCN/PC_{70}BM planar device. Gate voltage for holes and electron current are -140V and 140V respectively. The top panel shows the normalized photocurrent and the pulse signal from the LED. The bottom panel shows a single pulse. Rise time and fall time were then measured from these plots.

		t_r [ms]	t_f [ms]
Hole			
	Bi-layer	14.5	3.8
Electron			
	Bi-layer	7.5	52.5

Table 6.3 Summarizing table of rise time and fall time of CuSCN:$PC_{70}BM$ phototransistors.

6.5 Conclusion

We have successfully measured the carrier mobility values of holes and electrons in the CuSCN:$PC_{70}BM$ NW layers. The mobility values for holes and electrons are $6\times10^{-3}cm^2/Vs$ and $2\times10^{-3}cm^2/Vs$, respectively. It is worth noting that the transport direction in the transistor is horizontal to the device, which is different from photovoltaic devices. As the alignment of CuSCN-NWs is relatively vertical to the substrates, the actual mobility values in PV devices could possibly be higher. Also, we have utilized $PC_{70}BM$:CuSCN as the photoactive layer to fabricate a phototransistor. The result shows that the hole photocurrent is negligible. Nevertheless, the electron photocurrent is increased by more than 150 times, showing that CuSCN:$PC_{70}BM$ layer may possible to be applied in real-life applications. Dynamic measurement of CuSCN:$PC_{70}BM$ layer is then conducted, the result, unfortunately, shows that the rise time and fall time is not as fast as current devices under research, which suggested that further optimization of the device is required. For instance, reducing the film thickness of CuSCN compact layer may reduce the transport path and improve the rise time and fall time for carriers.

Reference

[1] P.Pattanasattayavong, N.Yaacobi-Gross, K.Zhao, G. O. N.Ndjawa, J.Li, F.Yan, B. C.O'Regan, A.Amassian, T. D.Anthopoulos, *Adv. Mater.* **2013**, *25*, 1504.

[2] M.Razeghi, A.Rogalski, *J. Appl. Phys.* **1996**, *79*, 7433.

[3] Z.Qi, J.Cao, H.Li, L.Ding, J.Wang, *Adv. Funct. Mater.* **2015**, *25*, 3138.

[4] E.Monroy, F.Omnès, F.Calle, *Semicond. Sci. Technol.* **2003**, *18*, 1242

[5] N.Li, Z.Lan, L.Cai, F.Zhu, *J. Mater. Chem. C* **2019**, *7*, 3711.

[6] H.Han, S.Nam, J.Seo, C.Lee, H.Kim, D. D. C.Bradley, C. S.Ha, Y.Kim, *Sci. Rep.* **2015**, *5*, 1.

[7] W.Huang, Y. H.Lin, T. D.Anthopoulos, *ACS Appl. Mater. Interfaces* **2018**, *10*, 10202.

[8] V. N.Tran, R.Stuart, H.Bhavsar, *Phototransistor Switching Time Analysis, AN3009, Calif. East. Lab., CA , USA* **2009***, P.1*

[9] J. J.Ho, Y. K.Fang, K. H.Wu, W. T.Hsieh, S. C.Huang, G. S.Chen, M. S.Ju, J. J.Lin, *IEEE Trans. Electron Devices* **1998**, *45*, 2085.

Chapter 7 Conclusion and future work

In this thesis, we have discovered that the methanofullerenes, namely $PC_{60}BM$ and $PC_{70}BM$ have excellent ambipolar transport properties. Both $PC_{60}BM$ and $PC_{70}BM$ have mobility values on the order of 10^{-2} cm^2/Vs for both hole and electrons carriers. Such balanced mobility is ideal in photovoltaic systems. We then also utilize the light absorption property of these methanofullerenes to make planar heterojunction solar cell using $PC_{60}BM$ and $PC_{70}BM$ using CuSCN as the electron blocking and hole transporting layer helps the efficiency to improve to nearly 2% compared to the device using PEDOT:PSS as the hole transporting layer. By mixing dilute CuSCN with the fullerenes to make a blend solution (1:3 CuSCN:$PC_{70}BM$ volume ratio), nanowire mesostructures were formed in the photoactive CuSCN:$PC_{70}BM$ layer. Such mesostructures improved the short circuit current density from $2mA/cm^2$ up to $10mA/cm^2$. This kind of nanowires can only be formed in $PC_{70}BM$ under our investigation. We then investigated the microstructure of the CuSCN:$PC_{70}BM$ device using transmission electron microscopy (TEM). The result shows that the length of the CuSCN nanowires is about 30-100 nm from the compact CuSCN layer. Energy-dispersive X-ray spectroscopy confirms that the nanowires are made of CuSCN. Dr. Yuliar Firdaus, our collaborator in King Abdullah University of Science and Technology (KAUST) concludes that the CuSCN nanowires have improved the device by reducing both geminate and non-geminate recombination, which causes the significant increment of short-circuit current. Another group in KAUST also showed that the hybrid organic/inorganic interface between CuSCN and $PC_{70}BM$ facilitates fast and efficient dissociation of exciton and hole extraction. These results show that the CuSCN nanowires provide a large surface area for the collection of carriers and improved the device efficiency.

We then tried to optimize the device performance by changing the substrate temperature during casting of the precursor of the mixed CuSCN:$PC_{70}BM$ solution. It is found that the optimum temperature for the substrate is at 115ºC. We believe that the temperature helps the growth of the CuSCN nanowires, and increases short-circuit current. Different compositions of CuSCN:$PC_{70}BM$ were also used to optimise the device. It is found that when the volume ratio of CuSCN (25mg/ml) and $PC_{70}BM$ (30mg/ml) is the best when it is 1:3, yielding the best device of 5.89% PCE. However, during the investigation of the system, we found that the reproducibility of this kind of device is poor. The same result of 5.89% could not be reproduced when a different batch of $PC_{70}BM$ was used. We then tried to spin-coat an interlayer between the compact CuSCN layer and the photoactive CuSCN:$PC_{70}BM$ layer in order to increase the density of CuSCN NWs, as it has been proven that these NWs are highly important to improve the efficiency of the system. It was found that if the precursor solution used to cast the interlayer is in the ratio of 9:1 of CuSCN:$PC_{70}BM$ by volume, the device improves again to 5.72%. The improvement is again in the short-circuit current density (from 8.3 mA/cm^2 to 10.4 mA/cm^2) . We then took scanning electron microscope (SEM) and TEM images of the device, and found that defects are observed on the surface of the aluminium electrode. By looking at the cross-sectional TEM images, we found that the defects, which have a shape of craters, originated in the CuSCN:$PC_{70}BM$ photoactive layer. Craters are found inside the layer with the size of 200nm in diameter. We tried to deposit double interlayers (spin-coated twice amount of CuSCN:$PC_{70}BM$ layer in 9:1 volume ratio) and found that the number of craters did not increase significantly, which means that the craters are formed either when the first interlayer is spun or when the 1:3 volume ratio photoactive CuSCN:$PC_{70}BM$ layer is spun. We then further investigated the composition inside the craters and found that the crater

dissolves the compact CuSCN, which may cause leakage current. Also, inside the craters, we found that CuSCN NWs were grown relatively horizontally. In some craters, the density of CuSCN NWs is a lot higher than other regions, meaning that the craters could possibly act as a light-absorbing site to facilitate exciton dissociation and hole extraction.

We have also incorporated silver and aluminium nanoparticles in the CuSCN:$PC_{70}BM$ photoactive layer to improve the light absorption spectrum. We found that only aluminium improves the absorption coefficient of CuSCN:$PC_{70}BM$ device and we have improved the PCE from 4.4% to 5.4% when the precursor solution is doped with 10% of aluminium nanoparticles. In fact, we have combined the results to fabricate a CuSCN:$PC_{70}BM$ device with interlayers and aluminium nanoparticles.

We then used field-effect transistors (FETs) to measure the mobility of CuSCN:$PC_{70}BM$ device. Unfortunately, we could not measure the carrier mobility of CuSCN:$PC_{70}BM$ nanowire by itself, but we successfully evaluated the effect on mobility when CuSCN NWs is present in the CuSCN:$PC_{70}BM$ film. The hole mobility of pristine CuSCN is found to be $1\times10^{-4}cm^2/Vs$, while the CuSCN/$PC_{70}BM$ planar device does not show any hole current. We have successfully measured the ambipolar transport of CuSCN:$PC_{70}BM$ device when Al/Au electrodes are used. The FET mobility values for holes and electrons are $6\times10^{-3}cm^2/Vs$ and $1\times10^{-2}\ cm^2/Vs$, respectively, which are similar to the carrier mobility of polymeric solar cell. However, we believe that the hole mobility of CuSCN NW should be higher than this value as the mobility we measured is a net mobility of compact CuSCN, CuSCN NWs and $PC_{70}BM$. We then illuminate the same transistor to create photoexcited carriers to become a phototransistor. In our study, only photoexcited electron current can be significantly mobilized in the application of phototransistors. The peak photosensitivity, responsivity, and detectivity of

CuSCN:$PC_{70}BM$ phototransistor are found to be 190, 19.1A/W, and 158×10^{10} Jones, respectively. Dynamic measurements were also conducted to measure the rise time and fall time. The rise times for electron current in the CuSCN:$PC_{70}BM$ device were 3 ms and 38 ms, respectively, which are rather low compared to recent work on phototransistors.

In the future, this work should focus on understanding the formation conditions for CuSCN NWs. The biggest challenge we faced was the poor reproducibility of such device because of the quality of $PC_{70}BM$ and the formation condition of CuSCN NWs is highly sensitive. It is important to investigate the reason of such uncertainty before systematic analysis. Also, we could optimise CuSCN NWs by varying the length and density of CuSCN NWs inside $PC_{70}BM$. We believe that substrate temperature, concentration of CuSCN and $PC_{70}BM$, and the ratio between the two materials play a major role to control the formation of CuSCN NWs.

By organic synthesis, we could edit the functional group of $PC_{70}BM$ to investigate how such NWs are formed. We believe that $PC_{70}BM$ provides a special crystal structure that only facilitates the formation of CuSCN NWs, which needs to be confirmed by using X-Ray diffraction (XRD). Such investigation may also help to explain why only CuSCN NWs can be formed when it is mixed with $PC_{70}BM$ but not any other fullerenes derivatives. As the limitation of PV device is the light absorption coefficient of $PC_{70}BM$ is not as good as other light-absorbing acceptor molecules, we should search for other light-absorbing acceptors that could form CuSCN NW structure because the CuSCN NW mesostructured could possibly be a new way to improve charge collection efficiency.

Appendix A: Permission from Third Parties

JOHN WILEY AND SONS LICENSE
TERMS AND CONDITIONS

Nov 08, 2019

This Agreement between Wai Yu Sit ("You") and John Wiley and Sons ("John Wiley and Sons") consists of your license details and the terms and conditions provided by John Wiley and Sons and Copyright Clearance Center.

License Number	4704371468166
License date	Nov 08, 2019
Licensed Content Publisher	John Wiley and Sons
Licensed Content Publication	Solar RRL
Licensed Content Title	Charge Photogeneration and Recombination in Mesostructured CuSCN-Nanowire/PC70BM Solar Cells
Licensed Content Author	Thomas D. Anthopoulos, Frédéric Laquai, Safakath Karuthedath, et al
Licensed Content Date	May 2, 2018
Licensed Content Volume	2
Licensed Content Issue	8
Licensed Content Pages	8
Type of use	Dissertation/Thesis
Requestor type	Author of this Wiley article